2016-07-28

Acoustic Green's Function Extraction in the Ocean

Xiaoqin Zang
University of Miami, xiaoqin.zang@hotmail.com

Recommended Citation

Zang, Xiaoqin, "Acoustic Green's Function Extraction in the Ocean" (2016). *Open Access Dissertations*. 1719.
https://scholarlyrepository.miami.edu/oa_dissertations/1719

UNIVERSITY OF MIAMI

ACOUSTIC GREEN'S FUNCTION EXTRACTION IN THE OCEAN

By

Xiaoqin Zang

A DISSERTATION

Submitted to the Faculty
of the University of Miami
in partial fulfillment of the requirements for
the degree of Doctor of Philosophy

Coral Gables, Florida
August 2016

UNIVERSITY OF MIAMI

A dissertation submitted in partial fulfillment of
the requirements for the degree of
Doctor of Philosophy

ACOUSTIC GREEN'S FUNCTION EXTRACTION IN THE OCEAN

Xiaoqin Zang

Approved:

Michael G. Brown, Ph.D. Professor of Ocean Sciences	Jorge F. Willemsen, Ph.D. Professor of Ocean Sciences
Harry A. DeFerrari, Ph.D. Professor of Ocean Sciences	Guillermo J. Prado, Ph.D. Dean of the Graduate School
Guoqing Lin, Ph.D. Associate Professor of Marine Geosciences	

ZANG, XIAOQIN (Ph.D., Applied Marine Physics)
Acoustic Green's Function Extraction (August 2016)
in the Ocean

Abstract of a dissertation at the University of Miami.

Dissertation supervised by Professor Michael G. Brown.
No. of pages in text. (99)

The acoustic Green's function (GF) is the key to understanding the acoustic properties of ocean environments. With knowledge of the acoustic GF, the physics of sound propagation, such as dispersion, can be analyzed; underwater communication over thousands of miles can be understood; physical properties of the ocean, including ocean temperature, ocean current speed, as well as seafloor bathymetry, can be investigated. Experimental methods of acoustic GF extraction can be categorized as active methods and passive methods. Active methods are based on employment of man-made sound sources. These active methods require less computational complexity and time, but may cause harm to marine mammals. Passive methods cost much less and do not harm marine mammals, but require more theoretical and computational work. Both methods have advantages and disadvantages that should be carefully tailored to fit the need of each specific environment and application. In this dissertation, we study one passive method, the noise interferometry method, and one active method, the inverse filter processing method, to achieve acoustic GF extraction in the ocean.

The passive method of noise interferometry makes use of ambient noise to extract an approximation to the acoustic GF. In an environment with a diffusive distribution of sound sources, sound waves that pass through two hydrophones at two locations carry the information of the acoustic GF between these two locations; by listening

to the long-term ambient noise signals and cross-correlating the noise data recorded at two locations, the acoustic GF emerges from the noise cross-correlation function (NCF); a coherent stack of many realizations of NCFs yields a good approximation to the acoustic GF between these two locations, with all the deterministic structures clearly exhibited in the waveform. To test the performance of noise interferometry in different types of ocean environments, two field experiments were performed and ambient noise data were collected in a 100-meter deep coastal ocean environment and a 600-meter deep ocean environment.

In the coastal ocean environment, the collected noise data were processed by coherently stacking five days of cross-correlation functions between pairs of hydrophones separated by 5 km, 10 km and 15 km, respectively. NCF waveforms were modeled using the KRAKEN normal mode model, with the difference between the NCFs and the acoustic GFs quantified by a weighting function. Through waveform inversion of NCFs, an optimal geoacoustic model was obtained by minimizing the two-norm misfit between the simulation and the measurement. Using a simulated time-reversal mirror, the extracted GF was back propagated from the receiver location to the virtual source, and a strong focus was found in the vicinity of the source, which provides additional support for the optimality of the aforementioned geoacoustic model. With the extracted GF, dispersion in experimental shallow water environment was visualized in the time-frequency representation. Normal modes of GFs were separated using the time-warping transformation. By separating the modes in the frequency domain of the time-warped signal, we isolated modal arrivals and reconstructed the NCF by summing up the isolated modes, thereby significantly improving the signal-to-noise ratio of NCFs. Finally, these reconstructed NCFs were employed to estimate the depth-averaged current speed in the Florida Straits, based on an effective sound speed approximation.

In the mid-deep ocean environment, the noise data were processed using the same noise interferometry method, but the obtained NCFs were not as good as those in the coastal ocean environment. Several highly possible reasons of the difference in the noise interferometry performance were investigated and discussed. The first one is the noise source composition, which is different in the spectrograms of noise records in two environments. The second is strong ocean current variability that can result in coherence loss and undermine the utility of coherent stacking. The third one is the downward refracting sound speed profile, which impedes strong coupling between near surface noise sources and the near-bottom instruments.

The active method of inverse filter processing was tested in a long-range deep-ocean environment. The high-power sound source, which was located near the sound channel axis, transmitted a pre-designed signal that was composed of a precursor signal and a communication signal. After traveling 1428.5 km distance in the north Pacific Ocean, the transmitted signal was detected by the receiver and was processed using the inverse filter. The probe signal, which was composed of M sequences and was known at the receiver, was utilized for the GF extraction in the inverse filter; the communication signal was then interpreted with the extracted GF. With a glitch in the length of communication signal, the inverse filter processing method was shown to be effective for long-range low-frequency deep ocean acoustic communication.

In summary, this dissertation explored two creative methods to extract the acoustic GFs in the ocean. The extracted acoustic GFs were utilized both for studying the physical properties of the ocean and for underwater communication. The study combined experimental data analysis and numerical simulation, using various signal processing techniques. This work is valuable in both passive acoustic remote sensing and active acoustic communication.

To my family.

Acknowledgments

I owe my sincere gratitude to many people who helped me on this dissertation.

First of all, I want to thank my adviser, Dr. Michael Brown, for his continuous support, professional guidance and great patience throughout my study and research. His wisdom and knowledge inspires me to conduct creative and original research. Without his experienced guidance, I cannot accomplish my Ph.D. study so smoothly.

I would like to express my sincere gratitude to my dissertation committee, Dr. Harry DeFerrari, Jorge Willemsen and Guoqing Lin, who offered me their insightful advices and suggestions on the dissertation. This dissertation cannot be completed without their help.

I want to thank our collaborators, Dr. Rex Andrew from APL/UW, and Dr. Oleg Godin from ESRL/NOAA, for their excellent cooperation in the two projects I've worked on. It has been such a pleasure to work and communicate with them.

I want to thank our technician and engineer, Michael Rebozo and Neil Williams, for their excellent work in designing, making and deploying the mooring equipments. I also want to thank the Walton Smith crew members for their professional work in the six research cruises, and many student volunteers who participated in these cruises, including Jeoffrey Banker, Chuntao Lu, Astrid Werkmeister, Macarena Ortiz, Alexis Denton,

Peng Wang, Shitao Wang and many others. Without their help, we cannot obtain the good quality data that are the basis of this dissertation.

I also want to give many thanks to Dr. Ying-Tsong Lin from WHOI, who shared the PE model source codes with me, for his great help in running the RAMPE model.

Most of all, I would like to acknowledge my family for their love and support, which warms me a lot when I am lonely. Many thanks to my friends who have accompanied me in the past five years and made my journey in Miami a beautiful memory. Last but not least, I would give my appreciation to my boyfriend, Zhiyang Huang, for his love and encouragement when I was depressed. This dissertation cannot be achieved without the love from my family and friends.

This dissertation work is funded by the US National Science Foundation, grants OCE1129860 and OCE1129524, and the US Office of Naval Research, grants N0001415122245 and N000141210182.

Contents

List of Figures

List of Tables

Chapter 1

Introduction

1.1 Acoustic Green's function in the ocean

1.1.1 What is acoustic Green's function

Mathematically, the acoustic Green's function is the solution to the acoustic wave equation, when boundary conditions are specified and the source function is a delta function. The transient acoustic Green's function in the ocean, which is also referred to as impulse response function or system function in the underwater communication community, is determined by the physical properties of relevant underwater environment. Given a specific ocean environment, with the known locations of the source and the receiver, the Green's function between these two locations can be obtained either analytically or numerically. The underwater communication problem can be viewed as a dynamic linear system, or a sound propagation waveguide; the input is the transmitted signal at the source location, while the output is the received signal at the receiver location. In this sense, Green's function is the system function, which represents the physical properties of the system; or an impulse response function, which is the output/response signal when the input signal is an impulse.

While its definition is relatively simple, the calculation of the acoustic Green's function in an ocean environment can be very complicated. Firstly, the ocean is a constantly varying dynamic system, which means that its physical properties change with time and location. The sound speed, which depends on temperature, salinity and pressure, varies with space and time, which adds complexity in solving the acoustic wave equation. Secondly, the boundary conditions for acoustic wave equation in an ocean environment are not easy to deal with. For the upper interface with the air, it's appropriate to approximate it with a pressure-release free surface under most circumstances. For the ocean bottom, some types of seafloor geoacoustic model are widely used, including the ideal (free-surface and rigid-bottom) waveguide model, half-space Pekeris model and other multi-layer models. Note that seafloor topography should also be carefully considered when the bathymetric variation is comparable with the wavelength, i.e. the range dependency is required in solving the acoustic equation. With the complexities mentioned above, Green's function cannot be extracted analytically for most cases. Thus, numerical models based on good approximations are usually the effective ways to compute the acoustic Green's function in the ocean.

1.1.2 Why do we study acoustic Green's function in the ocean

Extraction of acoustic Green's function is of great importance and significance. The acoustic Green's function is the key to understand the physics of the ocean acoustic environment. For example, from the Green's function, dispersive propagation properties can be analyzed and utilized in shallow water. In the field of underwater communication, especially for the deep-ocean long-range communication, once the Green's function is known, the transmitted signal can be effectively recovered from the received signal, i.e. Green's function is the key to underwater communication. In acoustical oceanography, physical properties of the ocean environment, including temperature, current speed, seafloor structure, etc., can be estimated from the acoustic Green's function; by monitoring the variation of the Green's function, changes of the environment can be analyzed accordingly.

1.1.3 How to extract acoustic Green's function in the ocean

In real ocean, extraction of acoustic Green's function is very challenging. Firstly, the ocean environment varies with time. Therefore the acoustic Green's function varies with time. Secondly, the ocean is an inhomogeneous moving medium which is significantly affected by multiple factors, including waves, tides, winds, currents, and so on. Thus theoretical studies usually need good approximations and assumptions, in order to solve the acoustic wave equation with corresponding boundary conditions. Thirdly, getting data from real ocean environment is challenging and costly, and the data quality is sometimes poor. Thus, extracting the acoustic Green's function of the ocean with low cost, high accuracy and short computation time is a goal of underwater acoustic researchers.

Experimental methods to estimate Green's functions are in principal best in that they correspond to the true environment. Experimental methods to extract ocean acoustic Green's functions can be categorized as active methods and passive methods. Active methods are based on the usage of controlled active man-made sources. Traditionally, active methods have been used to experimentally measure Green's functions. The main downside of active methods is the high cost for construction and implementation. Also, concerns relating to effects on marine animals have led to a complicated set of regulations. Therefore, in many cases, the passive method is very popular and important, as it doesn't need any controlled man-made sources. But its cost could be the sacrifice in data quality and computation complexity; especially, in certain cases, more efforts are required in exploring the acoustic theory and developing new signal processing methods. Acoustic researchers work to find a balance between the advantages and disadvantages of passive and active methods, and find a good solution to a given environment.

In this dissertation, we present two methods to extract the transient acoustic Green's function: the method of Noise Interferometry (NI), which is purely passive and needs longer computation time and lower construction cost, as well as the method of Inverse Filter Processing (IFP), which is active and needs shorter computation time and higher construction cost. It should be noted that due to the complexity of ocean environment, there is no universal method that applies to all types of environment. Every method has its own advantages and disadvantages under certain circumstances. Thus our study of these two methods focuses on different types of environment, and we will evaluate their performances and explore their limits to provide guidance for future applications.

1.2 Ocean acoustic noise interferometry: theory and literature review

1.2.1 Theory

The method to extract the acoustic Green's function (GF) from the cross-correlation function between the ambient noise at two locations is referred as Noise Interferometry (NI). The underlying physics of this method is: ambient noise waves, which connect two receivers, are coherent and carry information about the physical properties of the environment; by cross-correlating the concurrent noise recorded at two locations and coherently stacking many realizations of correlations, the coherent structure of the acoustic GF will emerge above the non-coherent background. Following Brown (2014), a general derivation of the basic result used in NI is derived below.

Assuming that the environment is stationary, and dissipation is weak, we formulate the acoustic NI problem in terms of the acoustic pressure p, since it is the quantity that is normally measured. At the very beginning, we neglect the effect of dissipation. The time-dependent acoustic pressure $p(\mathbf{x}|\mathbf{x}_0, t)$ at position $\mathbf{x}$ due to a transient point source, at position $\mathbf{x}_0$ and with time history $s(t)$, satisfies wave equation

$$(\nabla^2 - \frac{1}{c^2(\mathbf{x})}\frac{\partial^2}{\partial t^2})p(\mathbf{x}|\mathbf{x}_0, t) = -\delta(\mathbf{x} - \mathbf{x}_0)s(t). \tag{1.1}$$

Equivalently, $p(\mathbf{x}|\mathbf{x}_0, t) = s(t) * G(\mathbf{x}|\mathbf{x}_0, t)$ ($*$ stands for convolution) where the Green's function satisfies

$$(\nabla^2 - \frac{1}{c^2(\mathbf{x})}\frac{\partial^2}{\partial t^2})G(\mathbf{x}|\mathbf{x}_0, t) = -\delta(\mathbf{x} - \mathbf{x}_0)\delta(t). \tag{1.2}$$

In the frequency domain, $\bar{p}(\mathbf{x}|\mathbf{x}_0, \omega) = \bar{s}(\omega)\bar{G}(\mathbf{x}|\mathbf{x}_0, \omega)$ where $\bar{G}(\mathbf{x}|\mathbf{x}_0, \omega)$ satisfies

$$(\nabla^2 + k^2(\mathbf{x}))\bar{G}(\mathbf{x}|\mathbf{x}_0, \omega) = -\delta(\mathbf{x} - \mathbf{x}_0) \tag{1.3}$$

with $k^2(\mathbf{x}) = \frac{\omega^2}{c^2(\mathbf{x})}$.

In an unbounded homogeneous environment, the Green's function in the frequency domain is

$$\bar{G}(\mathbf{x}|\mathbf{x}_0, \omega) = \frac{e^{ikr}}{4\pi r}, \tag{1.4}$$

and the Green's function in time domain is

$$G(\mathbf{x}|\mathbf{x}_0, t) = \frac{\delta(t - \frac{r}{c})}{4\pi r}, \tag{1.5}$$

where $r = |\mathbf{x} - \mathbf{x}_0|$.

We further assume a random distribution of discrete point sources at positions $\mathbf{x}_i$ and with time histories $s_i(t)$. Then the contribution to the acoustic pressure at location $\mathbf{x}_A$ from the source at location $\mathbf{x}_i$ is

$$p(\mathbf{x}_A|\mathbf{x}_i, t) = s_i(t) * G(\mathbf{x}_A|\mathbf{x}_i, t). \tag{1.6}$$

Similarly, the acoustic pressure at $\mathbf{x}_B$ due to the source at $\mathbf{x}_j$ is

$$p(\mathbf{x}_B|\mathbf{x}_j, t) = s_j(t) * G(\mathbf{x}_B|\mathbf{x}_j, t). \tag{1.7}$$

Now sum up the contributions from all of the random sources and compute the cross-correlation of the acoustic pressures at locations A and B:

$$\begin{aligned} C_{AB}(t) &= \sum_i p(\mathbf{x}_A|\mathbf{x}_i, t) * \sum_j p(\mathbf{x}_B|\mathbf{x}_j, -t) \\ &= \sum_i \sum_j s_i(t) * G(\mathbf{x}_A|\mathbf{x}_i, t) * s_j(-t) * G(\mathbf{x}_B|\mathbf{x}_j, -t) \\ &= D(t) * \sum_i G(\mathbf{x}_A|\mathbf{x}_i, t) * G(\mathbf{x}_B|\mathbf{x}_i, -t). \end{aligned} \tag{1.8}$$

We have assumed that the acoustic sources are independent and approximately δ-correlated, i.e.

$$s_i(t) * s_j(-t) = \delta_{ij} D(t). \tag{1.9}$$

The above argument can be modified to account for a continuum of sources. The result is

$$C_{AB}(t) = D(t) * \int\int\int d\mathbf{x} G(\mathbf{x}_A|\mathbf{x}, t) * G(\mathbf{x}_B|\mathbf{x}, -t). \tag{1.10}$$

In the presence of weak dissipation, which is assumed to be proportional to ω times the parameter $\frac{\epsilon}{2}$, the Green's function $\bar{G}(\mathbf{x}|\mathbf{x}_A, \omega)$ at $\mathbf{x}$, corresponding to point source excitation at $\mathbf{x}_A$, satisfies

$$(\nabla^2 + k^2 + \frac{i\omega\epsilon}{2})\bar{G}(\mathbf{x}|\mathbf{x}_A, \omega) = -\delta(\mathbf{x} - \mathbf{x}_A). \tag{1.11}$$

Similarly, $\bar{G}$ at point $\mathbf{x}$ excited by a point source at $\mathbf{x}_B$ satisfies

$$(\nabla^2 + k^2 + \frac{i\omega\epsilon}{2})\bar{G}(\mathbf{x}|\mathbf{x}_B, \omega) = -\delta(\mathbf{x} - \mathbf{x}_B). \tag{1.12}$$

Due to reciprocity, $\bar{G}(\mathbf{x}|\mathbf{x}_A, \omega)$ is equal to $\bar{G}(\mathbf{x}_A|\mathbf{x}, \omega)$, and $\bar{G}(\mathbf{x}|\mathbf{x}_B, \omega)$ is equal to $\bar{G}(\mathbf{x}_B|\mathbf{x}, \omega)$. Multiplication of Eq.(1.11) by $\bar{G}^*(\mathbf{x}_B|\mathbf{x}, \omega)$, followed by integration over $\mathbf{x}$, and complex conjugation of left- and right-hand sides gives

$$\int\int\int d\mathbf{x}\ \bar{G}(\mathbf{x}_B|\mathbf{x}, \omega)(\nabla^2 + k^2 - \frac{i\omega\epsilon}{2})\bar{G}^*(\mathbf{x}_A|\mathbf{x}, \omega) = -\bar{G}(\mathbf{x}_B|\mathbf{x}_A, \omega). \tag{1.13}$$

Multiplication of Eq.(1.12) by $\bar{G}^*(\mathbf{x}_A|\mathbf{x}, \omega)$, followed by integration over $\mathbf{x}$ gives

$$\int\int\int d\mathbf{x}\ \bar{G}(\mathbf{x}_A|\mathbf{x}, \omega)(\nabla^2 + k^2 + \frac{i\omega\epsilon}{2})\bar{G}^*(\mathbf{x}_B|\mathbf{x}, \omega) = -\bar{G}(\mathbf{x}_A|\mathbf{x}_B, \omega). \tag{1.14}$$

Subtracting Eq.(1.14) from Eq.(1.13) gives

$$Q - i\omega\epsilon\int\int\int d\mathbf{x}\ \bar{G}(\mathbf{x}_B|\mathbf{x}, \omega)\bar{G}^*(\mathbf{x}_A|\mathbf{x}, \omega) = \bar{G}^*(\mathbf{x}_A|\mathbf{x}_B, \omega) - \bar{G}(\mathbf{x}_B|\mathbf{x}_A, \omega), \tag{1.15}$$

where

$$\begin{aligned} Q &= \int\int\int d\mathbf{x}\ \bar{G}(\mathbf{x}_B|\mathbf{x}, \omega)\nabla^2\bar{G}^*(\mathbf{x}_A|\mathbf{x}, \omega) - \int\int\int d\mathbf{x}\ \bar{G}^*(\mathbf{x}_A|\mathbf{x}, \omega)\nabla^2\bar{G}(\mathbf{x}_B|\mathbf{x}, \omega) \\ &= \int\int d\sigma\ [\bar{G}(\mathbf{x}_B|\mathbf{x}, \omega)\nabla\bar{G}^*(\mathbf{x}_A|\mathbf{x}, \omega) - \bar{G}^*(\mathbf{x}_A|\mathbf{x}, \omega)\nabla\bar{G}(\mathbf{x}_B|\mathbf{x}, \omega)] \cdot \hat{n}. \end{aligned} \tag{1.16}$$

By reciprocity $\bar{G}(\mathbf{x}_B|\mathbf{x}_A, \omega) = \bar{G}^{(}\mathbf{x}_A|\mathbf{x}_B, \omega)$, so the rhs of Eq.(1.15) can be written $-2\ Im\ \bar{G}(\mathbf{x}_B|\mathbf{x}_A, \omega)$. The second form of Q given above follows from applying the divergence theorem to $\int\int\int d\mathbf{x}\ \nabla\cdot[\bar{G}(\mathbf{x}_B|\mathbf{x}, \omega)\nabla\bar{G}^*(\mathbf{x}_A|\mathbf{x}, \omega) - \bar{G}^*(\mathbf{x}_A|\mathbf{x}, \omega)\nabla\bar{G}(\mathbf{x}_B|\mathbf{x}, \omega)]$. The integral in the latter form of Q is a surface integral over the boundary of the $\mathbf{x}$-domain and $\hat{n}$ is a unit outward normal. That integral vanishes under most conditions of interest. In an unbounded homogeneous environment, consider the domain enclosed within a large sphere of radius R centered at the midpoint between $\mathbf{x}_A$ and $\mathbf{x}_B$. Owing to dissipation, for sufficiently large R, $\bar{G}$ and $\nabla\bar{G}\cdot\hat{n}$ approach zero faster than R^{-1}, so Q approaches 0 in the large R limit. Note also that in an $\mathbf{x}$-domain bounded by a combination of rigid walls (where $\nabla\bar{G}\cdot\hat{n} = 0$) and pressure release surfaces (where $\bar{G} = 0$), each term in Q vanishes so $Q = 0$. Setting $Q = 0$ in Eq.(1.15) gives

$$-i\omega\epsilon\int\int\int d\mathbf{x}\ \bar{G}(\mathbf{x}_B|\mathbf{x}, \omega)\bar{G}^*(\mathbf{x}_A|\mathbf{x}, \omega) = \bar{G}^*(\mathbf{x}_A|\mathbf{x}_B, \omega) - \bar{G}(\mathbf{x}_B|\mathbf{x}_A, \omega). \tag{1.17}$$

Transforming to the time domain gives

$$\epsilon\frac{d}{dt}\int\int\int d\mathbf{x}\ G(\mathbf{x}_B|\mathbf{x}, t) * G(\mathbf{x}_A|\mathbf{x}, -t) = G(\mathbf{x}_B|\mathbf{x}_A, -t) - G(\mathbf{x}_A|\mathbf{x}_B, t), \tag{1.18}$$

where * denotes convolution. Recall that the convolution of $G(\mathbf{x}_B|\mathbf{x}, t)$ and $G(\mathbf{x}_A|\mathbf{x}, -t)$ is equivalent to the cross-correlation of $G(\mathbf{x}_B|\mathbf{x}, t)$ and $G(\mathbf{x}_A|\mathbf{x}, t)$.

Finally, differentiating Eq.(1.10) and making use of Eq.(1.18) gives

$$\frac{d}{dt}[\epsilon C_{AB}(t)] = D(t) * [G(\mathbf{x}_B|\mathbf{x}_A, -t) - G(\mathbf{x}_A|\mathbf{x}_B, t)]. \tag{1.19}$$

Dissipation plays an important role in the arguments leading to Eq.(1.19). The assumptions that we have made about the distribution and time history of the sources lead to a divergent C_{AB} in the limit $\epsilon \to 0$; that is a singular limit. More generally, $C_{AB}(t)$ increases in magnitude with decreasing ϵ. For small ϵ we may think of $\epsilon C_{AB}(t)$ as the effective correlation function and approximate this quantity as a constant times a long-, but finite-, time approximation to the correlation function, and replace the Green's functions on the rhs of Eq.(1.19) with their dissipationless counterparts. (This argument can be made rigorous if it can be shown that the limit as $\epsilon \to 0$ of $\epsilon C_{AB}(t)$ is well-defined and can be approximated by evaluating this expression at small ϵ.)

1.2.2 Literature review

The basic idea of extracting Green's functions from ambient noise can be traced back to Claerbout's conjecture (1968). In his conjecture, Claerbout stated that in three-dimensional heterogeneous media, simply by listening to noise at two receivers, we could construct the signal that would have been observed at one location if there had been a source at the other location. This conjecture was theoretically proved by Weaver and Lobkis in 2001, under the assumption of diffuse noise field. Following the work of Weaver and Lobkis, Derode *et al.* (2003) derived the same theory through an analogy with a time-reversal experiment; Wapenaar (2004) did the derivation in the view of reciprocity theorem; Snieder (2004) completed the derivation through the principle of stationary phase.

By now, the theory of NI has been demonstrated in experiment in multiple research areas. In ultrasonics, Weaver and Lobkis (2001) firstly confirmed the applicability of NI through cross-correlating thermal ultrasonic noise in reverberant cavities. In seismology, Campillo and Paul (2003) produced the first account of geophysical interferometric impulse response reconstruction using seismic ambient noise. Bakulin and Calvert (2004) produced the first practical application of seismic interferometry in an exploration setting. The application of interferometrically constructed impulse responses for tomographic velocity inversion was shown by Shapiro *et al.* (2005) and by Sabra *et al.* (2005b). In helioseismology, Duvall *et al.* (1993) showed that it is possible to extract time-distance information from temporal cross-correlation of intensity fluctuations on the solar surface, which can help to study local solar phenomena such as subsurface inhomogeneities near sunspots. In addition, Rickett and Claerbout (1999) also validated the conjecture that impulse response seismograms could be extracted through cross-correlation of noise traces via the method of Kolmogoroff spectral factorization. Extraction of the Green's function from cross-correlations of ambient noise has also been applied to remote structural health monitoring (Duroux *et al.*, 2009), muscular activity monitoring (Sabra *et al.*, 2007), and the gross structure of Earth's atmospheric boundary layer imaging (Haney, 2009). In underwater acoustics, extracting Green's functions from ambient noise cross-correlations in the ocean has also been demonstrated. Inverted fathometer application, which corresponds to one-dimension vertical propagation, have been shown to be successful [Siderius *et al.*, 2006, 2010; Gerstoft et al., 2008]. Several demonstrations of horizontal propagation have also shown to be successful [Fried *et al.*, 2008; Brooks and Gerstoft, 2009; Godin *et al.*, 2011; Lani *et al.*, 2012; Fried *et al.*, 2013; Brown *et al.*, 2014], with the ranges varying from a few hundred meters to 10 kilometers. Ocean current speed, which breaks the acoustic reciprocity, has been calculated from the noise correlation functions in a coastal ocean environment [Godin *et al.*, 2014].

1.3 Dissertation overview

The main body of this thesis is composed of four chapters. Chapters 2,3,4 are based on the passive method of noise interferometry, which are tested in two environments in the Florida Straits. Chapter 5 is about the active method of inverse filter processing, which studies long-range deep-ocean acoustic communication.

For noise interferometry method, field experiments, raw data, and data processing method are discussed in Chapter 2, where the ambient noise cross-correlation functions are calculated with noise data in both a coastal ocean environment and a mid-depth ocean environment. The performance of noise interferometry in the two studied environments are compared and possible factors that affect the noise interferometry performance are discussed.

Chapter 3 describes waveform modeling of the ambient noise cross-correlation function, aiming to quantify the relationship between the acoustic Green's function and the noise correlation function. Through waveform inversion, an optimal geoacoustic model, which fits the real environment very well, is obtained. The optimal geoacoustic model is then validated with time-reversal mirror, which verifies the feasibility of applying time-reversal mirror to passive acoustic remote sensing.

Chapter 4 firstly illustrates the dispersion in the coastal ocean environment. Then, using time warping technique, the modal arrivals of noise correlation functions are successfully separated. By summing up the isolated modes, the noise correlation functions are reconstructed and the signal-to-noise ratio is improved. Lastly, from the reconstructed noise correlation functions, the depth-averaged current speed is estimated.

For the inverse filter processing method, Chapter 5 summarizes the theory, method and experiment results.

Chapter 6 summarizes above chapters in the context of acoustic Green's function extraction and concludes the main results of the thesis. In addition, limitations of current work and topics for future studies are also discussed in the conclusion chapter.

Chapter 2

Ocean Acoustic Noise Interferometry: Experiment and Data Processing

2.1 Noise interferometry experiment in the Florida Straits

2.1.1 Three deployment cruises

To collect ambient noise data for the study of noise interferometry, we performed three field experiments in the Florida Straits. In each experiment, we deployed three sets of autonomous sound recording systems in the ocean. Each sound recording system was composed of a hydrophone, multiple batteries, a data-recording unit, and a taut mooring, with the hydrophone located 5 m off the seafloor. The electronics and recording unit were based on commercial units from Loggerhead Instruments. The three deployments were performed in different ocean environment. Figure 2.1 shows the locations of three deployments. As illustrated by the bathymetric lines, in deployment 1, the three sound recording systems were aligned in line following a 100-m deep isobath; in deployment 2, the systems were aligned in line approximately following a 600-m isobath; in deployment 3, the instruments were deployed in triangle shape, in 800-m deep water. The bathymetric variation in deployment 2 was stronger than in deployments 1 and 3. The three environments were selected for study since we intended to analyze the effect of environmental properties on the performance of noise interferometry.

In deployment 1 and 2, we label the three instruments from north to south as instrument 1, 2 and 3. The separation between 1-2, 2-3 and 1-3 instrument pair were 5 km, 10 km and 15 km, respectively. In deployment 3, the range between 1-2 and 2-3 instrument pair was 5 km and 10 km approximately. The separations were designed to evaluate the performance of noise interferometry as instrument separation increases. It should be noted that the separations were calculated from the ship-based GPS at the time of deployment, but there could be slight drift during the descent of

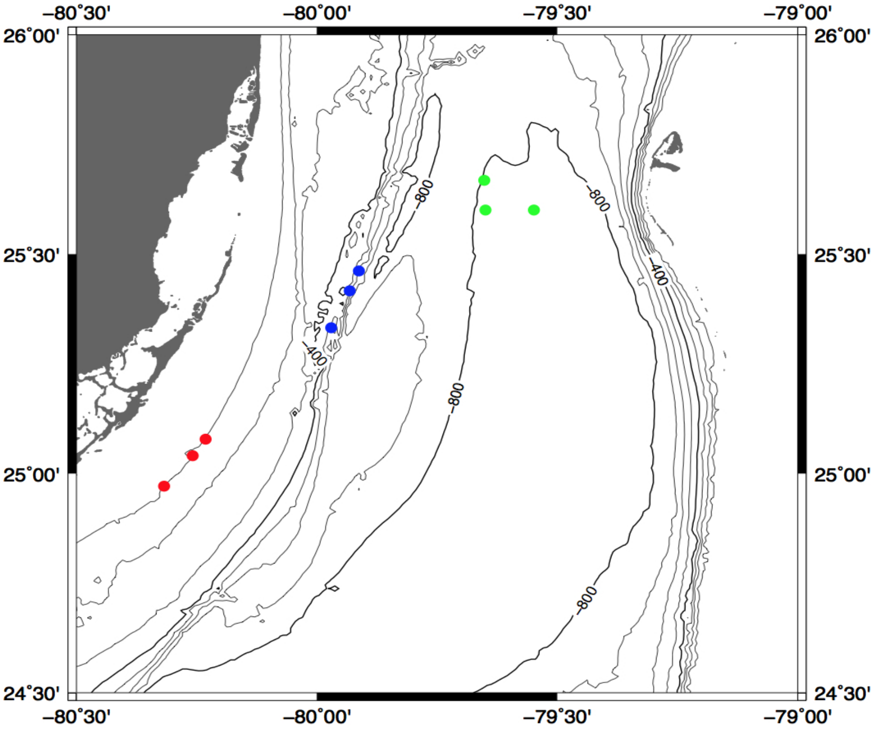

Figure 2.1: Map of experiment location of three deployments. Red dots: deployment 1; blue dots: deployment 2; green dots: deployment 3.

each instrument. This matter will be explained later on in the waveform modeling in Chapter 3.

In each experimental environment, we did one deployment cruise and one recovery cruise. Each sound recording system was designed to record ambient noise continuously without interruptions between the deployment cruise and recovery cruise. Deployment 1 was deployed in December 2012, and recovered in February 2013. Deployment 2 was initiated in September 2013, and recovered in October 2013. Deployment 3 was started in September 2014, and recovered in October 2014. The duration was designed to up to three month so that we can evaluate the temporal variation of the noise interferometry performance.

2.1.2 Data

The ambient acoustic noise was recorded at 8 kHz sampling frequency by each recording system. The recorded noise data were saved as one data file every 625.024 second, that is 5,000,192 sampling points. That means, about 138 data files were generated in one day at each instrument. For deployment 1, about three months of data were collected. For deployments 2 and 3, about one month of data were obtained. The data files were originally saved on flash memory cards by the autonomous recording system and then carefully transported to hard drives in laboratory after recovery cruise.

A key factor that affected the ambient noise data quality is the clock stability of each recording instrument, since the noise interferometry processing requires cross-correlating two concurrent data records to obtain the cross-correlation functions. In our experiment, the three instrument clocks were synchronized prior to deployment by simultaneously sending a signal to all three instruments. In addition, a post-recovery synchronization pulse was transmitted simultaneously to all three recording units, so that the clock drift can be evaluated and corrected after recovery. In deployment 1, instrument 2 stopped recording continuously after about the sixth day since deployment. The other instruments behaved similarly, but with longer gap-free recording intervals. In deployment 2, the three instruments all worked well. In deployment 3, all three clocks exhibited excessive drift, and the data collected during this deployment were not suitable for noise interferometry. Thus, in the next sections of this chapter as well as the next two chapters, we only use the data collected in deployment 1 and 2.

To construct the sound speed profile (SSP), CTD casts were performed during the deployment cruises. The constructed SSP for deployment 1 and 2 are shown in Fig. 2.2. In deployment 1, the sound speed variation over 100-meter-depth is less than 5 m/s, i.e. the acoustic environment in deployment 1 is almost homogeneous. On the contrary, in deployment 2, sound speed decreases about 60 m/s from ocean surface to seafloor, and the thermocline is very obvious from 50 m to 300 m. We should keep in mind that deployment 1 was performed in winter while deployment 2 was performed in summer. From the SSP comparison, we can see that the acoustic environment in deployment 1 and 2 is very different, thus we can expect the difference in the noise interferometry applicability in these two types of environment.

During each cruise, the ADCP data were also collected for current speed analysis. Since we only estimate the current speed in deployment 1, we will save the ADCP data analysis for Chapter 4.

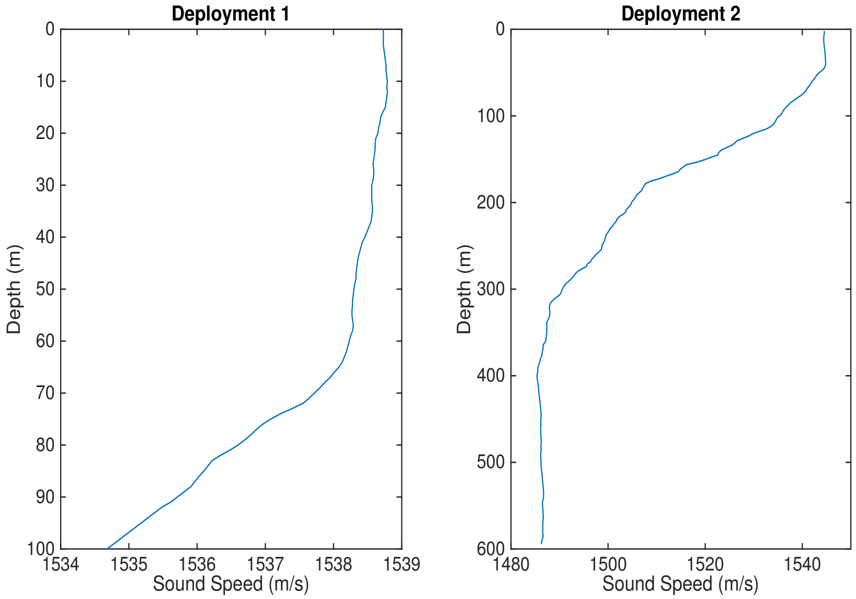

Figure 2.2: Sound speed profiles constructed from the conductivity-temperature-depth casts performed in deployment 1 (left panel) and deployment 2 (right panel).

2.2 Calculation of ambient noise cross-correlation functions

2.2.1 Data processing methods

The length of each segment in calculating one NCF realization is determined by the separation between the two sites, i.e. the arrival time for an impulse to propagate from one location to the other. In this way, we can guarantee that the deterministic structure of NCF and GF is fully kept. The raw data of ambient noise were processed by cross-correlating two concurrent records at two locations. Remember that each file of noise data is about 625 second long, with 5,000,192 sampling points. Since the separation between 1-2 and 2-3 instrument pairs are no more than 10 km, each realization of cross-correlation function corresponds to two 65536-point-long segments of noise data file and yields a 131072-point-long cross-correlation function. For the

1-3 instrument pair, where the separation was about 15 km, each realization of cross-correlation function corresponds to two 131072-point-long segments of noise data file and yields a 262145-point-long cross-correlation function.

To calculate the cross-correlation functions, we firstly transform each segment of noise data at both receivers to the frequency domain, then take the product of the Fourier transform at one receiver with the complex conjugate of the Fourier transform at the other receiver. The inverse transform of the conjugate product yields the cross-correlation function in time domain. Note that to suppress the effects of a rapid variation of the noise power spectrum with frequency, before the inverse Fourier transform, the cross-spectrum is normalized by amplitude, i.e. we are evaluating the inverse transform of the coherence function. After coherently stacking many realizations of correlation functions, the deterministic structure of Green's function will emerge from the stacked correlation function.

Although the theory of noise interferometry is relatively simple, there are many procedures that need careful consideration in the process of data processing. In addition to the NCF calculation steps mentioned above, an important factor is the frequency band in which the NCFs are calculated. The sampling frequency was 8000 Hz, thus the maximum frequency for use is 4000 Hz. Through trial and error, we find that the frequency band from 20-100 Hz bands yield good NCF structures. This is reasonable since the low frequency signal is more coherent than high frequency counterpart. In the Results section, the frequency band for each NCF will be explained individually.

2.2.2 Clock drift correction

As discussed in previous section, the clock stability of each recording system is a key requirement to the quality of stacked correlation functions. Thus, in the calculation of each realization of correlation functions, we should carefully remove the relative clock drift between the two instruments. Since the clock drift of each system is unknown, we assume that the relative clock drift between two instruments is linear. This behavior is consistent with laboratory-based monitoring of relative drifts between three clocks.Relative clock drifts were estimated using two different methods. For deployment 1, results presented here were measured by maximizing the signal-to-noise ratio of the stacked NCF. It should be clarified that the signal-to-noise ratio of the stacked NCF refers to the energy ratio of the coherent signal to the non-coherent signal. The coherent signals that correspond to the arrival of GFs are viewed as "signal", while the incoherent signals that arrive before and after the GF structures are taken as "noise". For the 1-2 instrument pair, we search for clock drift in the span of 0.1 to 1.5 ms/day. For the 2-3 instrument pair, we search for the clock drift in the span of -0.1 to -1.0 ms/day. These bounds are based on the estimates presented in Godin *et al.* (2014). The highest SNR happens when the clock drift is 1.1 ms/day for 1-2 instrument pair, and -0.5 ms/day. Since the relative clock drift between 1-3 instrument pair is dependent on 1-2 and 2-3 instrument pair $\triangle_{13} = \triangle_{12} + \triangle_{23}$, here we take the clock drift between 1-3 instrument pair as 0.6 ms/day.Then, for the deployment 2, the clocks on three instruments all work well during the whole experiment period. Thus, we use the synchronization signals, which were transmitted before deployment and after recovery in the lab, to calculate the relative clock drift. Again, we assume that the relative clock drift between two instruments were linear. As a result, we find that the relative clock drift for 1-2 and 2-3 pairs were 1.2 ms/day and -0.8 ms/day, respectively.

2.3 Results

2.3.1 Deployment 1: shallow water environment

With the aforementioned signal processing method and clock drift corrections, we coherently stack five days of concurrent cross-correlation functions of deployment 1, where the water depth is about 100 m. The results are shown in Fig. 2.3. By comparing panel (a), (c) and (e), we can see that the SNR decreases as the separation increases. $C_{12}(t)$ has the strongest signal. $C_{23}(t)$ gets noisier but the deterministic structure is still clear in both positive and negative lags. In $C_{13}(t)$, the deterministic structure is severely blurred by the noise, especially in the negative lag. It should be noted that in spite of the SNR, all stacked NCFs show correct arrival time of the deterministic structure, which is an indication of success of noise interferometry in the studied shallow water environment. Panel (b), (d) and (e) in Fig. 2.3 illustrate the difference between the positive lag and the negative lag in each NCF. In the three NCFs, the phase difference between two lags is obvious. This should be mainly attributed to the effect of ocean current, and will be investigated in Chapter 4. The amplitude difference in $C_{12}(t)$ is minimal among all three NCFs. In $C_{23}(t)$ and $C_{13}(t)$, the amplitude difference between two lags are more obvious. It may be attributed to the asymmetry of noise sources distribution. The frequency band of NCF calculations for 1-2 and 2-3 instrument pair is 20-70 Hz band, while the frequency band for 1-3 instrument pair is 20-50 Hz.

2.3.2 Deployment 2: mid-depth ocean environment

Using the same data processing procedures, the ambient noise cross-correlation functions are calculated for deployment 2. Unlike deployment 1, the stacked NCFs in deployment 2 has very low signal-to-noise ratio, even for the 1-2 instrument pair at 5 km separation. To view the temporal variation of NCFs more clearly, we make a color plot of NCFs, where the color denotes the amplitude of the envelope of NCFs. Varying the coherent integration time interval reveals that both 1-2 and 2-3 instrument pairs show some deterministic structures in the 30-60 Hz band. To check the quality of extracted NCFs, we simulate the theoretical correlation function using the KRAKEN normal mode model, and compare with the experimental results. The results for 1-2 and 2-3 instrument pairs are shown in Fig. 2.4 and Fig. 2.5 respectively. In both figures, Panel (a) illustrates the intensity of the measured NCFs, and each horizontal stripe of the color plot represents a coherent stack of NCF over six days; Panel (b) plots the intensity of the analytical signal of simulated NCF, which is obtained with the KRAKEN normal mode model. From the comparison between Panel (a) and Panel (b), consistency between the measured NCF and the theoretical NCF can be evaluated. For the 1-2 instrument pair, two wave packets are clearly visible and are consistent over the whole time span in the negative lag; the pattern of the two wave packets are relatively weak in the positive lag, but they are still visible in some start days. For the 2-3 instrument pair, only one wave packet is clear and consistent in the positive lag, and three wave packets are visible but not very consistent. Overall, we can see solid and reliable consistency between the measurement and the simulation. SNR in 1-2 instrument pair is higher than the 2-3 instrument pair, and the deterministic structures are more consistent in 1-2 instrument pair than 2-3 instrument pair.

2.4 Discussion

From the results above, we've successfully extracted the ambient noise cross-correlation functions by coherently stacking many realizations of correlation functions of ambient noise recorded at two locations. However, the results in the coastal ocean environment of deployment 1 and in the mid-depth ocean environment of deployment 2 are not equally good. The deterministic structure in the stacked NCF of deployment 1 is much more clear than deployment 2. It is important to figure out why the performance of noise interferometry in the two studied environments is so different. In this section, we intend to explain the difference in the noise interferometry performance by investigating the difference in ambient sources and the acoustic properties of the two studied environments.

2.4.1 Noise source identification

The theory of noise interferometry requires the noise source to be diffusive, which means that the sources should be uncorrelated and evenly distributed in the medium of study. In the real ocean environment, the requirement of diffusive noise field is not satisfied over time intervals shorter than about a day. Spatially, the noise source distribution varies significantly with depth. Near the surface, wind-driven waves and nearby shipping generate large amount of noise; in the upper 100 m, where most biological activities exist, noise levels are higher than in the deeper ocean; near the bottom, seismic and volcanic activities contribute to low frequency noise components. In general, ocean environments are far from ideal medium for noise interferometry study. However, the good result of deployment 1 does demonstrate the applicability of noise interferometry in the experimental coastal ocean environment. Thereby, it's worth taking a look at the noise source components in the two studied environments. This work will provide useful guidance for future noise interferometry experiment.

Here, we examine the spectrogram of the noise data files. It should be noted that each noise data file is a mixture of sound generated by various sound sources, including distant ship traffic, wind-driven breaking waves, nearby shipping, marine animals, seismic activities, etc. Although sound source properties can be viewed and differentiated in the frequency domain, it is still impossible to identify/separate the noise sources exactly. From the spectrogram, we can grossly tell the possible noise sources, and get a clue to tell the difference of the source composition. Figure 2.6 shows the spectrogram of some records of two deployments in 0-100 Hz band, since the calculation of NCFs are all done in this band. Panels in the left column are from deployment 1, while panels in the right column are from deployment 2. All the spectrograms are calculated with the noise files of instrument 1. By comparison, it's clear that the spectrograms of two deployments have different features. Deployment 2 shows many vertical stripes of high noise level, which last about 20 minutes, and these are most likely generated by near-by shippings. Since the experiment location of deployment 2 are close to the Port of Miami, we expect that there are more ships passing right overhead of the noise recording systems. In addition, the spectrograms of deployment 2 have very consistent strong components in the band 0-25 Hz, whose origin is unknown. Since the NCFs for deployment 2 are calculated in 30-60 Hz band, we've carefully avoided the 0-25 Hz components. Spectrograms of deployment 1 have some special structures that are evenly distributed over frequency domain and last for about 2 hours. These structures are probably distant ships. Overall, the noise source compositions in the two deployments are different, which might cause the difference of noise interferometry performance in the two environments.

2.4.2 Environmental physics comparison: shallow water vs mid-deep ocean

The next thing we want to investigate is the acoustic properties of the two experimental environments. We know that the emergence of acoustic Green's function relies on sound waves that pass through both recording hydrophones. Therefore, with sufficient noise sources, another key factor is the likelihood for sound waves to travel through two hydrophones. Two conditions are desirable in this aspect. Firstly, since the noise sources between 20-100 Hz are mainly distributed near surface, the acoustic field has a dipole excitation pattern due to the image effect. Therefore, sound rays with steep angles relative to the surface are more favorable than flat angles in connecting two recording hydrophones. Secondly, at the ocean bottom, due to the need of full reflection, sound rays with flat angles relative to the bottom are desirable to connect two recording hydrophones. With these two conditions in mind, we compare the two studied environments. In the environment of deployment 1, sound speed is almost constant over 100-m water depth. Sound rays are almost straight lines, which approximately satisfy the above two conditions. For deployment 2, the sound speed varies significantly from the surface to the bottom. Due to Snell's law, sound rays bend towards the lower sound speed, i.e. downward at the surface. This pattern conflicts with both conditions. From this aspect, the coastal environment of deployment 1 is physically more favorable for noise interferometry than the mid-depth ocean environment of deployment 2.

2.5 Summary

In this chapter, we've introduced the three ocean experiments designed for the noise interferometry research. Each experiment was performed in a different ocean environment. Data processing procedures and the clock drift corrections that are very important to the NCF calculations are discussed in details. From there, we've successfully calculated the NCFs between two hydrophones from the data of deployment 1 and deployment 2. The results from deployment 1 and deployment 2 are presented and compared. To explore the reason of the difference in the noise interferometry performance of two deployments, we discussed the difference in noise source compositions as well as the acoustic properties of the two environments. The effort of this chapter gives important methodology reference of noise interferometry experiment and data processing. More importantly, we've got good-quality NCFs that are the basis of the next two chapters.

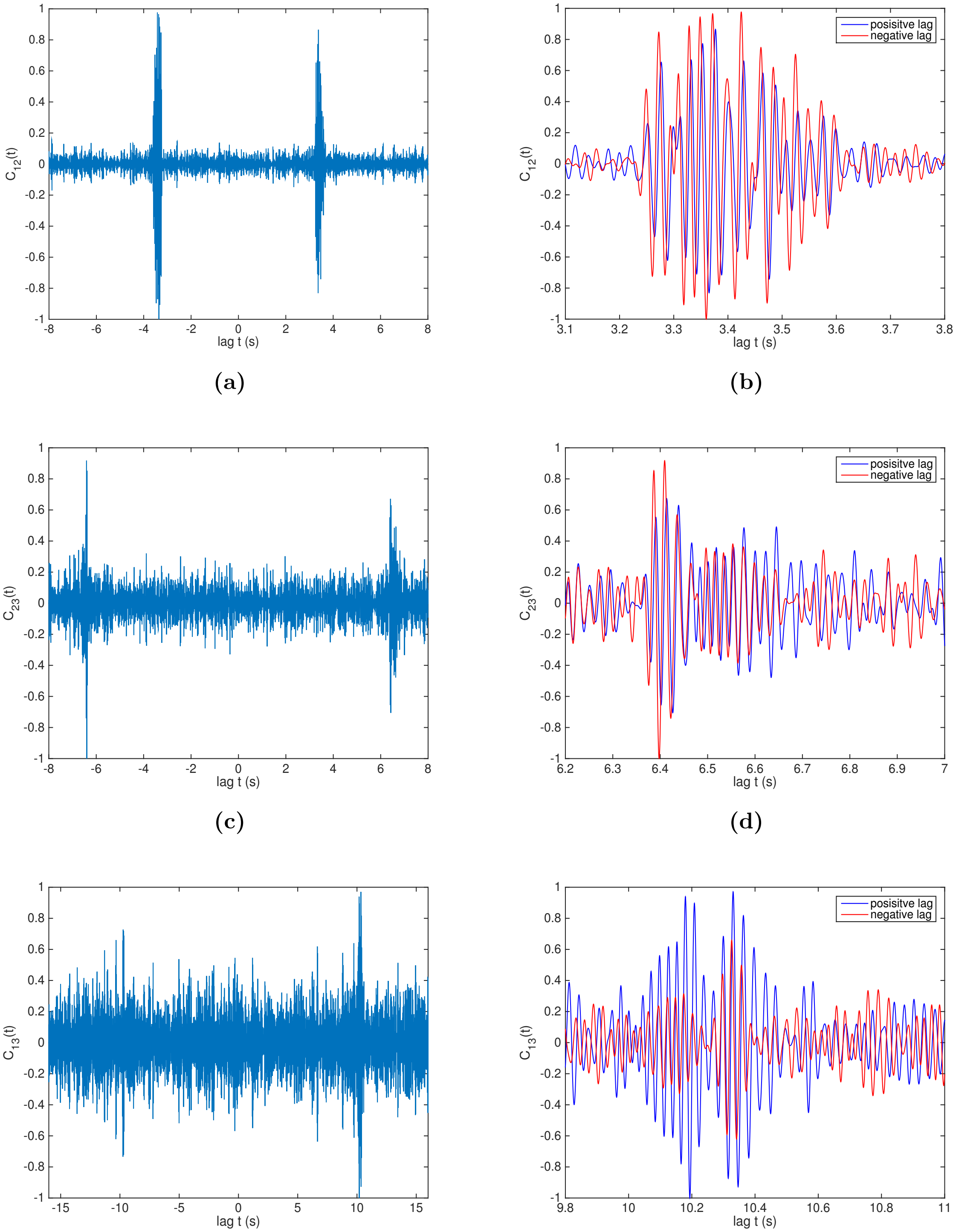

(a) **(b)**

(c) **(d)**

(e) **(f)**

Figure 2.3: Cross-correlation functions between 1-2, 2-3 and 1-3 instrument pair of deployment 1, obtained from five days of ambient noise data. Panel (b), (d), (f) show difference between the positive lags (in blue) and negative lags (in red).

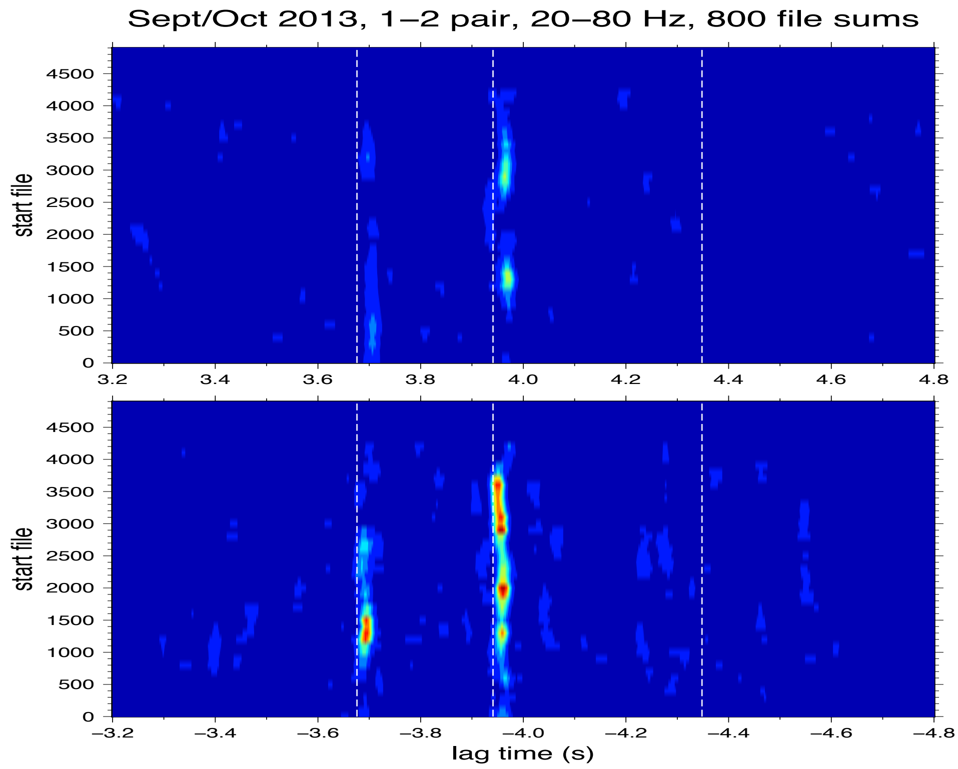

(a)

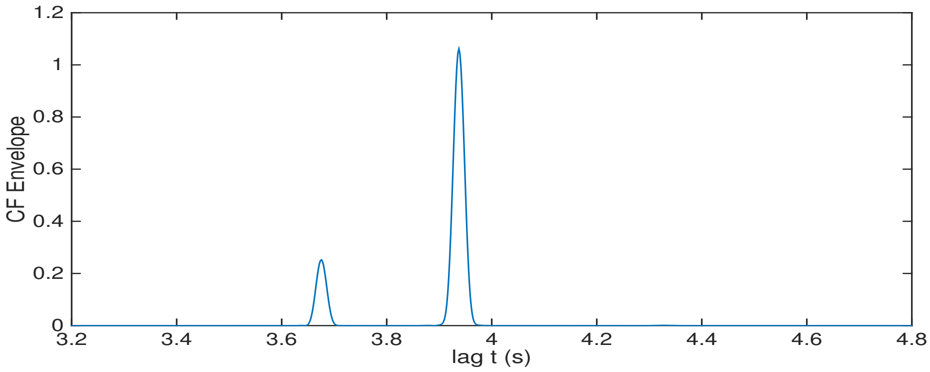

(b)

Figure 2.4: NCF intensity plots for the 1-2 instrument pair in deployment 2 show consistency between the measurement and simulation. (a) Squared modulus of the analytic signal of measured correlation functions throughout the duration of 34 days, with each horizontal stipe of the figure corresponding to a 800-file-stacked correlation function. White dotted lines correspond to ray arrivals from simulation. (b) The modulus of the analytic signal of simulated correlation function using the KRAKEN normal mode model.

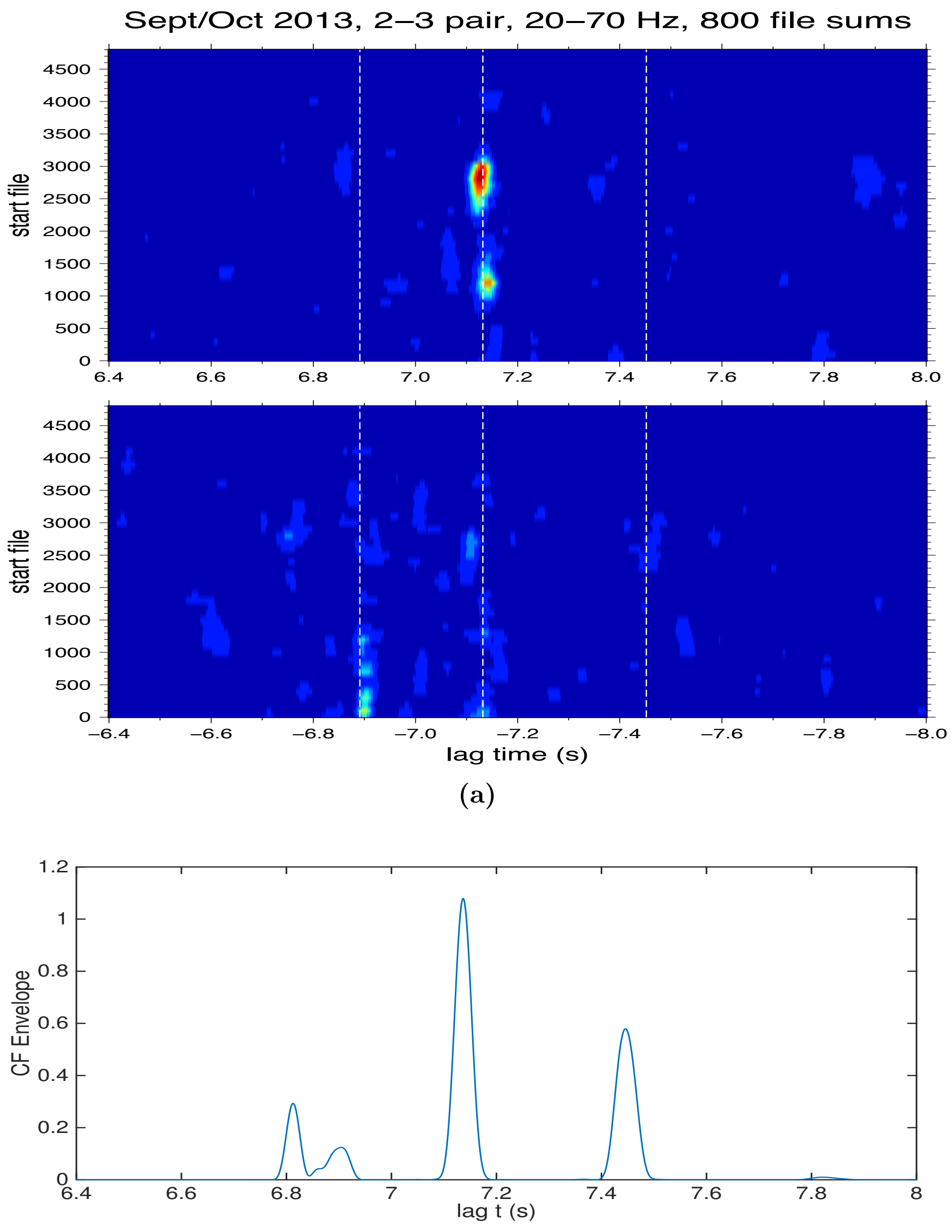

(a)

(b)

Figure 2.5: NCF intensity plots for the 2-3 instrument pair in deployment 2 show consistency between the measurement and simulation. (a) Squared modulus of the analytic signal of measured correlation functions throughout the duration of 34 days, with each horizontal stipe of the figure corresponding to a 800-file-stacked correlation function. White dotted lines correspond to ray arrivals from simulation. (b) The modulus of the analytic signal of simulated correlation function using the KRAKEN normal mode model.

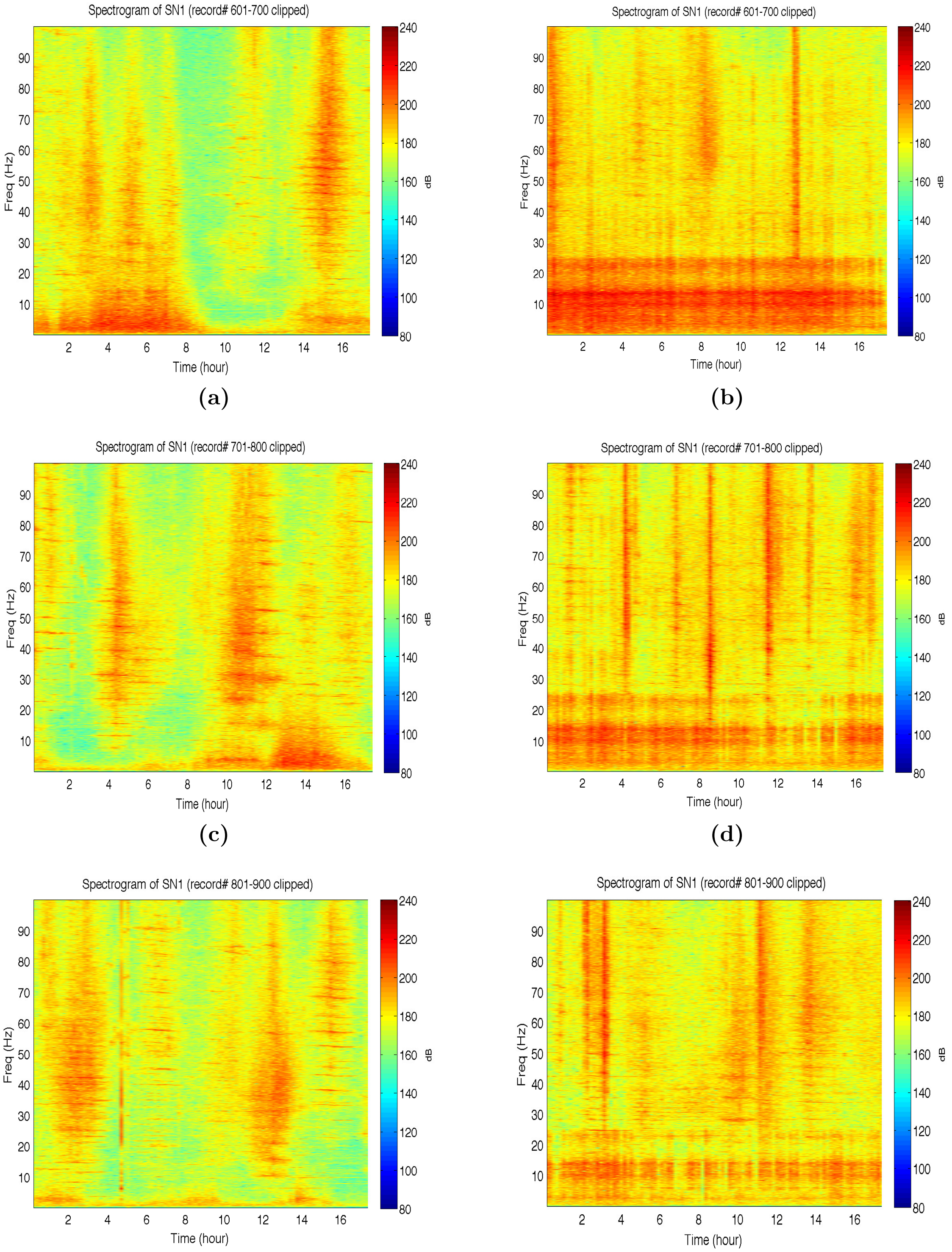

(a) (b) (c) (d) (e) (f)

Figure 2.6: Spectrograms of noise data recorded by instrument 1 in deployment 1 (left panels) and deployment 2 (right panels). The features in spectrograms illustrate the difference of noise source compositions in two deployments.

Chapter 3

Waveform Modeling and Inversion of Ambient Noise Cross-correlation Functions in a Coastal Ocean Environment

3.1 Motivation

The process by which approximations to Green's functions (GFs) between two locations are estimated by cross-correlating time series of ambient noise recorded at those two locations is widely referred to as noise interferometry (NI). The underlying theory is now well developed.(2; 4; 9; 10; 11; 12; 14; 18; 20; 21; 22; 23; 24) NI has proven to be extremely useful in remote sensing applications, including seismic applications,(25; 26; 28; 32) helioseismic applications,(34; 36) atmospheric acoustic applications,(37; 38; 39) structural health monitoring,(40; 41) and ocean infragravity wave studies(43). The utility of NI in underwater acoustic applications,(44; 47; 48; 49; 50; 51; 53; 54; 55) including passive echosounder applications,(56; 58; 61) has also been demonstrated. In underwater acoustic applications of NI, most investigators have focused on extracting estimates of the travel times of temporally resolved multi-paths from the measured noise cross-correlation function (NCF). But in situations in which multi-paths are not temporally resolved, the extraction of information from a measured NCF suitable for use in an inverse analysis requires that one carefully considers and accounts for subtle differences between NCFs and GFs. That is the case in the data that is analyzed here. Also, it should be noted that, even when multi-path arrivals are temporally resolved in measured NCFs, the accuracy of travel time estimates can be significantly improved if NCF waveform (phase) information is exploited.(62) Thus, from a remote sensing perspective, there is strong motivation to carefully examine the relationship between NCFs and GFs. Using data collected in the Straits of Florida, that relationship is explored here. Both the forward problem of simulating NCFs, and the inverse problem of finding the environmental model that gives the best-fitting NCF are considered here.

3.2 NCF waveform modeling: the forward problem

The basic mathematical result underlying acoustic NI is that the cross-correlation function, $C_{AB}(t)$, of time series of acoustic pressure ambient noise at locations $\mathbf{x}_A$ and $\mathbf{x}_B$ satisfies

$$\frac{d}{dt}C_{AB}(t) = D(t) * [G(\mathbf{x}_B|\mathbf{x}_A, -t) - G(\mathbf{x}_A|\mathbf{x}_B, t)], \tag{3.1}$$

where $D(t)$ is an approximation to a delta function, $*$ denotes convolution, and the transient Green's function satisfies $G(\mathbf{x}|\mathbf{x}_0, t)$ satisfies

$$\left(\nabla^2 - \frac{1}{c^2(\mathbf{x})}\frac{\partial^2}{\partial t^2}\right) G(\mathbf{x}|\mathbf{x}_0, t) = -\frac{\delta(r)}{2\pi r}\delta(z - z_0)\delta(t), \tag{3.2}$$

where $\mathbf{x} = (x, y, z)$, $\mathbf{x}_0 = (0, 0, z_0)$ and $r = (x^2 + y^2)^{1/2}$. The GFs are causal; the positive (negative) lag portion of $C_{AB}(t)$ describes propagation from $\mathbf{x}_B$ to $\mathbf{x}_A$ ($\mathbf{x}_A$ to

$\mathbf{x}_B$). Consistent with Eq. (3.2), we assume here that the environment is stationary, so $G(\mathbf{x}_B|\mathbf{x}_A, t) = G(\mathbf{x}_A|\mathbf{x}_B, t)$ by reciprocity. With this assumption, it follows from Eq. (3.1) that the negative lag structure of $C_{AB}(t)$ is redundant and that for $t > 0$

$$\frac{d}{dt}C_{AB}(t) = -D(t) * G(\mathbf{x}_A|\mathbf{x}_B, t). \tag{3.3}$$

The normal mode representation of $\bar{G}(\mathbf{x}_A|\mathbf{x}_B, \omega)$, the Fourier transform of $G(\mathbf{x}_A|\mathbf{x}_B, t)$, is well known.(66) (Note that unlike Eq. (3.3), the normal mode representation assumes a layered medium.) Consistent with Eq. (3.3), the normal mode representation of $\bar{C}_{AB}(\omega)$, satisfies $-i\omega\bar{C}_{AB}(\omega) = -\bar{D}(\omega)\bar{G}(\mathbf{x}_A|\mathbf{x}_B, \omega)$, or

$$\bar{C}_{AB}(\omega) = \bar{D}(\omega)\left(\frac{1}{i\omega}\right)\left(\frac{i}{4}\right)\sum_m \psi_m(z_A)\psi_m(z_B)H_0^{(1)}(k_m(\omega)r_{AB}), \tag{3.4}$$

where the normal modes, which are defined on the depth interval $(-\infty, 0]$ are assumed to be normalized, $\int_{-\infty}^{0} \psi_m^2(z)\, dz = 1$, and r_{AB} is the horizontal separation between $\mathbf{x}_A$ and $\mathbf{x}_B$.

A straightforward derivation of Eq. (3.1) (see Section 1.2.2) involves making use of an exact identity involving GFs , Eq. (1.18), together with the highly idealized assumption, Eq. (1.9), that noise sources are delta-correlated in space and time. The latter assumption is clearly an approximation. In spite of this, Eq. (3.1), and hence also Eqs. (3.3) and (3.4) remain useful approximate results provided the distribution of noise sources is approximately diffuse. To account for physical processes that are not accounted for in the derivation of Eq. (3.1), including a diffuse but nonuniform distribution of noise sources, a weighting function(44) can BE included on the rhs of Eq. (3.4).

The weighting function used here is a product of two terms. The first accounts for the fact that in the frequency band used here to construct NCFs, 20-70 Hz, noise sources, including shipping and wind-related noise, are predominantly near-surface sources.(65) (Seismic sources also contribute to ambient noise in this frequency band, but there was no known nearby exploration geophysics activity during our experiment, or experimental evidence of its presence.) The pressure-release boundary condition at the air-sea interface then leads to a dipole radiation pattern, with $\sin\theta$ weighting, where θ is the propagation angle at the sea surface measured relative to the horizontal. The relevance of the dipole excitation weighting in underwater acoustic NI applications was first pointed out by Roux *et al.*(44).

The second term in the weighting function that we employ accounts for the fact that tidal fluctuations lead to phase fluctuations – and thus coherence loss – of surface reflecting energy, which is partially filtered out by the phase-coherent processing that we perform. Note in this regard that the NCFs analyzed here were produced by coherently stacking short-time NCF estimates over a duration (approximately six days) that is long compared to the M2 tidal period, and that energy at higher frequency and steeper propagation angles is most susceptible to tidal-fluctuation-induced coherence loss. To quantify the effect of tidal fluctuations, consider a homogeneous ocean with sound speed c and constant depth h, subject to a tidal perturbation δh. Let r_{hc} denote the range of a half ray cycle of a surface- and bottom-reflecting ray connecting fixed instruments. At range r the number of half ray cycles is $r/r_{hc} = r\tan\theta/h$. For each half ray cycle the path length perturbation is $\delta h\sin\theta$. The total tidal-induced path length perturbation over range r is then $(r\delta h/h)\sin\theta\tan\theta$ and the total phase perturbation is $\Delta\phi(\omega,\theta) = (\omega/c)(r\delta h/h)\sin\theta\tan\theta$. It is shown in section 9.8 of Brekhovskikh and Lysanov (67) that if phase fluctuations have a Gaussian pdf, the mean coherent field is weighted by the function $\exp(-(\Delta\phi)^2/2)$ where $\Delta\phi$ is evaluated with δh set equal to its rms value. In our simulations this expression for the tidal-fluctuation-induced coherence loss weighting function was used with δh set equal to

0.45 m, consistent with relevant environmental conditions.

With the above comments in mind, our simulated NCFs are computed by evaluating a weighted form of Eq. (3.4),

$$\bar{C}_{AB}(\omega) = \bar{D}(\omega)\left(\frac{1}{4\omega}\right)\sum_{m} W(\omega,\theta_m)\psi_m(z_A)\psi_m(z_B)H_0^{(1)}(k_m(\omega)r_{AB}) \qquad (3.5)$$

where $W(\omega, \theta_m) = \sin\theta_m \exp(-(\Delta\phi(\omega, \theta_m))^2/2)$. Note that θ_m depends on both mode number and frequency, consistent with the modal quantization condition, and the relationship $k_m = (\omega/c)\cos\theta_m$. Consistent with the manner in which measured NCFs were processed, $\bar{D}(\omega)$ was chosen to be a Hanning window with zeros at 20 and 70 Hz. Fourier transforming $\bar{C}_{AB}(\omega)$ back to the time domain gives $C_{AB}(t)$. All calculations shown below were performed using a slightly modified form of the KRAKEN(68) normal mode model.

3.3 NCF waveform modeling: the inverse problem

3.3.1 Inversion method

The results presented in the previous section rely on approximate and possibly incomplete descriptions of relevant physical processes. The validity of our mathematical description of these processes needs to be demonstrated by showing equivalence between measured and simulated NCFs. But such a comparison is complicated by environmental uncertainty. In this section we describe a simple procedure to test our ability to reproduce, using Eq. (3.5), measured NCF waveforms, while simultaneously allowing for plausible environmental uncertainty. The ocean sound speed structure and bathymetry were well characterized during the experiment. There is much greater uncertainty in the seafloor structure, and, in the 20-70 Hz band of interest, the influence of the seafloor structure on the water column sound field is expected to be significant. Thus our inverse analysis focuses on seafloor structure together with uncertainty (of O(10 m)) in the horizontal separation r between instruments.

With these comments in mind, our inverse analysis focuses on r and parameters that describe the seafloor structure, using some assumed parameterization. We focus on NCFs estimated using the 1-2 instrument pair, corresponding to r of approximately 5.01 km. We focus on the 1-2 instrument pair for two reasons: 1) the SNR for the 1-2 instrument pair is higher than that for the 2-3 instrument pair; and 2) the assumption of range-independent bathymetry is a much better approximation for the 1-2 pair than for the 2-3 pair. Note that the mathematical expression for the weighting function that was introduced above was greatly simplified by the assumption that the environment is range-independent.

The following simple procedure is used to investigate the inverse problem. A parameterization of the environment is chosen, together with suitable bounds on the model parameters. A brute-force search over the relevant parameter space is then conducted. For each combination of model parameters, a suitable measure of misfit between simulated and measured NCFs is computed. The optimal set of model parameters is then chosen to be the set that minimizes the misfit. For the results shown, the misfit was defined as

$$M(\mathbf{p}) = \int_{t_{start}}^{t_{end}} \left[C_m(t) - C_s(\mathbf{p},t)\right]^2 \; dt \tag{3.6}$$

where the elements of the vector $\mathbf{p}$ are the model parameters, $C_m(t)$ is the measured NCF, and $C_s(\mathbf{p},t)$ is the simulated NCF. Because there is no absolute amplitude scale for $C_m(t)$, both $C_m(t)$ and $C_s(\mathbf{p},t)$ in Eq. (3.6) are normalized so that their maximum absolute amplitudes are equal to 1. For the 1-2 pair t_{start} and t_{end} were set equal to

3.2 s and 3.7 s, respectively. The procedure just described can be claimed to lead to an optimal solution for the range of parameter values explored, but it is important to keep in mind that inversion results depend on how one chooses to parameterize the environment. For that reason, no claim to uniqueness can be made. Several different environmental parameterizations have been explored. Three of these are discussed below. With guidance from a nearby seismic section (71) in a similar geological setting, both parameterizations considered here assume that the seafloor is a two-layer structure consisting of a sediment layer overlying a substrate. Parameter limits were chosen, in part, using guidance from Jensen *et al.*,(72) and, in part, to insure that the minimum of the misfit function could fall on a parameter limit only if a physical argument prevented that limit from being exceeded.

3.3.2 Inversion results

Firstly, we consider an environmental model consisting of a half-space fluid bottom. We refer to this model as the three-parameter model. The three parameters that we will estimate are the sound speed in the bottom c_b, the bottom density ρ_b, and the range r. A comparison of the measured NCF and the best-fitting three-parameter simulated NCF is shown in Fig. 3.1. Figure 3.2 shows the corresponding misfit function.

Secondly, we consider an environmental model consisting of a fluid sediment layer overlying a rigid bottom. We shall refer to this as the four parameter model. The four parameters that we seek to estimate are the sediment sound speed c_s, the sediment density ρ_s, the sediment layer thickness d_s, and the range r. A comparison of the measured NCF and the best-fitting four-parameter simulated NCF is shown in Fig. 3.3. Figure 3.4 shows two two-dimensional slices of the corresponding misfit

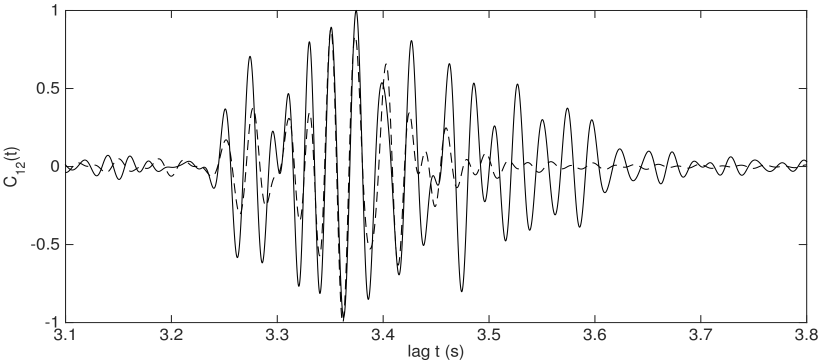

Figure 3.1: Measured NCF (solid curve) and best-fitting three-parameter simulated NCF (dashed curve) for the 1-2 instrument pair.

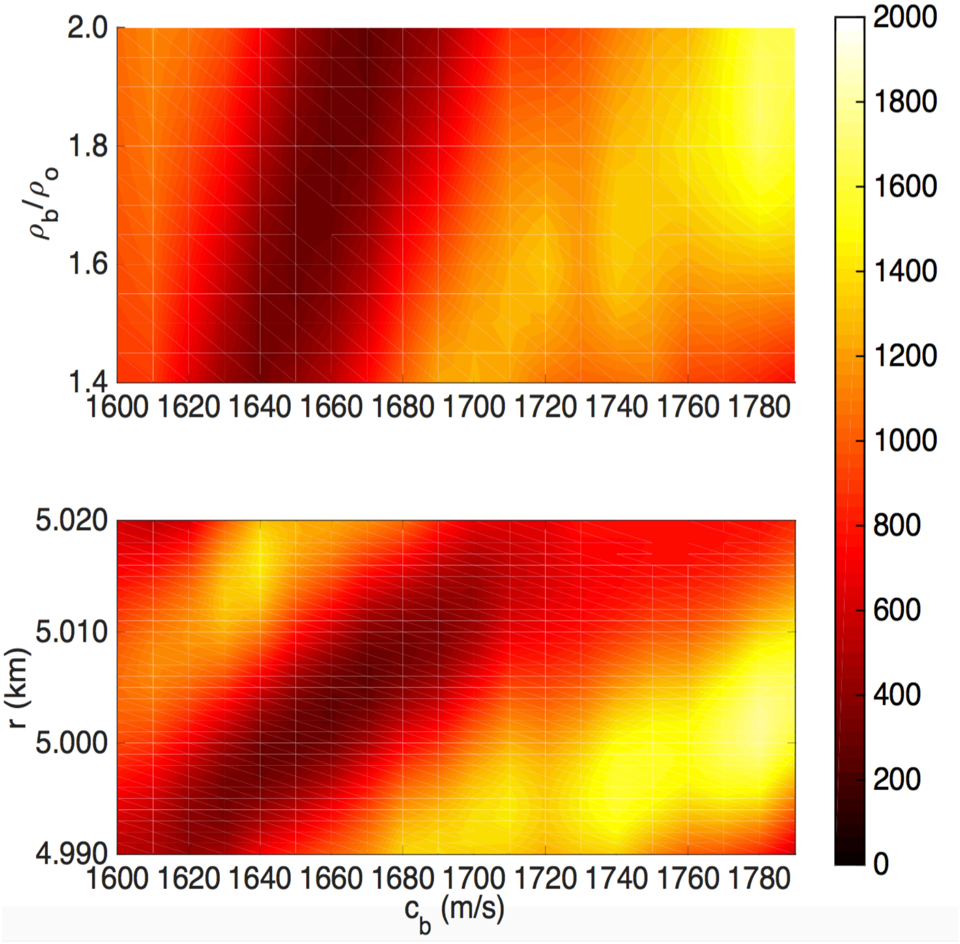

Figure 3.2: Two two-dimensional slices of the three-parameter misfit function for the 1-2 instrument pair: $M(\rho_b/\rho_{ocean}, c_b)$ for $r = 5.006$ km; and $M(r, c_b)$ for $\rho_b/\rho_{ocean} = 2.0$.

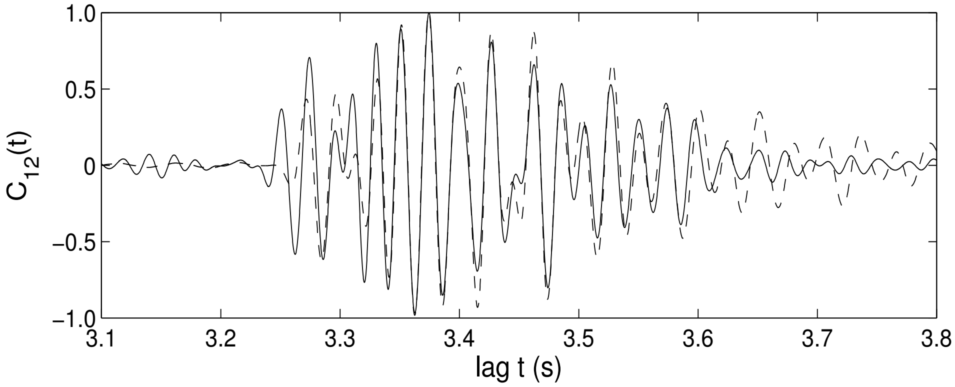

Figure 3.3: Measured NCF (solid curve) and best-fitting four-parameter simulated NCF (dashed curve) for the 1-2 instrument pair.

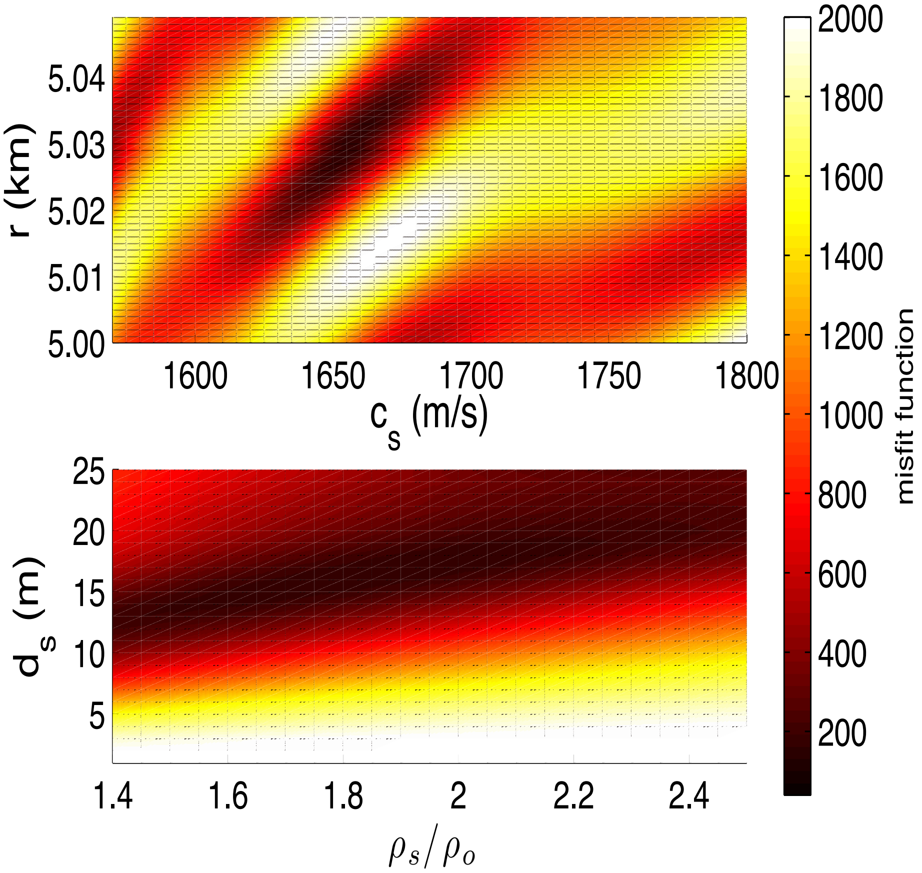

Figure 3.4: Two two-dimensional slices of the four-parameter misfit function for the 1-2 instrument pair: $M(c_s, d_s)$ for $\rho_s/\rho_{ocean} = 1.90$, $r = 5.030$ km; and $M(\rho_s/\rho_{ocean}, r)$ for $c_s = 1655$ m/s, $d_s = 17$ m.

function $M(c_s, d_s)$ for fixed ρ_s, r; and $M(\rho_s, r)$ for fixed c_s, d_s. Figure 3.4 also shows limits on the search domain of the four unknown parameters. Not surprisingly, the misfit M is less sensitive to ρ_s than the other three parameters. Minimizing the misfit function that we have chosen, Eq. (3.6), imposes a high penalty for a phase mismatch, so it is not surprising that the phases of measured and simulated NCFs in Fig. 3.3 are in generally better agreement than the amplitudes.

Thirdly, we consider a slightly more general lossy fluid model with eight unknown parameters: the sediment layer sound speed c_s, the sediment layer thickness d_s, the sediment layer density ρ_s, the sediment layer attenuation α_s, the substrate (bottom) sound speed c_b, the substrate density ρ_b, the substrate attenuation α_b, and the range r. A comparison of the measured NCF and the best-fitting eight-parameter simulated NCF is shown in Fig. 3.5. Figure 3.6 shows two two-dimensional slices of the corresponding misfit function: $M(c_b, r)$ for fixed c_s, d_s, ρ_s, α_s, ρ_b and α_b; and $M(d_s, c_s)$ for fixed ρ_s, α_s, c_b, ρ_b, α_b and r. Figure 6 also shows the limits of the search domain for the unknown parameters r, c_s, d_s and c_b. The other four parameter searches were bounded by the limits $1.2 < \rho_s/\rho_{ocean} < 1.7$, $1.7 < \rho_b/\rho_{ocean} < 3.0$, $0 < \alpha_s < 1.0$ dB/λ and $0 < \alpha_b < 1.2$ dB/λ.

A complete summary of the inversion results obtained with three models are

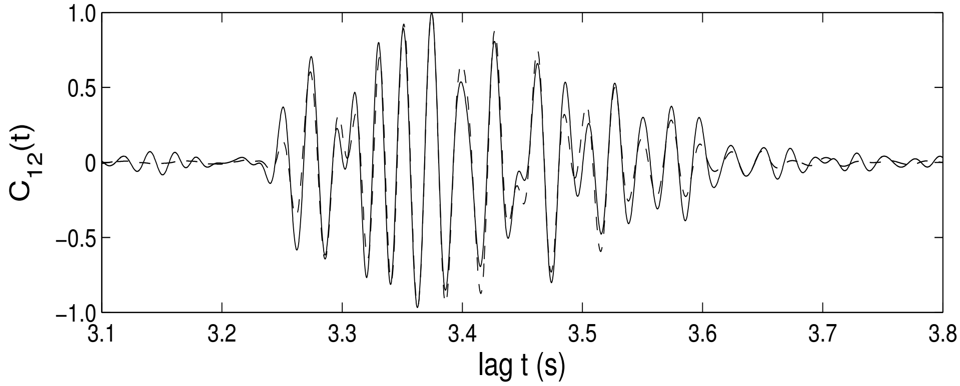

Figure 3.5: Measured 1-2 instrument pair NCF (solid curve) and corresponding simulated NCF (dashed curve) computed using the optimal eight-parameter environmental model with $W = \sin\theta \exp(-(\Delta\phi)^2/2)$.

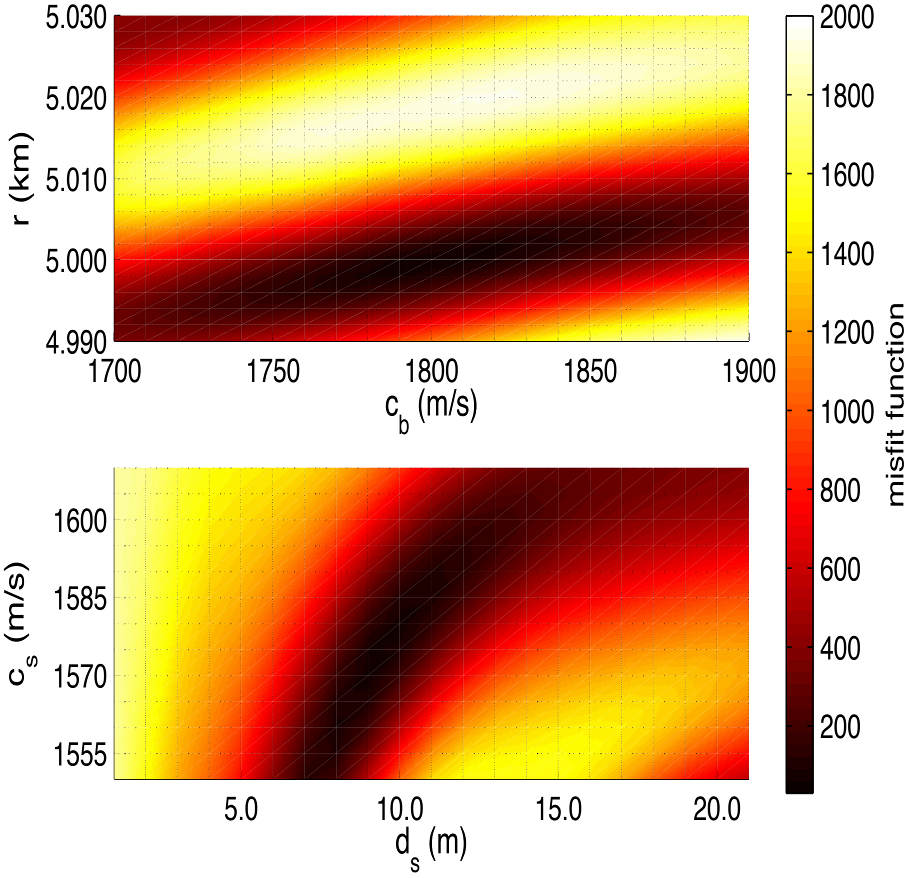

Figure 3.6: Two two-dimensional slices of the eight-parameter misfit function for the 1-2 instrument pair: $M(c_b, r)$ for $c_s = 1570$ m/s, $d_s = 9$ m, $\rho_s/\rho_{ocean} = 1.3$, $\alpha_s = 0$, $\rho_b/\rho_{ocean} = 2.2$, $\alpha_b = 0.8$ dB/λ; and$M(d_s, c_s)$ for $r = 5.000$ km, $\rho_s/\rho_{ocean} = 1.3$, $\alpha_s = 0$, $c_b = 1800$ m/s, $\rho_b/\rho_{ocean} = 2.2$, $\alpha_b = 0.9$ dB/λ.

listed in Table 3.1.

3.4 Discussion

The results presented in the previous section are representative of a much larger set of qualitatively similar results. Other environmental model parameterizations have been explored, as have other choices of the misfit function. As noted above, the type of analysis performed allows one to make only very qualified statements about opti-

Number of Parameters	Optimal Parameters	Misfit Function	Correlation Coefficient
Three	$r = 5.006$ km, $c_b = 1670$ m/s, $\rho_b = 2.0$	236.2596	75.17%
Four	$r = 5.030$ km, $H = 17$ m, $c_s = 1655$ m/s, $\rho_s = 1.90$	113.9025	89.67%
Eight	$r = 5.000$ km, $H = 9$ m, $c_s = 1570$ m/s, $\rho_s = 1.30$, $\alpha_{ps} = 0.0$ dB/λ, $c_b = 1800$ m/s, $\rho_b = 2.2$, $\alpha_{pb} = 0.8$ dB/λ	38.5843	96.33%

Table 3.1: Summary of the geoacoustic inversion results

mality and uniqueness of the solution found; these issues are related to each other, and are strongly tied to, and constrained by, the assumptions that one makes about how to parameterize the environment. Some specific comments about the results presented above follow.

3.4.1 Comparison of inversion results using three geoacoustic models

From Figure 3.2, the duration of simulated NCF is much shorter than the measured NCF, which means that the simplest three-parameter model in our study is incapable of approximating the real ocean environment. Thus, except for the basic use as a reference, it should not be taken for further consideration.

Although the four-parameter model corresponding to the NCF shown in Fig. 3.3 is optimal in the sense that we have described, that solution appears to have a significant defect: the leading edge of the energetic portion of the simulated NCF appears to be one cycle out of phase with the measured NCF. Consistent with this observation, the estimated value of r, 5.030 km, is a larger correction, 20 m, to the navigational estimate than we expect. Convergence to a poor solution is due to a combination of the choice of the misfit function (recall the comments above about the misfit function imposing a high penalty on relative phase mismatch) and an overly restrictive parameterization of the environment. As a result, we have little confidence in the estimated four-parameter model solution. That model will not be further discussed.

In contrast, there is no obvious problem associated with the solution found using the eight-parameter model (see Fig. 3.5). The optimal parameters found using the eight-parameter model are $r = 5.000$ km, $c_s = 1570$ m/s, $d_s = 9.0$ m, $\rho_s/\rho_{ocean} = 1.30$, $\alpha_s = 0$, $c_b = 1800$ m/s, $\rho_b/\rho_{ocean} = 2.20$ and $\alpha_b = 0.8$ dB/λ. We have estimated domains of uncertainty for each of these parameters by varying each parameter independently, keeping the others fixed at their optimal values. Lower and upper bounds on the uncertainty domain for the varied parameter were then estimated as the nearest parameter values for which the misfit M is higher than the absolute minimum, M_{min}, of the misfit function by an amount equal to 1% of the total range of M over the entire search domain. (Although the choice of the threshold value of M is somewhat arbitrary, this exercise gives a good idea of the range of parameters for which agreement between measured and simulated NCFs is very good.) The procedure just described gives the following bounds: 4.999 km $< r <$ 5.001 km; 1567 m/s $< c_s <$ 1575 m/s; 8.8 m $< d_s <$ 9.2 m; $1.24 < \rho_s/\rho_{ocean} < 1.36$; 0 dB/$\lambda$ $< \alpha_s <$ 0.42 dB/λ; 1789 m/s $< c_b <$ 1814 m/s; $2.09 < \rho_b/\rho_{ocean} < 2.27$; and 0.2 dB/$\lambda$ $< \alpha_b <$ 2.0 dB/λ. It is clear from these bounds that our inversion results do not provide strong constraints on estimates of α_s and α_b. Consistent with the assumed structure of our eight-parameter model and our sediment layer thickness estimate, a seismic section at a site in a geologically similar setting (about 15 km from the Florida Keys in water of approximately 100 m deep and approximately 100 km to the southwest of our experimental site) reveals a sediment layer, whose thickness is approximately 10 m, overlying a limestone formation.(71) It is difficult to provide a quantitative assessment of any of our other geoacoustic parameter estimates. Jiang *et al.* (73) and Monjo *et al.* (74) also performed geoacoustic inversions using data collected at sites that are approximately 120 and 230 km, respectively, north of our experimental site, but in deeper water where the sediment layer thickness is greater. Those authors and the references they cite (which list non-acoustic measurements of bottom properties in the Florida Straits) report a very broad range of parameter values, including values of parameters that we have not considered like porosity, shear wave speed and attenuation, and compressional speed gradients. Compressional wave speed estimates in the sediment range from 1540 m/s (74) to 1683 m/s (73).

3.4.2 Spectral analysis and narrowband analysis

Some features of the simulated NCF based on the optimal eight-parameter environmental model will now be described. Figure 3.7 shows spectra of measured and simulated NCFs. Agreement is seen to be good. Recall that a Hanning window has been applied to both spectra, so no insight into how well the inversion procedure worked can be gleaned by comparing spectral envelopes. In contrast, the locations of the zeros in the spectrum of the simulated NCF have not been constrained in any way, so the good agreement between the locations of the zeros in the spectra of the simulated and measured NCFs gives one confidence that the estimated environmental model is close to the true environment. Figure 3.8 shows measured and simulated NCFs in overlapping narrow (10 Hz) frequency bands. Within each 10 Hz band a Hanning window weighting function was applied, and each band-limited NCF was normalized individually. Agreement between measured and simulated NCFs is seen to be good in all frequency bands shown.

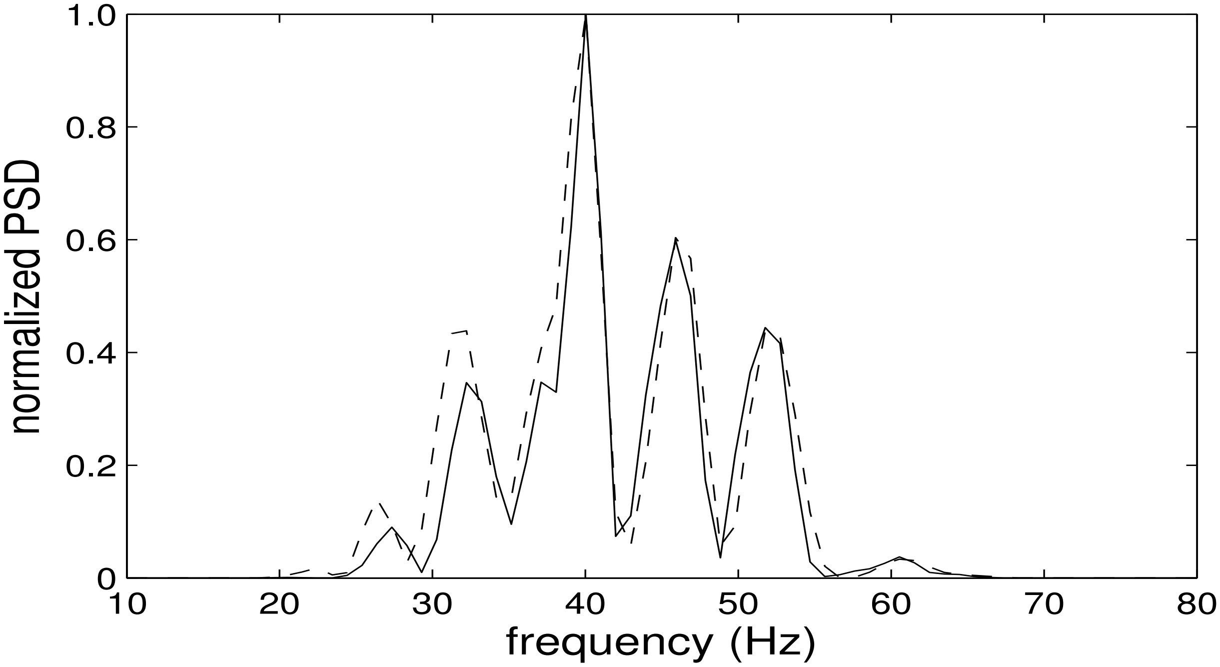

Figure 3.7: Spectra of measured NCF (solid curve) and best-fitting eight-parameter simulated NCF (dashed curve) for the 1-2 instrument pair.

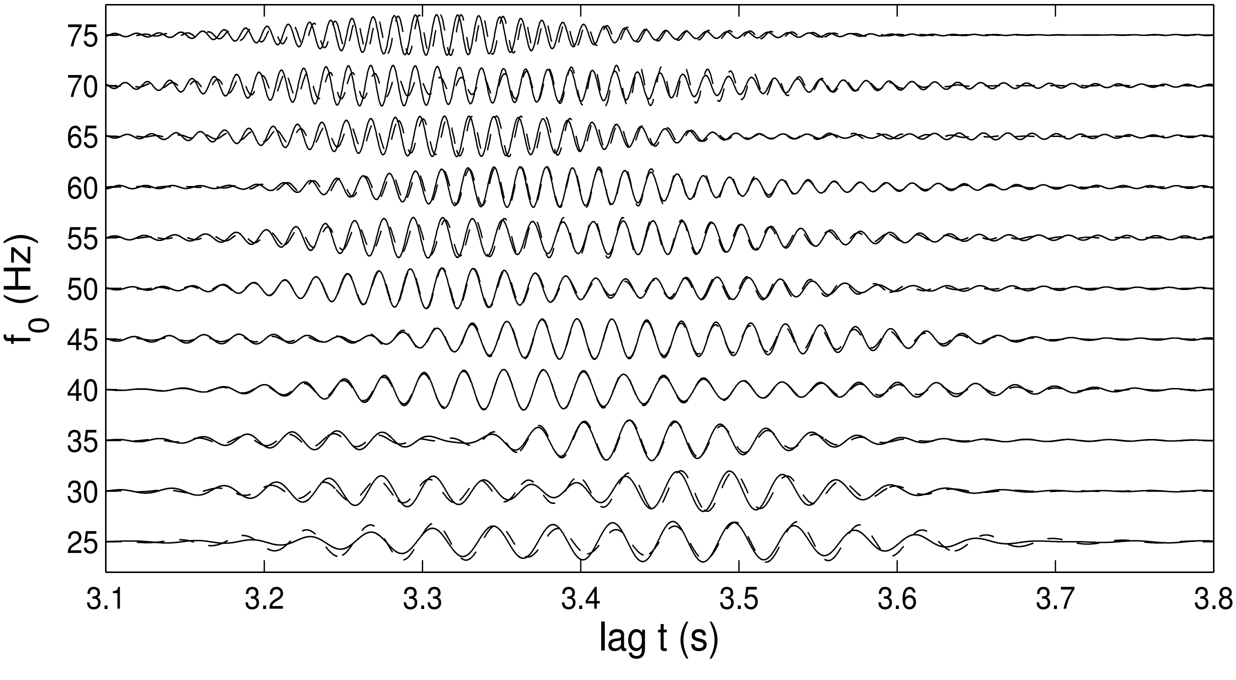

Figure 3.8: Measured NCF (solid curves) and best-fitting eight-parameter simulated NCF (dashed curves) for the 1-2 instrument pair in overlapping 10 Hz bands.

3.4.3 Waveform modeling of NCF of 2-3 instrument pair

We turn our attention now to analysis of the NCF estimated using the 2-3 instrument pair. The estimated navigational separation between those instruments is 9.76 km. The low SNR of the NCF for this instrument pair poses an obvious limitation. Also, along the path between the 2-3 instrument pair the bottom depth varied between 86 and 100 m, compared to variations between 97 and 101 m along the path between the 1-2 instrument pair. To model propagation between the 2-3 instrument pair, the range-independent assumption is not realistic. The combination of low SNR and a range-dependent environment led us to give up on the idea of performing the same type of analysis of this data that was performed using the NCFs estimated using the 1-2 instrument pair. Instead, we use this data set as a consistency test on the model parameters that were estimated using the 1-2 instrument pair inverse analysis described above. A comparison of measured and simulated NCFs for the 2-3 instrument pair is shown in Fig. 3.9. To perform the simulation an adiabatic mode calculation (68; 72) was performed. Such a calculation is expected to be accurate because bathymetric variations were gradual. The adiabatic mode calculation was performed assuming the sediment layer thickness was constant and that all bottom parameters are identical to those described above, based on the 1-2 instrument pair analysis. Note, however, that while the environment is assumed fixed in this calculation, uncertainty in the range between instruments 2 and 3 must be allowed and accounted for. This led to a one-parameter inverse problem that was solved the same way the four- and eight-parameter inverse problems described above were solved. The adiabatic mode calculation shown in Fig. 9 corresponds to the best-fitting value of r. The optimal value of r was found to be 9.775 km, which deviates by 15 m from the nominal navigation-based estimate. Considering the relatively low SNR of the measured NCF, agreement between measured and simulated NCFs in Fig. 3.9 is fairly good. On the time interval from 6.35 s to 7.0 s the correlation coefficient between measured and simulated NCFs is 70.6%.

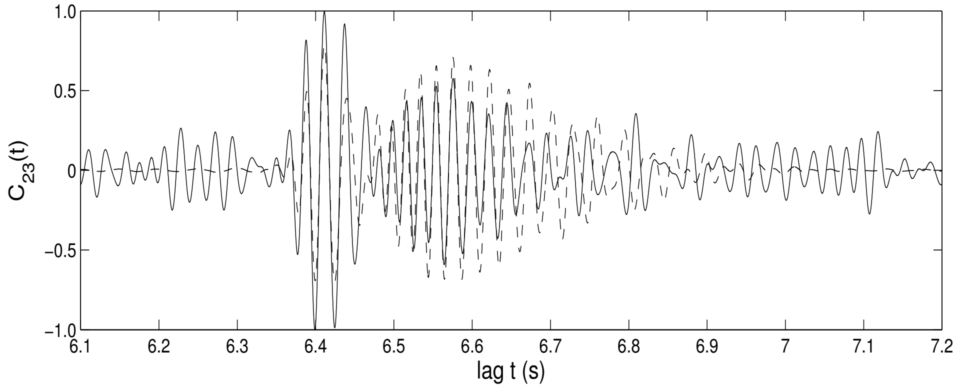

Figure 3.9: Measured NCF (solid curve) and simulated NCF (dashed curve) for the 2-3 instrument pair.

3.4.4 Comments on weighting functions

We now address the question of whether inclusion of the weighting function $W(\omega, \theta_m)$ improves agreement between measured and simulated NCFs. Figure 10 shows a comparison of the measured broadband (20-70 Hz) NCF for the 1-2 instrument pair with an unweighted ($W = 1$) simulation, computed using the optimal parameter values listed above. Recall that Fig. 3.5 shows a comparison of the same measured NCF with a weighted (using $W = \sin\theta \exp(-(\Delta\phi)^2/2)$) simulated NCF. When comparing Figs. 3.5 and 3.10 it is useful to keep in mind that the early arriving energy – prior to about 3.35 s – is low-angle energy that is strongly damped in Fig. 5 by the term $\sin\theta$; later-arriving energy is higher angle energy that is damped by both $\sin\theta$ and $\exp(-(\Delta\phi)^2/2)$, with neither term dominant. Also, all NCFs plotted in both Fig. 3.5 and Fig. 3.10 are normalized to have maximum absolute amplitude equal to 1, which partially obscures the aforementioned damping. (Some normalization assumption must be made because there is no absolute amplitude scale for measured NCFs.) Differences between Fig. 3.5 and Fig. 3.10 are small; with the aforementioned normalization, correlation coefficients between measured and simulated NCFs are 96.3% when $W = \sin\theta \exp(-(\Delta\phi)^2/2)$ (Fig. 3.5) is used and 94.8% when $W = 1$ (Fig. 3.10) is used. The absence of strong sensitivity to W is partly due to the normalization that we have described, and partly due to the fact that replacing $W = \sin\theta \exp(-(\Delta\phi)^2/2)$ by $W = 1$ does not alter the good phase agreement between measured and simulated NCFs. It should also be noted that because both the tidal-fluctuation-induced coherence loss term $\exp(-(\Delta\phi)^2/2)$ and seafloor attenuation serve to preferentially attenuate steep-angle energy at higher frequencies, the optimal choice of the latter is expected to depend on whether or not the former is included in W. Although replacing $W = 1$ by $W = \sin\theta \exp(-(\Delta\phi)^2/2)$ results in only slightly better agreement between simulated and measured NCFs, that replacement represents an important, albeit incomplete, step towards describing the relevant underlying physics that contribute to the measured NCF.

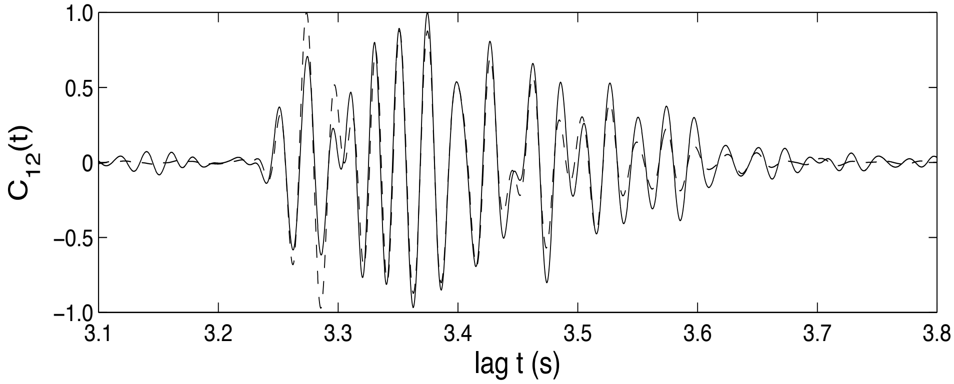

Figure 3.10: Measured 1-2 instrument pair NCF (solid curve) and corresponding simulated NCF (dashed curve) computed using the optimal eight-parameter environmental model with $W = 1$.

3.5 Validation of the optimal geoacoustic model using a time reversal mirror

3.5.1 Motivation

In previous sections, we've successfully performed the waveform modeling of noise correlation functions and obtained an eight-parameter geoacoustic model that fits the real environment very well. In this section, we verify the optimality of the eight-parameter model with a time reversal mirror.

The physics of the time-reversal mirror was firstly presented by Fink in 1997 (75) and demonstrated in the ocean by Kuperman *et al.* (76; 77; 78). Its basic idea is: in a multi-pathing environment, transmit a signal from the source and receive the transmitted signal at the receiver array; then transmit the received signal back to the source location in reverse time; the back propagated signal will refocus at the source location, both temporally and spatially, due to the multi-path propagation. In our noise interferometry experiments, the shallow water environment is an ideal multi-pathing environment, which enables the application of the time reversal mirror. If we back propagate the extracted acoustic Green's function from one location to the other, we can get a focus in the vicinity of the source. The location of the focus relies on the optimality of the geoacoustic model. In this way, we can test the validity of the optimal eight-parameter model we've obtained from waveform modeling and inversion.

3.5.2 Application of time reversal mirror in shallow water environment: simulation

Before we apply time reversal mirror to the measured NCFs, we run a simulation using the RAM PE model. The reason we use the RAM model instead of the KRAKEN model is that RAM can calculate the acoustic field at one calculation with less computation time. We assume an shallow water environment that is the same as the 1-2 instrument pair in noise interferometry experiment, as shown in Fig. 3.11. Using the environment, we firstly calculate the acoustic Green's function $G(\mathbf{x}_B|\mathbf{x}_A, t)$, which is the received signal at location B when the impulsive source is at location A. Then, we propagate the time reversed Green's function $G(\mathbf{x}_B|\mathbf{x}_A, -t)$ from location B to location A. Now the received signal at location A turns out to be a convolution of $G(\mathbf{x}_B|\mathbf{x}_A, -t) * G(\mathbf{x}_A|\mathbf{x}_B, t)$. Due to acoustic reciprocity, $G(\mathbf{x}_B|\mathbf{x}_A, t) = G(\mathbf{x}_A|\mathbf{x}_B, t)$. Thus, the received signal at location is just an autocorrelation function of the acoustic Green's function. Figure 3.12 plots the received signal at the range of hydrophone A at different water depth. It appears that the back propagated signal successfully refocuses at the source in both time and space.

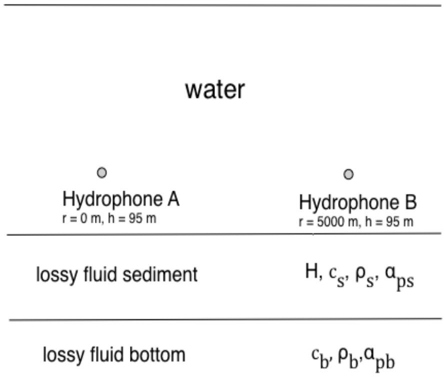

Figure 3.11: Time reversal mirror numerical simulation using the RAM PE model. Parameters H = 9 m, c_s = 1570 m/s, ρ_b = 1.3, α_{ps} = 0, c_b = 1800 m/s, ρ_b = 2.2, α_{pb} = 0.8 dB/λ were obtained from NCF waveform inversion.

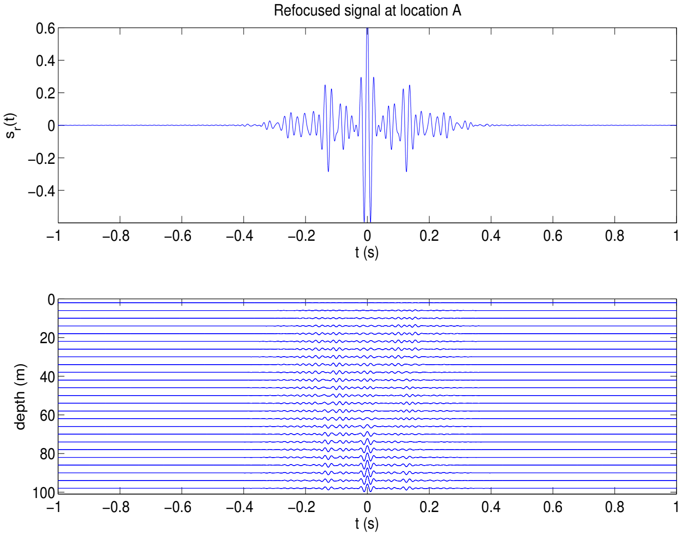

Figure 3.12: The refocused signal at range of hydrophone A in the time reversal mirror simulation using the RAM PE model. Top panel: refocused signal at depth of hydrophone A; bottom panel: a glance of refocused signal at different depth.

To view the spatial focus of the back propagated acoustic field further more, we need a good measure of the focus. After trying different options, we find a measure of acoustic energy level, $E(r,z) = -10 * \log_{10}(1 - 0.99 * (\frac{E(r,z|t_{span})}{E_{ref}}))$. Here, $E(r,z|t_{span})$ is the acoustic energy at location (r,z) within time span t_{span}. We choose t_{span} as (-0.03, 0.03) second, which depicts the main pulse of the refocused signal. $E(r,z)$ is the energy level of the refocused field, which is shown in Fig. 3.13. The back propagated signal is successfully refocused in the vicinity of the source. However, it should be noted that the maximum of $E(r,z)$ doesn't fall on the source location exactly. This is partially due to the fact that the acoustic Green's function at different location has different amplitude, partially due to the measure we choose to visualize the refocused field. With this limitation in mind, we still get a good focus at the source location.

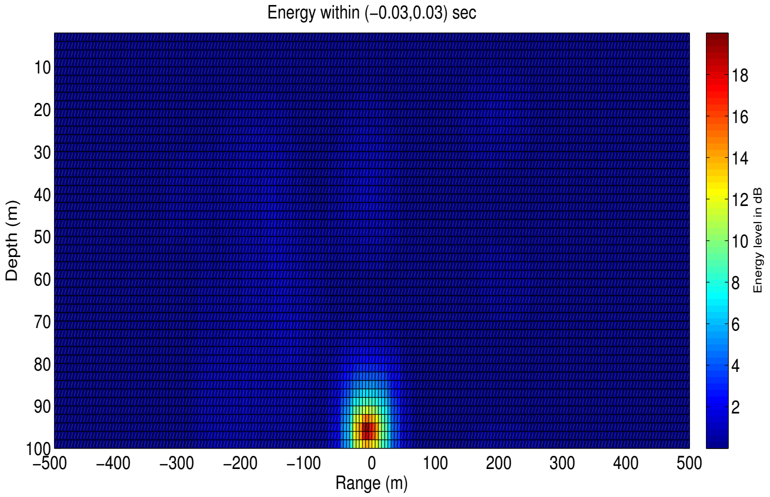

Figure 3.13: The refocused acoustic field in the time reversal mirror simulation using the RAM PE model. The back propagated signal successfully refocuses in the vicinity of the source.

3.5.3 Back propagation of GF using the obtained optimal geoacoustic model

Now we move on to apply the time reversal mirror to the Green's function that were extracted from ambient noise correlation function. The back propagation procedure is similar to the one in Section 3.5.2. The difference is now the Green's function is extracted from measured ambient noise data, not from simulation. Here, in simulating the back propagation, we use the KRAKEN normal model, as it is the model we've used in the waveform inversion. Figure 3.14 shows the refocused acoustic field, using the optimal eight-parameter model. Again, the back propagated GF refocuses at the source location.

Next, we test the sensitivity of the focus to the environmental parameters in the geoacoustic model. Figure 3.15 shows four plots of the test results. In plot (a), the bottom sound speed c_b is changed from 1800 m/s to 1700 m/s. In plot (b), the sound

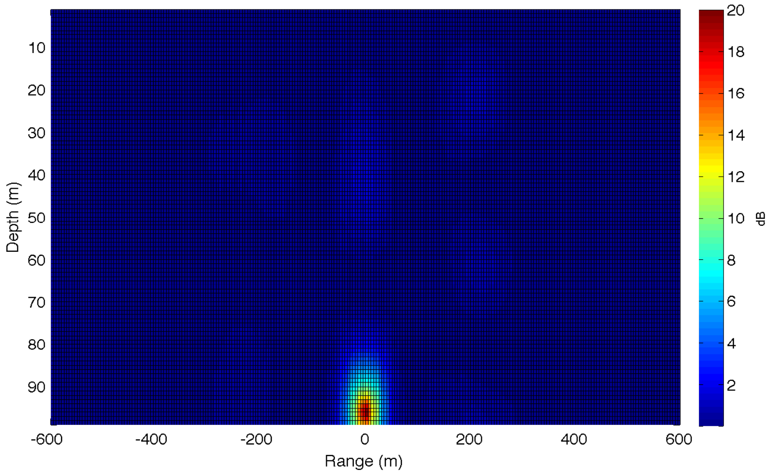

Figure 3.14: The refocused acoustic field after back propagating the Green's function that was extracted from the ambient noise correlation function. The back propagated signal successfully refocuses in the vicinity of the source.

speed in the sediment c_s is changed from 1570 m/s to 1670 m/s. In plot (c), the thickness of the sediment layer is raised from 9 m to 19 m. In plot (d), the range between two locations is shifted from 5000 m to 5025 m. In all four plots, when environmental parameters are different from corresponding optimal parameters, the focus location changes correspondingly. With the sensitivity test, we illustrate both the time-reversal mirror concept and the near optimality of the eight-parameter model obtained from the waveform inversion.

3.6 Summary

We have addressed the problem of waveform modeling of ambient noise cross-correlation functions (NCFs) using measurements collected in a 100 m deep coastal ocean environment at both 5 and 10 km range. NCFs are closely related, but not identical, to the Green's functions (GFs) that describe propagation between the two measurement locations. To model NCF waveforms, subtle differences between NCFs and GFs must

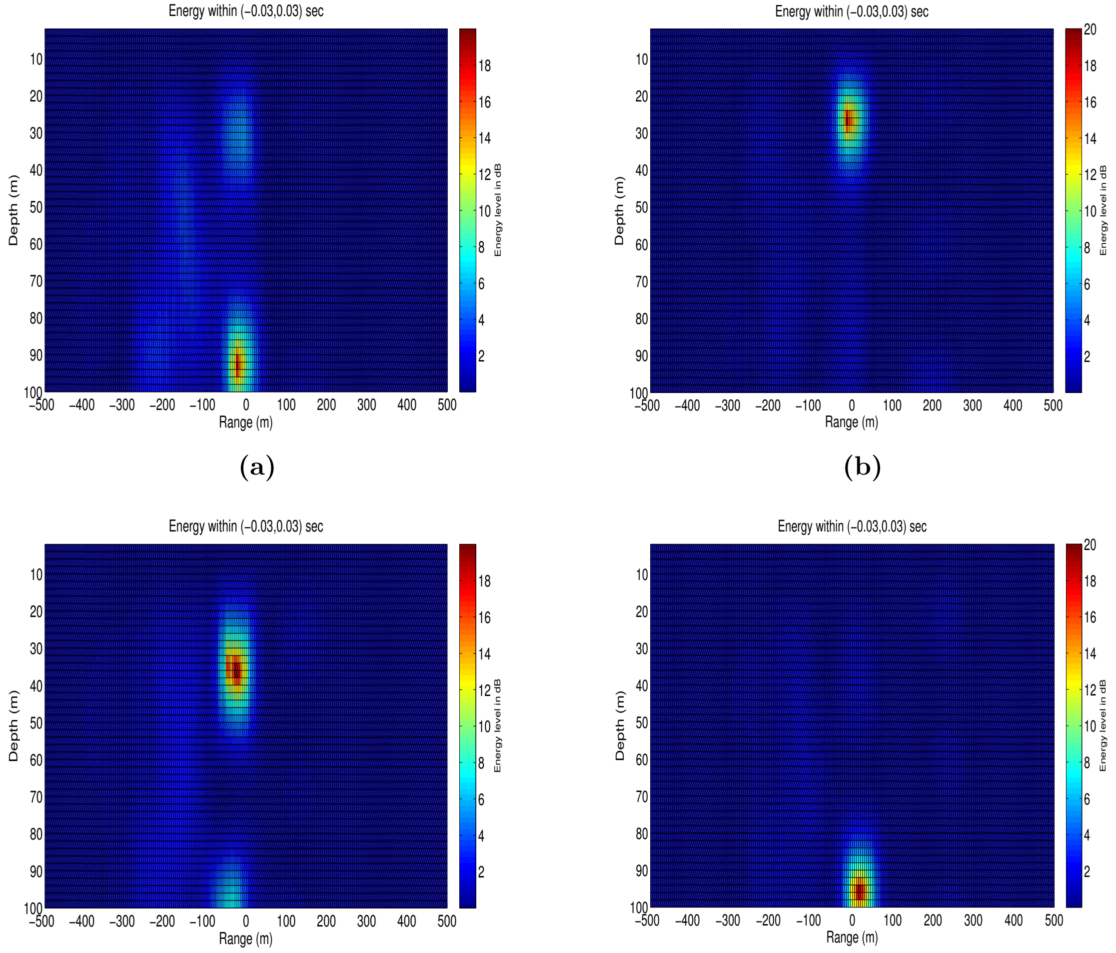

(a) (b)

(c) (d)

Figure 3.15: Sensitivity test of the focus location on the environmental parameters. When the parameters are different from the optimal ones, the focus of back propagated acoustic field shifts from the source location.

be accounted for. We have accounted for a phase difference that is predicted theoretically, and we have introduced a physically motivated amplitude weighting function in our simulated NCFs. The latter accounts for the directivity of the predominantly near-surface noise sources, and the effective filtering outof high frequency and steep angle energy that results from coherently stacking many realizations of short-time estimates of the NCF.

Measured NCFs are also sensitive to the environment, so our focus on modeling NCF waveforms has led us to simultaneously consider the inverse problem of estimating an optimal set of environmental parameters. This was accomplished using a simple parameterization of the environment, together with a brute-force search over a suitably bounded parameter space to identify the set of model parameters that minimize the chosen measure of misfit between measured and simulated NCFs. That effort focused on analysis of NCFs corresponding to an instrument separation of 5 km, both because those NCFs have relatively high SNR and because the 5 km range environment is to a good approximation range-independent. The NCF corresponding to an instrument separation of 10 km was used as a consistency test of the environmental model parameters found using the 5 km data. The 10 km separation data was modeled using an adiabatic normal mode calculation, which showed fairly good agreement between measured and simulated NCFs.

Our focus on modeling NCF waveforms has led us to consider small but important differences between NCFs and GFs, and to investigate the inverse problem. These issues are related inasmuch as one cannot expect to find good agreement between measured and simulated NCFs unless the environmental model used to produce the simulated NCF is close to the true environment. Waveform matching of the type we have performed generally does not lead to a solution to the inverse problem that can be proved to be unique, even when active source transmissions are utilized. This problem is somewhat exacerbated in NI applications. That is because the optimal set of model parameters that one finds will, in general, depend on the weighting function $W(\omega, \theta)$ that is used to compute simulated NCFs. A poor choice of $W(\omega, \theta)$ will lead to a biased set environmental model parameters. The form of $W(\omega, \theta)$ that we have chosen is a good approximation in the environment considered, but has clear limitations. The surface dipole excitation term $\sin\theta$ that we have used does not account for subsurface sound sources or scattering processes that lead to the conversion of steep angle anergy to shallow angle energy. The gaussian coherence loss term that we have used accounts only for tidal-fluctuation-induced coherence loss, and makes the idealized assumption that tidally-induced sea surface height fluctuations have a gaussian distribution. No other coherence loss mechanism was accounted for in our simulated NCFs. In measured NCFs there is no simple way to distinguish between coherence loss mechanisms and attenuation mechanisms.

With the aforementioned limitations and caveats, we have computed simulated NCFs that account for the theoretically predicted phase difference between NCFs and GFs, and that include a physically motivated weighting function $W(\omega, \theta)$ that is a good approximation in the environment considered. Simulated NCFs were used as the basis for a simple treatment of the inverse problem that resulted in an environmental model for which simulated NCFs were shown to be in good agreement with their measured counterparts for instrument separations of both 5 and 10 km.

Using the time reversal mirror, we also illustrates the near optimality of the obtained environmental model. By back propagating the GF that was extracted from NCF, we obtained a focus in the vicinity of the virtual source location. From the sensitivity test, we found that the focus location is sensitive to the environment parameters, which verifies the environmental model once more. Last but not least, the validation test also demonstrates the applicability of time reversal mirrors to passive acoustic remote sensing. More valuably, our time reversal mirror only consists one hydrophone, which reduces the cost and complexity of conventional time reversal applications.

Chapter 4

Time Warping Processing and Current Speed Estimation

4.1 Background

As discussed in Chapter 2, from the extracted noise cross-correlation function (NCF) at 5 km, 10 km and 15 km range (deployment 1), the signal to noise ratio (SNR) of NCF decreases as the separation increases (Fig. 4.1). Note again that the SNR of the stacked NCF refers to the energy ratio of the coherent signal to the non-coherent signal. The coherent signals that correspond to the arrival of GFs are viewed as "signal", while the incoherent signals that arrive before and after the GF structures are taken as "noise". In Chapter 3, the waveform modeling and inversion was done using the 1-2 instrument pair only, and the 2-3 instrument pair was used as a consistency check. However, the 1-3 instrument pair is never used due to the low SNR. To extend the separation limit of the noise interferometry application, in this chapter, we explore a method to improve the SNR of measured NCFs; especially, we intend to make use of 1-3 instrument pair after improving its SNR.

Before we start to improve the SNR, we carefully consider the effect of clock drift, which is crucial in the calculation of NCFs, as discussed in Chapter 2. In Fig. 4.1, the clock drifts have been corrected and removed already. The method we use is a broad search in a bounded domain with a resolution of 0.1 ms/day. The search domain of $\triangle_{12}$ and $\triangle_{23}$ is (0.5, 1.5) ms/day and (-0.9, -0.1) ms/day, with reference to to the study in Godin *et al.*, 2014 (64). The measure adopted here to determine the best clock drift is the SNR of the stacked NCFs. We assume that the relative clock drift between two systems is linear in time, i.e. the clock drift rate is constant. Then, in each calculation of NCF, the relative clock drift is corrected and the NCFs are coherently stacked for up to five days. The SNR of the stacked NCF is correspondingly a function of clock drift, which has the maximum at the best clock drift. The broad search results show that the best clock drift between instruments 1-2 is 1.1 ms/day, while the best clock drift between 2-3 is -0.5 ms/day. Since the clock drift between instruments 1-3 is dependent on $\triangle_{12}$ and $\triangle_{23}$, and considering that the SNR in $C_{13}(t)$ is lower than $C_{12}(t)$ and $C_{23}(t)$, we use $\triangle_{13} = \triangle_{12} + \triangle_{23} = 0.6$ m/s in calculating $C_{13}(t)$.

In this chapter, we employ a method called time warping processing–which can

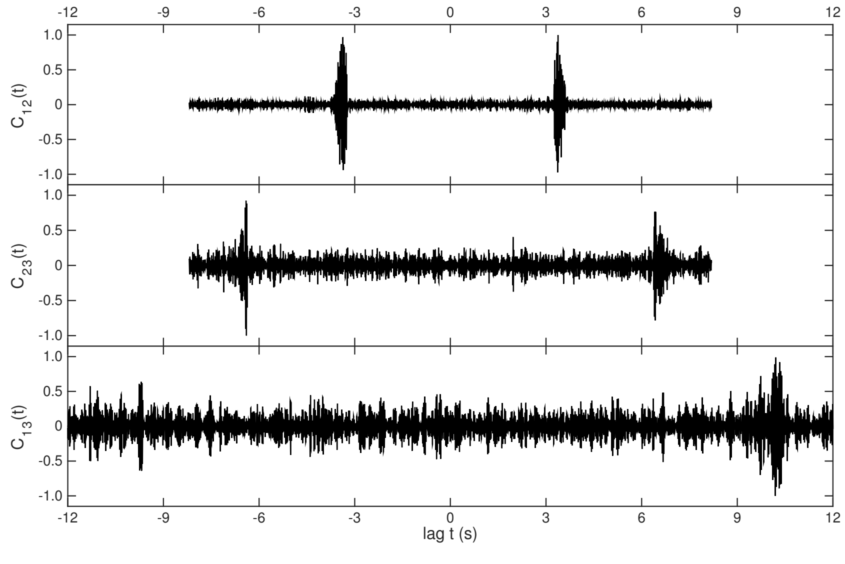

Figure 4.1: Measured CFs for the 1-2 (5 km separation), 2-3 (10 km separation) and 1-3 (15 km separation) instrument pair of deployment 1. The signal to noise ratio decreases as the separation increases.

isolate the modes from NCFs–to reconstruct the measured NCFs and improve their SNRs. From there, we move on to estimate the depth-averaged current speed in the experimental environment, using an effective sound speed approximation.

4.2 Time warping processing for dispersion analysis

4.2.1 Dispersion in shallow water environment

In the water, sound propagation has dispersive properties, i.e. sound waves at different frequencies propagate at different phase/group speed. Especially, in shallow water environment, due to the limit of water depth, sound waves suffer more bottom and surface reflections than in deep ocean. Thus, after certain distance, the propagating wave elongates in time, and eventually, normal modes naturally separate from each other due to their modal dependent speed. However, when the propagation distance is not long enough, the normal modes cannot separate from each other completely, i.e. the acoustic Green's function is composed of several modes that overlap with one another. Being able to analyze the dispersion relationship in shallow water, and more importantly, being able to isolate the normal modes from the acoustic Green's function, is very important to understand the physics of shallow water environment.

In Chapter 3, we have performed the waveform modeling and inversion of NCF. By plotting the NCFs in multiple narrow bands, we've got a glance of dispersion in 1-2 instrument pair. Here, we continue to explore the dispersion analysis in the shallow water environment, with 1-2, 2-3 and 1-3 instrument pair. By comparing the narrow band NCFs at difference propagation distance, we can see the modal separation evolution with distance. In addition to plotting NCFs in multiple 10 Hz bands, we also calculate the theoretical group speed of each mode at different frequency, and visualize the group speed with the NCFs in narrow bands in the same plot. Here, the theoretical group speed is calculated with the KRAKEN normal mode model, using the optimal eight-parameter model obtained in Chapter 3. The calculated group speed $c_g(f,m)$is a function of frequency f and mode number m, which represents the nature of sound wave dispersion.

Figure 4.2, 4.3 and 4.4 shows dispersion in the 1-2, 2-3 and 1-3 instrument pair wave fields, respectively. The red curves are the measured NCFs in multiple 10 Hz bands, with the center frequency of each 10 Hz band as the vertical axis. The blue curves are the simulated counterparts in each 10 Hz band. Yellow shadow depicts the arrival time of each narrow band, calculating from the group speed $c_g(f,m)$. Each slate of shadow corresponds to one mode. By comparison, it's obvious that dispersion effect grows as the separation between two locations increases from 5 km to 15 km. In Fig. 4.4, when traveling 15 km range, two modes are clearly separated without additional filtering techniques. On the contrary, in Fig. 4.2, the separation is not clear in any band; in Fig. 4.3, the separation is visible in the lower five bands, not in the higher four bands. For the cases where modes are not naturally separated, like the 1-2 and 2-3 instrument pairs, additional signal processing techniques are needed in order to isolate normal modes from the acoustic Green's function. In this chapter, we employ the time warping method to achieve this goal.

4.2.2 Time warping method in dispersion analysis

4.2.2.1 Time warping operators

The time warping operators are designed to compensate for the dispersive effect and isolate the modal components. It was firstly presented by Touze *et al.* (79) in 2009

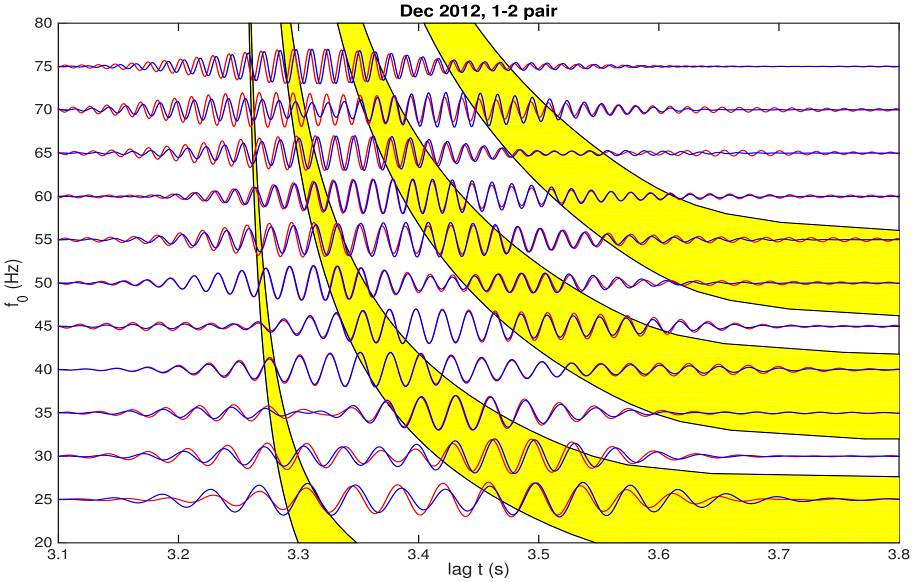

Figure 4.2: Dispersion plot of $C_{12}(t)$. Red curves are measured NCFs and blue curves are simulated NCFs, in multiple 10 Hz bands, with the center frequency as the vertical axis. Yellow shadowed zones represent the arrival time of four modes at corresponding frequency.

and then applied to geoacoustic inversion (80; 81; 82). Its essence is a nonlinear resampling of the Green's function. By resampling the original Green's function in the warped time domain, the dispersion is compensated and the normal modes occupy non-overlapping bands in the frequency domain. The warping operator depends on the type of the waveguide, i.e. the ocean environment. The warping operator for the ideal waveguide has been derived theoretically, and tested numerically. The steps associated with implementing time warping in an ideal waveguide are: given a Green's function $G(t)$ that contains the modes of a dispersive waveguide, resample $G(t)$ uniformly in warped time $t' = \sqrt{t^2 - t_r^2}$, where $t_r = r/c$ is the start time of deterministic structures, resulting in a time-warped signal $G(t')$; compute the spectra of $G(t')$ that shows the clearly-resolved modes in the frequency domain; band pass filter to isolate the contribution from a particular mode (m);apply the inverse warping operator $t = \sqrt{t'^2 + t_r^2}$ to transform back to the original time domain and reveal

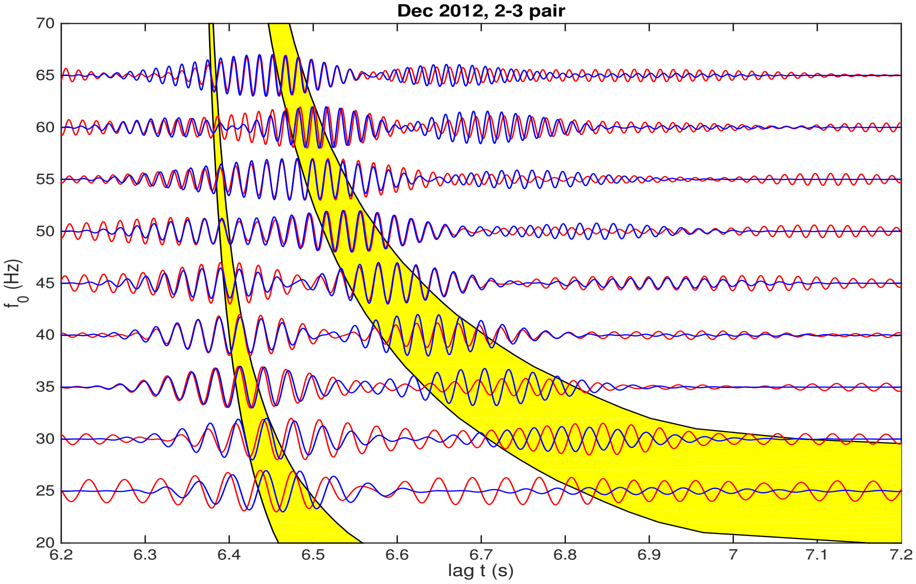

Figure 4.3: Dispersion plot of $C_{23}(t)$. Red curves are measured NCFs and blue curves are simulated NCFs, in multiple 10 Hz bands, with the center frequency as the vertical axis. Yellow shadowed zones represent the arrival time of two modes at corresponding frequency.

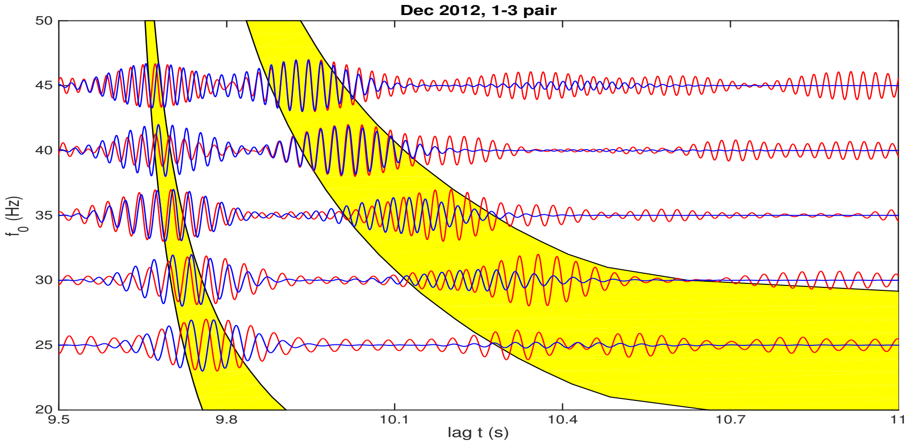

Figure 4.4: Dispersion plot of $C_{13}(t)$. Red curves are measured NCFs and blue curves are simulated NCFs, in multiple 10 Hz bands, with the center frequency as the vertical axis. Yellow shadowed zones represent the arrival time of two modes at corresponding frequency.

$G_m(t)$. In 2014, the warping operators were extended to the non-ideal waveguide by Niu *et al.* (83). In his work, sound speed profile is depth-dependent, and sea bottom is acoustic. Niu's operators are closer to the realistic ocean environment, but requires more computation work. For the low frequency band (20-70 Hz) in our study, we employs the warping operators for the ideal waveguide, assuming that they are good approximations in the frequency band of interest. For better results, we may consider Niu's operators in future work.

4.2.2.2 Simulation of time warping in an ideal waveguide

Here we run a simple test on the warping operator in an ideal waveguide. Firstly, we simulate the acoustic Green's function in the same shallow water environment as the 1-2 instrument pair. Instead of a half-space elastic bottom, we use a rigid bottom, i.e. we are assuming an ideal waveguide. Using the Short Time Fourier Transform (STFT), we can plot the spectrogram of the simulated GF to visualize the time frequency representation, i.e. the dispersion. As shown in Fig. 4.5(a), four modes are distinguishable, but the four modes cannot be isolated from each other with conventional filtering. Then, with the simulated GF, we apply the time warping operator, and plot its spectrogram using STFT, as shown in Fig. 4.5(b). The spectrogram of the warped GF shows four clearly resolved modes in frequency domain; the resolved four modes can be easily isolated by performing simple conventional filtering, which realizes our objective of modal separation.

4.2.2.3 Application of time warping to dispersion analysis of measured NCFs

After testing the warping operator on the ideal waveguide, we process the measured NCFs with the same warping operators. It should be noted that the ideal waveguide

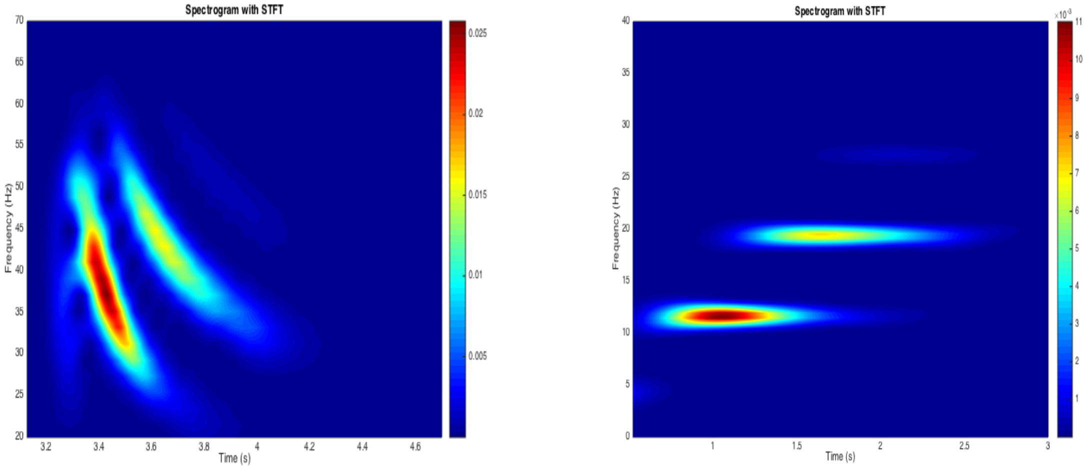

(a) Original GF

(b) Warped GF

Figure 4.5: Spectrogram of original and warped GF simulated in an ideal waveguide. Four modes are separated after warping transformation.

warping operator may not apply to the real ocean environment perfectly, but we can take it as a close approximation, as our experiment environment is relative shallow, and the water body is almost homogeneous.

Figure 4.6, 4.7, 4.8 show the spectrograms of the original and warped $C_{12}(t)$, $C_{23}(t)$ and $C_{13}(t)$ respectively. For $C_{12}(t)$, four modes are resolved after warping processing. For $C_{23}(t)$ and $C_{13}(t)$, only two modes are recognizable. In addition, $C_{23}(t)$ and $C_{13}(t)$ are more noisy than $C_{12}(t)$, as the peaks in Fig. 4.7 and 4.8 are smeared compared with Fig. 4.6.

If we apply a conventional band-pass filter to the spectrum of the warped NCFs, we can extract each single mode successfully. Figure 4.9, 4.10, 4.11 shows the isolated modes in multiple 10 Hz bands. Comparing with Fig. 4.2, 4.3 and 4.4, the normal modes of each NCF have been successfully extracted. Also, it should be noted that the fit between the simulation and measurement is very good in the extracted modes, and the near-optimality of the eight-parameter model obtained in Chapter 3 is veri-

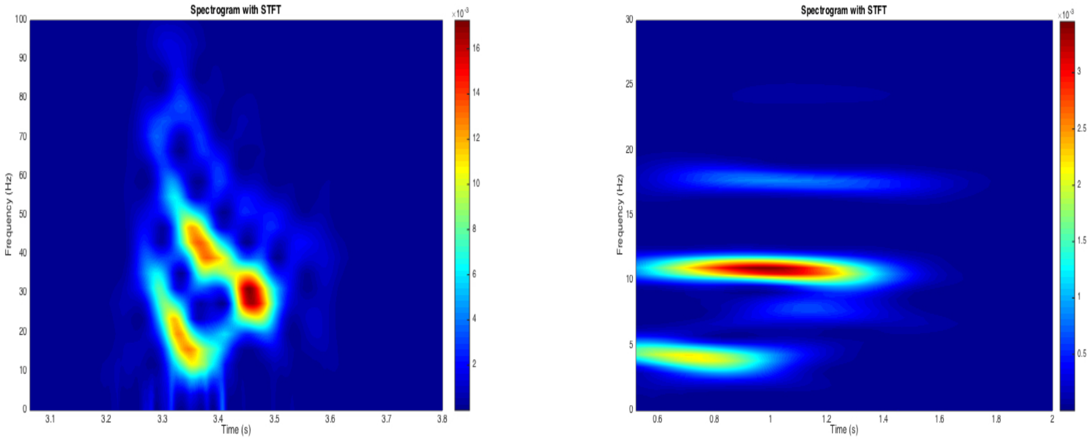

(a) Original NCF **(b)** Warped NCF

Figure 4.6: Spectrogram of original and warped $C_{12}(t)$. Four modes are separated after warping transformation.

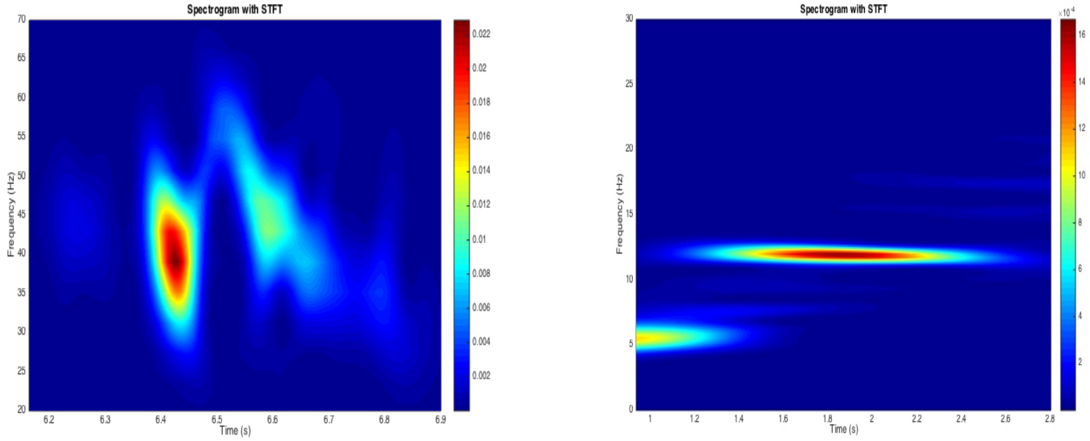

(a) Original NCF **(b)** Warped NCF

Figure 4.7: Spectrogram of original and warped $C_{23}(t)$. Two modes are separated after warping transformation.

fied again.

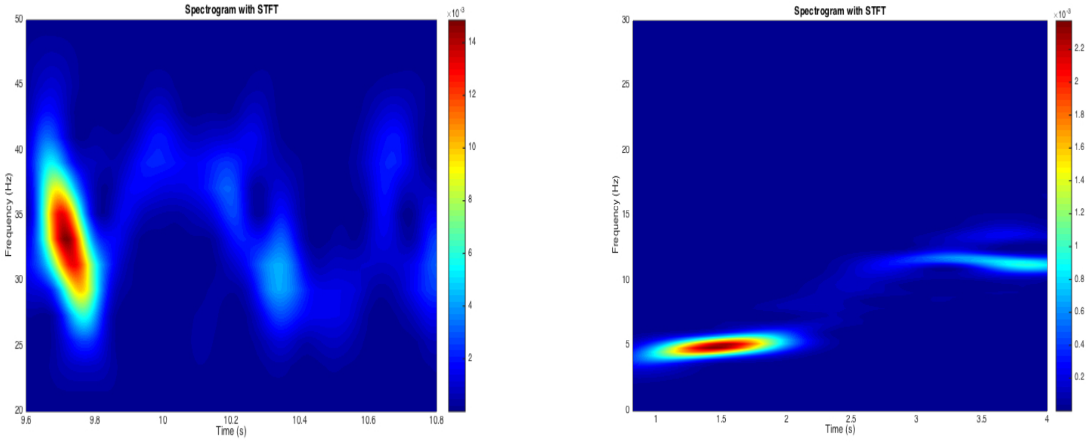

(a) Original NCF **(b)** Warped NCF

Figure 4.8: Spectrogram of original and warped $C_{13}(t)$. Two modes are separated after warping transformation.

4.3 Reconstruct the NCFs with time warping to improve SNR

4.3.1 Reconstruction of NCF in an ideal waveguide

The goal of this section is to improve the SNR in NCFs obtained in Section 4.1. The technique we employ is time warping processing, which is a signal processing technique that can be used to isolate normal modes from NCF. We firstly test the NCF reconstruction procedures on a two-point NCF in an ideal waveguide, with 5 km separation between two hydrophones that are located 5 m off the seafloor, similar to the instrument pair 1-2 in the field experiment. We reconstruct $C_{12}(t)$ in five steps: Process $C_{12}(t)$ with the forward warping operator, i.e. resample $C_{12}(t)$ with the warped time $t' = \sqrt{t^2 - t_r^2}$; Do the forward Fourier transform of warped signal $C_{12}(t')$, and isolate each mode using the conventional filtering based on the spectra, as shown in Fig. 4.12(a); Do the inverse Fourier transform of each isolated mode,

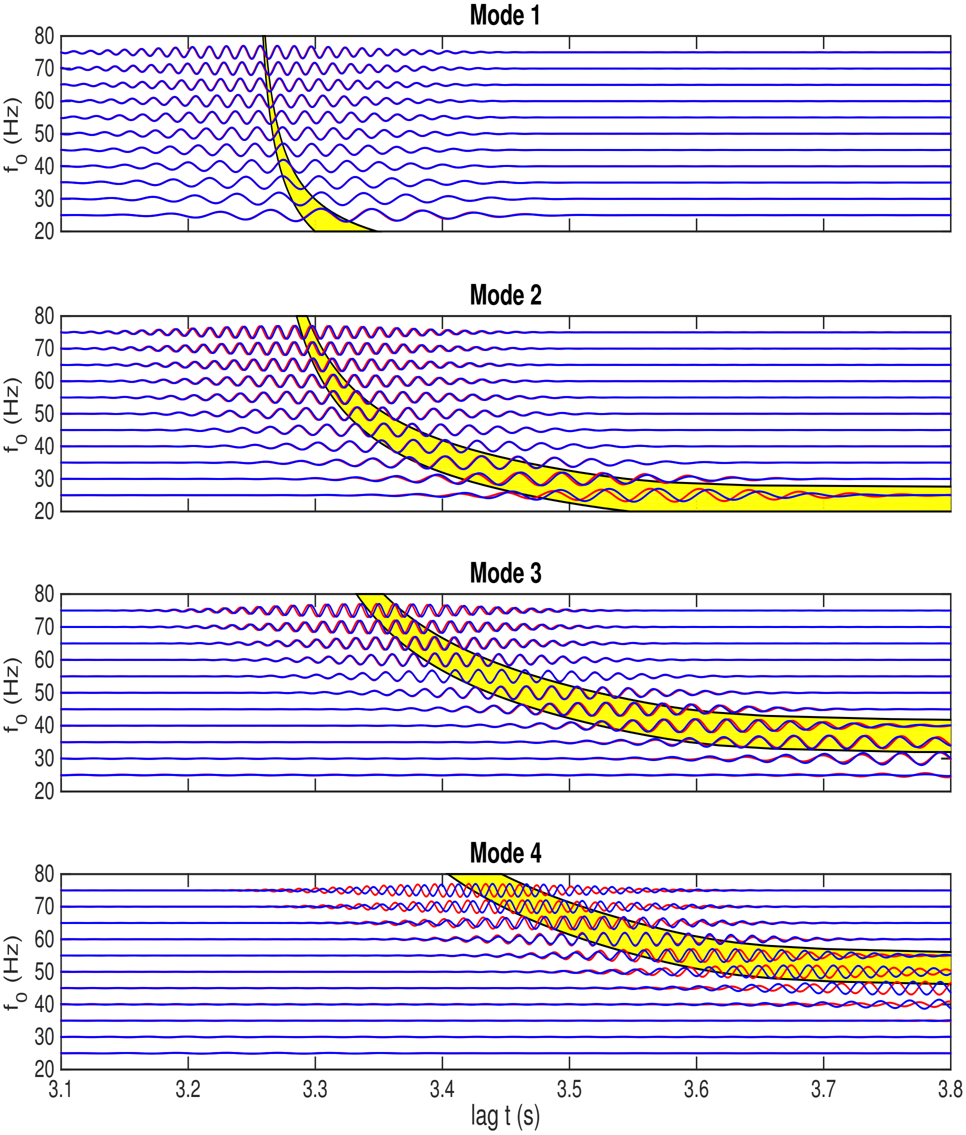

Figure 4.9: Isolated modes plot of $C_{12}(t)$. Red curves are measured NCFs and blue curves are simulated NCFs, in multiple 10 Hz bands, with the center frequency as the vertical axis. Yellow shadowed zones represent the arrival time of four modes at corresponding frequency.

and view the separated modes in the warped time domain, as shown in Fig. 4.12(b); Transform each mode of $C_{12}(t')$ back to the original time domain using the unwarping operator $t = \sqrt{t'^2 + t_r^2}$, as shown in Fig. 4.12(c); Sum up all the unwarped isolated

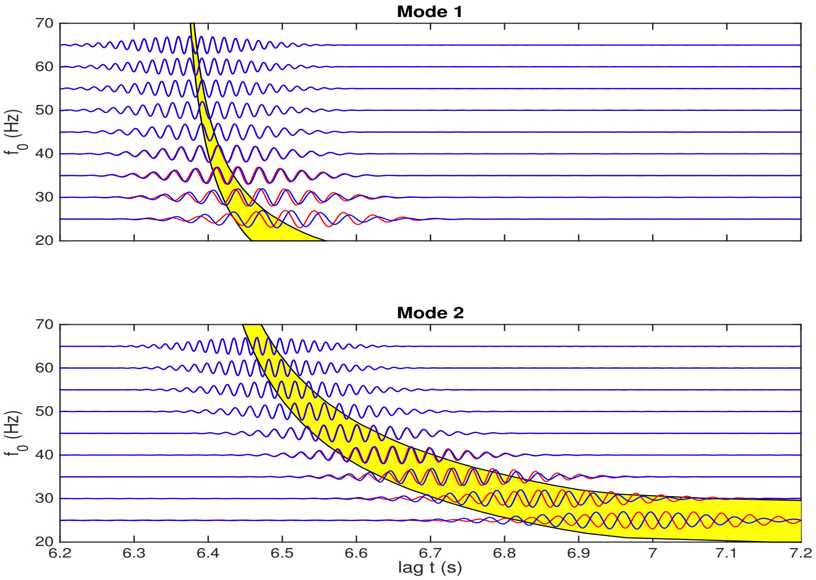

Figure 4.10: Isolated modes of $C_{23}(t)$. Red curves are measured NCFs and blue curves are simulated NCFs, in multiple 10 Hz bands, with the center frequency as the vertical axis. Yellow shadowed zones represent the arrival time of two modes at corresponding frequency.

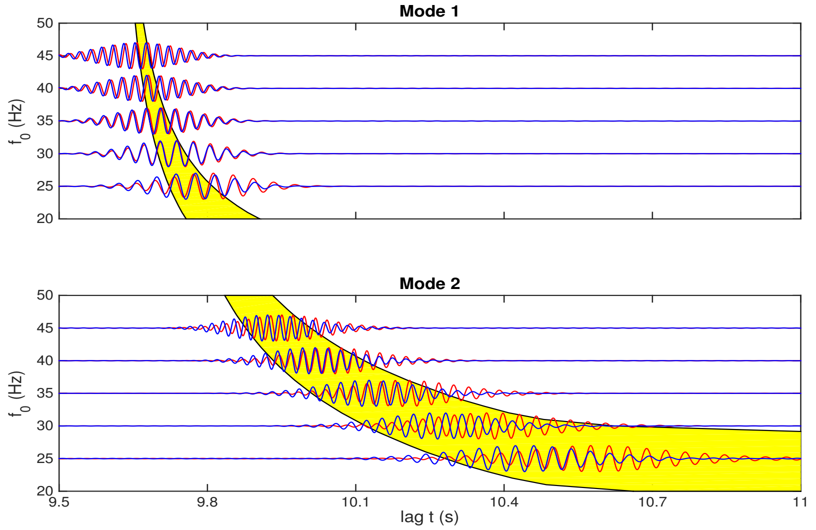

Figure 4.11: Isolated modes of $C_{13}(t)$. Red curves are measured NCFs and blue curves are simulated NCFs, in multiple 10 Hz bands, with the center frequency as the vertical axis. Yellow shadowed zones represent the arrival time of two modes at corresponding frequency.

modes to get the reconstructed NCF and compare with the original NCF, as shown in Fig. 4.12(d). The reconstructed NCF fits with the original NCF perfectly, with no difference in phase and negligibly small difference in amplitude. The simple test on the ideal waveguide verifies the feasibility of NCF reconstruction using time warping technique. For the measured NCFs, since the incoherent has no modal structures, the reconstruction procedures will effectively filter out the incoherent energy and enhance the deterministic structure.

4.3.2 Reconstruction of measured NCF in the coastal ocean environment

Following above reconstruction procedures, the NCFs obtained in Section 4.1 are all reconstructed. Figure 4.13, 4.14, 4.15 show the reconstructed lags of $C_{12}(t)$, $C_{23}(t)$ and $C_{13}(t)$, respectively. In Fig. 4.13, four modes are clearly resolved in the spectra, and the fit between measured and reconstructed lags is very good. In Fig. 4.14, two modes are clear in the spectra of both lags; through mode filtering and reconstruction, the signal is enhanced while the noise is suppressed. In Fig. 4.15, two modes are visible in the spectra of both lags, but the negative lag is much noisier than the positive lag; after reconstruction, the positive lag shows two strong modes with very low noise, while the negative lag has a clear mode 1 and a relatively poor-shaped mode 2; but still, it is obvious that mode 2 in negative lag becomes much more clear after reconstruction. The benefits of NCF reconstruction in improving SNR is further quantified in Table 4.1. By isolating the modes of measured NCFs with time warping technique, and reconstructing NCFs through summing up the isolated modes, we've successfully improved the SNR of measured NCFs, especially for $C_{23}(t)$ and $C_{13}(t)$. In particular, the SNR of negative lag of $C_{13}(t)$ increases from 1.44 dB to 17.69 dB

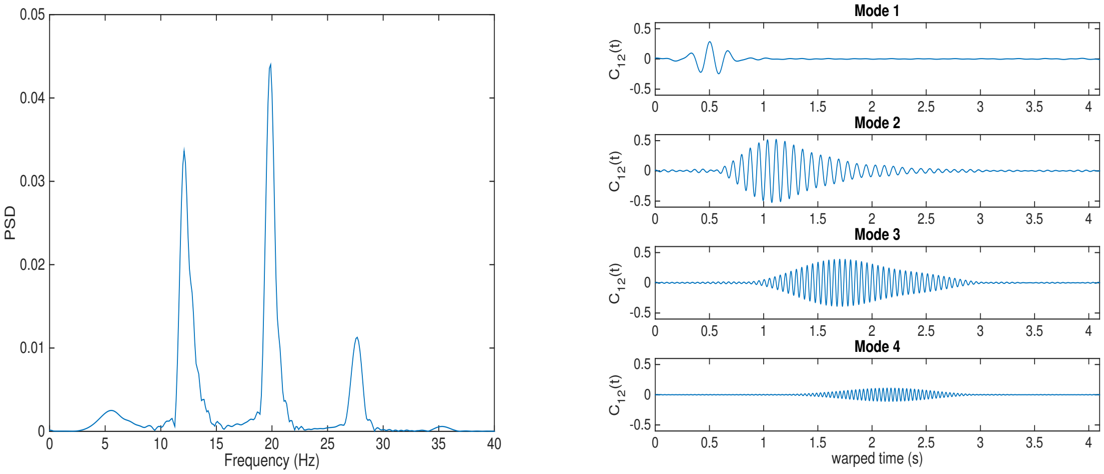

(a) Spectrum of the warped CF

(b) Warped modes

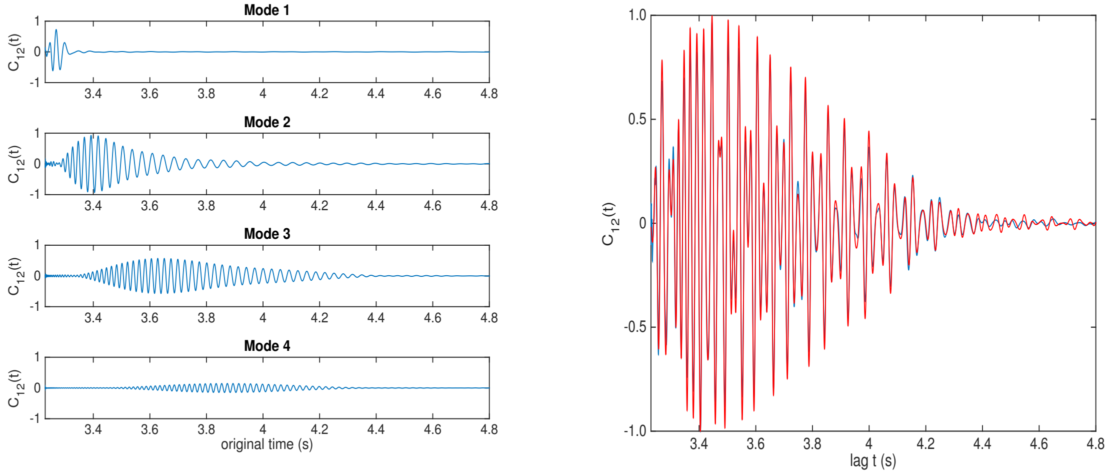

(c) Unwarped modes

(d) Simulated (in red) and reconstructed (in blue) CF

Figure 4.12: Simulation of CF reconstruction in an ideal waveguide using time warping method.

after reconstruction.

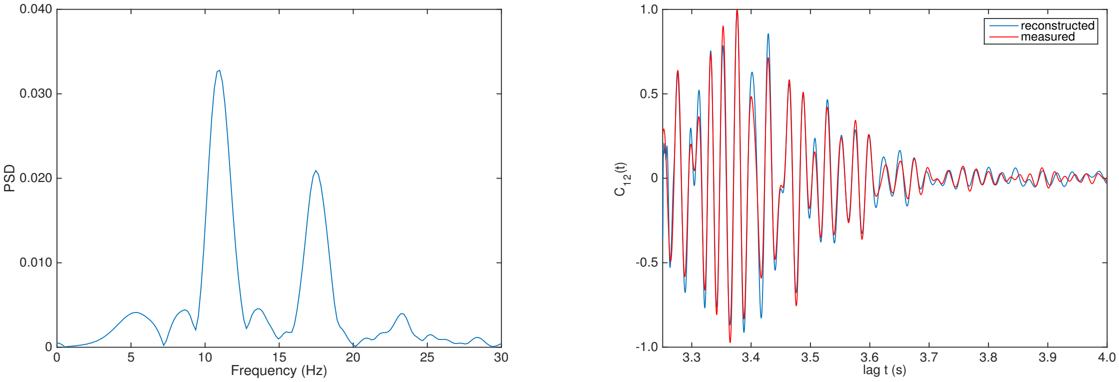

(a) Spectrum of warped $C_{12}(t)$, positive lag

(b) Measured (in red) and reconstructed (in blue) $C_{12}(t)$, positive lag

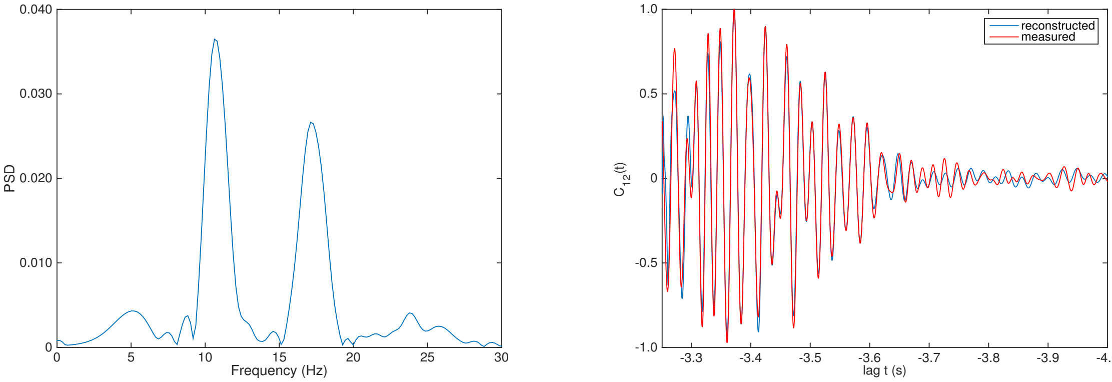

(c) Spectrum of warped $C_{12}(t)$, negative lag

(d) Measured (in red) and reconstructed (in blue) $C_{12}(t)$, negative lag

Figure 4.13: Reconstruction of measured $C_{12}(t)$ using time warping method.

Instrument Pair	$C_{12}(t)$		$C_{23}(t)$		$C_{13}(t)$	
NCF Type	Measured	Reconstructed	Measured	Reconstructed	Measured	Reconstructed
Positive Lag SNR (dB)	21.59	25.39	9.77	26.03	8.36	20.60
Negative Lag SNR (dB)	23.22	26.80	9.92	23.02	1.44	17.69

Table 4.1: Comparison of SNR of measured and reconstructed NCFs

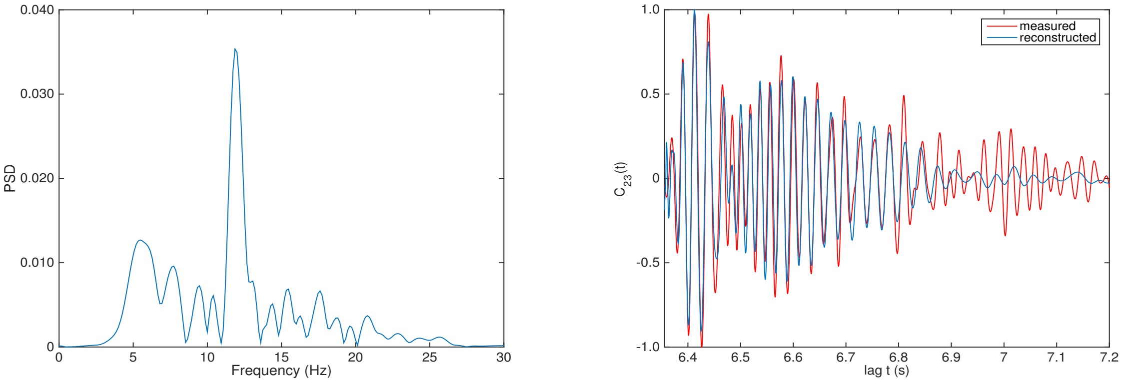

(a) Spectrum of warped $C_{23}(t)$, positive lag

(b) Measured (in red) and reconstructed (in blue) $C_{23}(t)$, positive lag

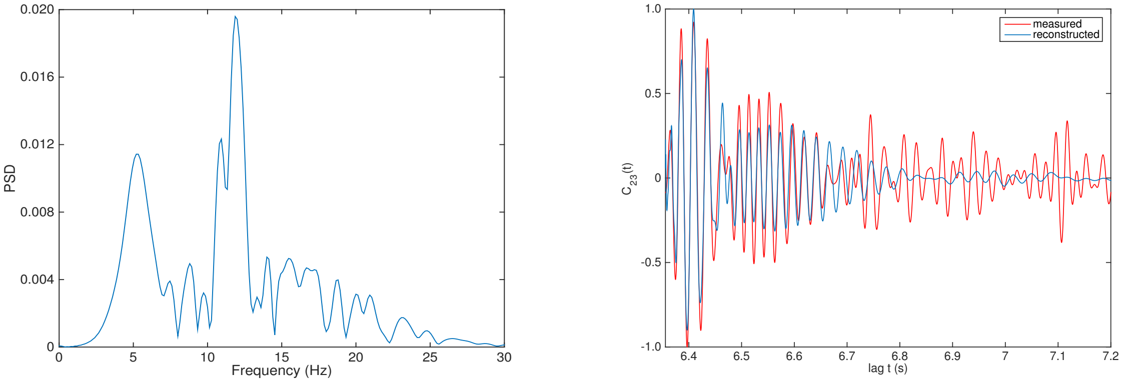

(c) Spectrum of warped $C_{23}(t)$, negative lag

(d) Measured (in red) and reconstructed (in blue) $C_{23}(t)$, negative lag

Figure 4.14: Reconstruction of measured $C_{23}(t)$ using time warping method.

4.4 Estimate current speed using effective sound speed approximation

4.4.1 Effective sound speed approximation in a slow moving medium

In this section, we estimate the ocean current speed from the reconstructed NCFs, based on an effective motionless medium approximation that is built on certain con-

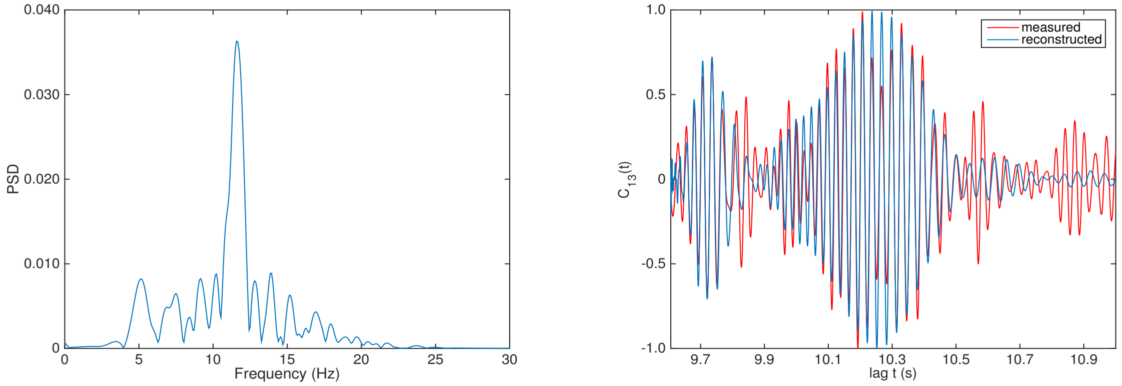

(a) Spectrum of warped $C_{13}(t)$, positive lag

(b) Measured (in red) and reconstructed (in blue) $C_{13}(t)$, positive lag

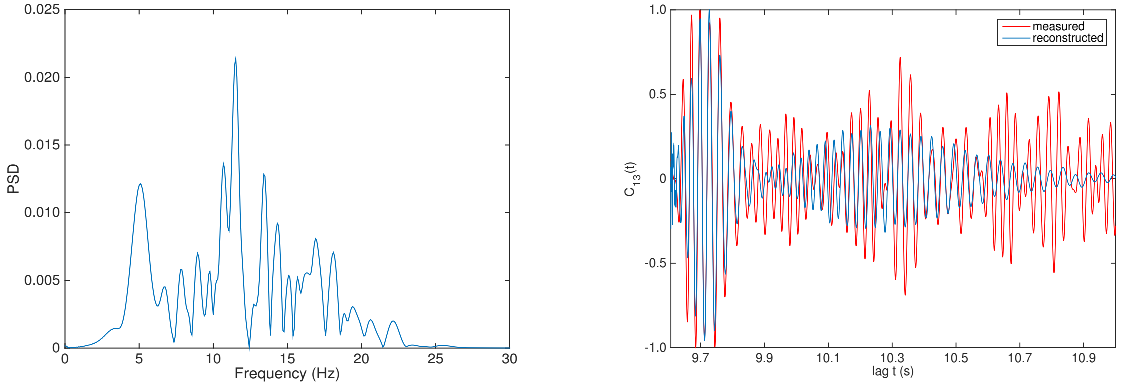

(c) Spectrum of warped $C_{13}(t)$, negative lag

(d) Measured (in red) and reconstructed (in blue) $C_{13}(t)$, negative lag

Figure 4.15: Reconstruction of measured $C_{13}(t)$ using time warping method.

ditions of applicability. The idea of approximating the acoustic field in an inhomogeneous moving medium with the acoustic field in an effective quiescent medium can be traced back to Lord Rayleigh (85). This idea is widely used in simulating sound propagation in the atmosphere when wind exists and in the ocean when current exists. By substituting the moving medium with an equivalent static medium, the governing acoustic wave equation is significantly simplified, and numerical modeling of corresponding acoustic field can be done with existing sound propagation models, including ray models, normal mode models as well as parabolic equation models.

In our experiment, sound speed variation in depth is less than 5 m/s over 100 m depth, as illustrated by Fig.1. Ship-based ADCP measurements during the deployment cruise show that the depth-averaged eastward and northward currents are approximately 0.4 m/s and 0.6 m/s, respectively. Through vector calculation, the overall current speed is 0.7 m/s, in the direction of 55° from north to east, which approximately falls on the direction of our hydrophone array. The dominant propagation paths have low grazing angles with respect to the seafloor. The above properties make the studied environment a qualified candidate to use the effective motionless medium approximation, given by Godin in 2002 (84). Through derivation, he gives a form of effective medium with

$$c_e = c + \vec{u} \cdot \vec{n}, \quad \rho_e = \rho \frac{c^2}{c_e^2}, \tag{4.1}$$

where c_e and ρ_e are effective sound speed and effective density; c and ρ are the sound speed and density in the moving medium; $\vec{u}$ is the current velocity and $\vec{n}$ denotes sound propagation direction. When the medium is a weakly inhomogeneous slow moving medium, i.e. $\frac{\delta c}{c} \ll 1$, $\frac{\delta \rho}{\rho} \ll 1$ and $u \ll c$, Godin shows that the acoustic wave equation in the moving medium reduces to

$$\nabla \cdot \frac{\nabla p}{\rho_e} + \frac{\omega^2}{\rho_e c_e^2} p = 0. \tag{4.2}$$

In addition, when grazing angle with respect to the reflecting surface is small, the boundary condition in the moving medium reduces to the boundary condition in the effective medium. Since both the weakly inhomogeneous slow moving medium condition and the small grazing angle condition are satisfied by our experimental environment, we can simulate the sound propagation using the effective motionless medium approximation on the KRAKEN normal mode model. By incorporating the current speed in the effective sound speed and density, the simulated NCF is dependent on current speed.

4.4.2 Method of current speed estimate

In Section 4.3, we've reconstructed the measured NCFs, which have higher SNRs than the original measured NCFs. The positive lags correspond to sound propagation from south to north (location 3 to 1), while negative lags correspond to sound propagation from north to south (location 1 to 3). Through numerical simulation, both positive lags and negative lags can be modeled by applying the effective motionless medium approximation, given in Eq.4.1. Note that $\vec{n}$ in positive and negative lags is exactly opposite. From previous work on waveform modeling and inversion (86), we've obtained an optimal eight-parameter geoacoustic model that approximates the experimental environment very well. Here, we simulate NCFs using the obtained eight-parameter geoacoustic model, combining the effective motionless medium approximation, which incorporates the current speed in the effective sound speed and density. For each instrument pair, we firstly run simulations with current speed varying from 0 to 1.5 m/s, pointing from location 3 to 1. Then, we calculate the two-norm misfit $M(u)$ between simulated and reconstructed NCFs,

$$M(u) = \int_{-t_{max}}^{-t_{min}} \left[C_{recon}(t,u) - C_{simu}(t,u)\right]^2 \, dt + \int_{t_{min}}^{t_{max}} \left[C_{recon}(t,u) - C_{simu}(t,u)\right]^2 \, dt, \tag{4.3}$$

where u is the value of current speed; t_{min} and t_{max} denote the starting and ending time of the deterministic structure in each NCF; $C_{recon}(t,u)$ is the reconstructed NCF while $C_{simu}(t,u)$ is the simulated NCF. $M(u)$ reaches the minimum at optimal u.

4.4.3 Results and discussion

Through a brute-force search, we find that the optimal depth-averaged current speeds are $u_{12} = 1.03$ m/s, $u_{23} = 0.49$ m/s, $u_{13} = 0.72$m/s for instrument pair 1-2, 2-3 and 1-3, respectively. It should be noted that u_{12}, u_{23} and u_{13} are obtained from independent search with corresponding reconstructed and simulated NCFs. Surprisingly, $\frac{1}{3}u_{12} + \frac{2}{3}u_{23} = 0.67$ m/s, which is very close to $u_{13} = 0.72$ m/s. The consistency $u_{13} \approx \frac{1}{3}u_{12} + \frac{2}{3}u_{23}$ is a good sign of the reliability of the estimated current speeds.

Figure 4.16 shows the comparison between simulated NCFs, obtained with the optimal current speed, and the reconstructed NCFs, obtained with time warping technique. For $C_{12}(t)$ in the 20-70 Hz band, the simulated NCFs fit the reconstructed NCFs very well, with a perfect phase match and some minor amplitude misfits. For $C_{23}(t)$ in the 20-70 Hz band, the fit is very good in Mode 1, ending at 6.5 s approximately, but relatively poor in Mode 2, especially in amplitude. The difference in amplitude is partially because of the asymmetry in the two lags of $C_{23}(t)$, referring to Fig. 4.1, and partially because of the weighting function applied in the simulation, referring to Zang *et al.*, 2015 (86). Modal arrivals within 6.7 s to 6.9 s time span, which correspond to the low frequency components of Mode 2 arrivals, illustrate obvious phase misfit in both the positive lag and the negative lag; this phenomena is more obvious in Fig. 4.10. This is due to the inadequacy of the eight-parameter geoacoustic model in low frequencies. The geoacoustic model in our simulation simplifies the seafloor structure as a 9 m fluid sediment layer overlying a half-space fluid bottom, which is quite limited at low frequencies where bottom interactions happen more often than in high frequency bands. In spite of the aforementioned defects, the 2-3 instrument pairs still yield a good match between the reconstructed and simulated NCFs. Thus, the current speed estimation at 10 km separation is reliable.

For $C_{13}(t)$, which is calculated in the 20-50 Hz band, the fit in Mode 1 is good in both the positive and the negative lags; the misfit in Mode 2 is significant. This phenomenon is consistent with Fig. 4.11. Two factors can be accounted for it. Firstly, our geoacoustic model was obtained with the 1-2 instrument pair NCFs in the 20-70 Hz band. For the 1-3 instrument pair, since the 50-70 Hz band components are too noisy to be included, we only calculate NCFs in the 20-50 Hz band. Similar to the problem analyzed for the 2-3 instrument pair, the geoacoustic model in our simulation is inadequate at low frequencies, which partially explains the misfit in later arrivals of Mode 2 of $C_{13}(t)$. Secondly, the separation for the 1-3 instrument pair is approximately 15 km, which is three times of the 1-2 instrument pair. For longer propagation range, sound waves suffer more bottom interaction and attenuation, especially at low frequencies. These two factors are the major reasons for the misfit in Mode 2. However, with the satisfying performance of Mode 1, and considering that the measure we defined to search for optimal current speed in Eq. 4.3 emphasizes the fit in phase, the current speed estimation at 15 km range is still believable, even if the simulation of Mode 2 is not good.

Now we evaluate our estimation results with reference to previous study (64). Previously, Godin *et al.* (2014) has estimated the depth-averaged current speed based on acoustic reciprocity. In that study, the time difference between the positive and negative lag was employed to investigate the relative clock drift and the current speed at the same time. Their results show that: the clock drifts for the 1-2 and 2-3 instrument pair is 0.917 ms/day and -0.490 ms/day, respectively; the depth-averaged current speed is -0.47 m/s based on the 1-2 instrument pair, and the result obtained from 2-3 instrument pair is 5% higher. It should be mentioned that the frequency band in Godin's work is 20-50 Hz band, which is different from our 1-2 and 2-3 instrument pair calculations. In addition, the method employed to find the good clock

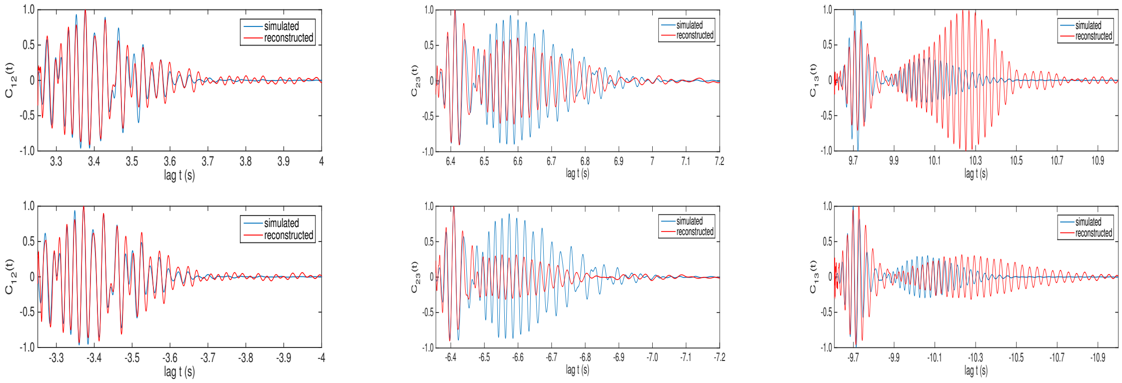

Figure 4.16: Simulated NCFs (in blue) using effective sound speed and reconstructed NCFs (in red) using time warping. Left: 1-2 instrument pair; middle: 2-3 instrument pair; right: 1-3 instrument pair.

drift is also different in two studies. With above difference in mind, we've tested $C_{12}(t)$ in the 20-50 Hz band, and find that the SNR is best when relative clock drift is 1.01 ms/day, and the corresponding current speed is 0.81 m/s. It's obvious that the difference of relative clock drifts in two studies contributes to the difference of current speed estimation using the 1-2 instrument pair. The results obtained from 2-3 instrument pair show better match in both studies. Moreover, with the NCF reconstruction processing, we've successfully estimated the current speed with the 1-3 instrument pair, which was not completed in previous study due to the low SNR in $C_{13}(t)$. Our results show that $\frac{1}{3}u_{12} + \frac{2}{3}u_{23} = 0.67$ m/s, about 7% smaller than u_{13}=0.72 m/s, which is a good consistency within the estimations at three separations. The ship-based along track ADCP measurement gives a current speed of about 0.7 m/s in the upper 70 m, which is 3% smaller than u_{13}. With the good consistency with previous study and the ADCP measurement, we think the new current speed estimation method presented in this Chapter is reliable and robust, and the reconstruction of NCFs can significantly extend the application of noise interferomentry.

Several aspects of future improvements are discussed here. As mentioned earlier in Section 4.2, the warping operators employed in this Chapter are based on the ideal waveguide. The geoacoustic model in our simulation is more complicated than the ideal waveguide. Thus, modal separation and NCF reconstruction can be improved with a more complicated and realistic warping operator pair. The other thing that should be noted is that the effective sound speed given in Eq. 4.1 is approximated by $c_e = c + u$, which ignores the modal dependency and frequency dependency in the propagation angle of each mode. This approximation is checked by monitoring the wave number $k(f, m)$ in NCF simulations. For both upper bound and lower bound of frequency band of each mode, the propagation angles are less than 30 degree, and the correction that applies to the estimated current speed is less than 10%. Thus, the approximation $c_e = c + u$ is acceptable. More accurate current speed estimates can be obtained by incorporating the modal and frequency dependency in both the effective sound speed and the effective density, as defined in Eq. 4.1.

4.5 Summary

In this chapter, we have employed the time warping transformation to analyze the dispersion in shallow water environment. Our study started with the simulated Green's function (GF) in an ideal waveguide. The time warping operator helps us to isolate four normal modes from the simulated GF using conventional filtering. Then we applied the time warping operators to the noise cross-correlation function (NCF) calculated from the ambient noise data in the shallow water environment. Results show that after time warping transformation, we have successfully extracted the normal modes from the measured NCFs, at 5 km, 10 km and 15 km separation. The extracted modes of the measured NCFs fit the modes of the simulated NCFs and the corresponding group speed very well, at all separations considered here.

Noise interferometry is a low-cost passive acoustic remote sensing method. Yet the signal-to-noise-ratio (SNR) of the NCF decreases significantly with the separation of two hydrophones, thus its application is quite limited. Thus, inspired by the success of aforementioned modal separation, we have presented a method to improve the SNR of NCFs in a highly dispersive shallow water environment. The reconstruction method not only successfully recovers the NCF in Pekeris waveguide simulation, but also effectively improves the SNR of measured NCFs, even for the 15 km separation.

Using the reconstructed NCFs, the current speed is estimated based on an effective motionless medium approximation. Our experimental environment, which is an ideal weakly inhomogeneous slow moving medium, satisfies the effective motionless medium approximation conditions. The optimal depth-averaged current speed is obtained by minimizing the two-norm misfit between the reconstructed and simulated NCFs. We obtained the optimal estimates of depth-averaged current speed to be u_{12} = 1.03 m/s, u_{23} = 0.49 m/s, u_{13} = 0.72 m/s for instrument pair 1-2, 2-3 and 1-3, respectively. The current speed estimates show good consistency not only with each other ($u_{13} \approx \frac{1}{3}u_{12} + \frac{2}{3}u_{23}$), but also with the ship-based ADCP measurement ($\approx$0.7 m/s). Through reconstruction, the current speed is successfully estimated from NCFs at 15 km separation for the first time.

Chapter 5

Low-frequency Long-range Communication in Deep Ocean

5.1 Background

Long-range underwater communication in the ocean is extremely challenging due to multi-pathing; many ray paths connect fixed points. The transient acoustic Green's function plays a vital role in quantifying this phenomenon. Compared with wireless electromagnetic communication in the air, acoustic communication in the ocean is much more complicated. Sound propagation in the ocean is usually affected by many factors. Firstly, inhomogeneity of underwater environment, including the variation of salinity and temperature with depth, results in inhomogeneity of the sound speed. This leads to sound rays propagating along multiple paths. Multi-path propagation can prolong and distort the transmitted signal, and lead to inter-symbol interference in underwater acoustic communication. The second factor that affects the accuracy in underwater communication is ambient noise, including ship traffic noise, wind-dependent noise, turbulent pressure fluctuations, etc. Under some circumstances, ambient noise is much stronger than the signal and thereby make the signal very difficult to identify. The third factor is the time-varying environment. All these factors make the extraction of acoustic Green's function in the ocean very challenging.

In this chapter, we present an active method, inverse filter processing, to extract the acoustic Green's function in deep ocean. This method is designed to work in long-range deep-ocean communication.

5.2 Theory

The solution to the acoustic wave equation with a transient point source at $\mathbf{x}_0$

$$\nabla^2 p - \frac{1}{c^2(\mathbf{x})}\frac{\partial^2 p}{\partial t^2} = -\delta(\mathbf{x}-\mathbf{x}_0)s(t) \tag{5.1}$$

can be written as a convolution,

$$\begin{aligned} p(\mathbf{x}|\mathbf{x}_0,t) &= G(\mathbf{x}|\mathbf{x}_0,\tau) * s(t) \qquad (5.2)\\ &= \int_{-\infty}^{\infty} G(\mathbf{x}|\mathbf{x}_0,\tau)s(t-\tau)d\tau. \end{aligned}$$

Here $g(\mathbf{x}|\mathbf{x}_0)$ is the transient Green's function, or impulse response function, which satisfies Eq.(5.1) with $s(t)$ replaced by $\delta(t)$.

For simplicity Eq.(5.2) is written in the following as

$$p(t) = G(t) * s(t). \tag{5.3}$$

Take the Fourier Transform on both sides of Eq.(5.3), the convolution in time domain turns into a product in frequency domain

$$\bar{p}(\omega) = \bar{G}(\omega)\bar{s}(\omega), \tag{5.4}$$

where $\bar{G}(\omega)$ and $\bar{s}(\omega)$ are the Fourier transform of $G(t)$ and $s(t)$, respectively.

From Eq.(5.3) and Eq.(5.4), it is clear that $G(t)$ has to be known in order to recover an unknown communication signal $s(t)$. Using Inverse Filter Processing (IFP), the Green's function $G(t)$ can be estimated from $p(t)$, if $s(t)$ is known. Let $s_m(t)$ denote a known transient source function and $p_m(t)$ the corresponding response function. Then

$$p_m(t) = G(t) * s_m(t), \tag{5.5}$$

$$\bar{p}_m(\omega) = \bar{G}(\omega)\bar{s}_m(\omega). \tag{5.6}$$

At the receiver, the Green's function can be recovered as a ratio

$$\bar{G}(\omega) = \frac{\bar{p}_m(\omega)}{\bar{s}_m(\omega)}. \tag{5.7}$$

Then, an unknown communication signal $s_c(t)$ satisfies

$$p_c(t) = G(t) * s_c(t) \tag{5.8}$$

in time domain, and

$$\bar{p}_c(\omega) = \bar{G}(\omega)\bar{s}_c(\omega) \tag{5.9}$$

in frequency domain.

Combining Eq.(5.7) and (5.9), the transmitted communication signal can be recovered as

$$\begin{aligned}\bar{s}_c(\omega) &= \frac{\bar{p}_c(\omega)}{\bar{G}(\omega)} \\ &= \frac{\bar{p}_c(\omega)\bar{s}_m(\omega)}{\bar{p}_m(\omega)} \\ &\approx \frac{\bar{p}_c(\omega)\bar{p}_m^*(\omega)\bar{s}_m(\omega)}{|\bar{p}_m(\omega)|^2 + \varepsilon^2},\end{aligned} \tag{5.10}$$

where the superscript $*$ denotes complex conjugation.

Considering that the ambient noise is non-coherent, and the communication signal is coherent, the inverse filter processing can perform better when the Signal to Noise Ratio (SNR) is low by averaging over time or space using multiple receivers, as illustrated in Eq.(5.11)

$$\bar{s}_{cavg}(\omega) = \frac{1}{M}\sum_{i=1}^{M} \bar{s}_{ci}(\omega), \tag{5.11}$$

where M is the number of temporal records for one hydrophone at different time or the number of hydrophones in the array.

Taking the inverse Fourier transform on both sides of Eq.(5.11), we can recover the transmitted communication as

$$s_c(t) = F^{-1}[\bar{s}_{cavg}(\omega)]. \tag{5.12}$$

5.3 Deep ocean experiment

5.3.1 Experiment setup

To test the performance of IFP method, an experiment was carried out in North Pacific ocean. The experiment equipment was part of the Acoustic Thermometry of Ocean Climate (ATOC) project. The source was located near Kauai Island (22.3492 N, 159.5700 W) in Hawaii, while the receivers (29.5835 N, 147.7429 W) were in the northeast direction to the source. The bearing angle of the receiver was 58.2811°. The horizontal distance between the source and the receiver was 1428.60 km. The source was 810 m deep, while the receiver was 1320 m deep. The receivers were an array of hydrophones mounted on a sea mountain, with an inclining angle of 20°.

To apply the IFP method, two sets of signals were transmitted. The precursor signal was composed of 1023-digit M sequence, modulated with a 75 Hz sinusoidal carrier wave in a binary phase-shift key. The communication signal was composed of a 1024-digit personally constructed binary sequence, modulated in the same pattern as the precursor signal. The communication signal was supposed to be of the same length as the precursor signal. However, due to a glitch in the correspondence, one more digit was transmitted in the real experiment. This glitch could deteriorate the performance of the IFP method, which will be shown explicitly later in the section of numerical simulation. The total length of transmitted signal was 1200 seconds, with 298 seconds of precursor signals and 902 seconds of communication signals. The sampling frequency at the receivers was 300 Hz, which was four times of the carrier frequency.

5.3.2 Experiment results

In the real ocean experiment, the number of hydrophones in the array is unknown to us. All the data we have in hand are from the same hydrophone. The experiment was carried out every four hours, on every Friday in seven consecutive weeks. So in total, we have 42 records to use. To improve the SNR, we can also use Eq.(5.11) and employ the temporal diversity in the analysis of real data, instead of the spatial diversity in the simulation.

Here, the measure of communication success we employed is the bit error rate (BER), which is the rate between the misinterpreted bits to the length of the communication signal. The result of the real ocean experiment is illustrated in the Fig.(5.1).

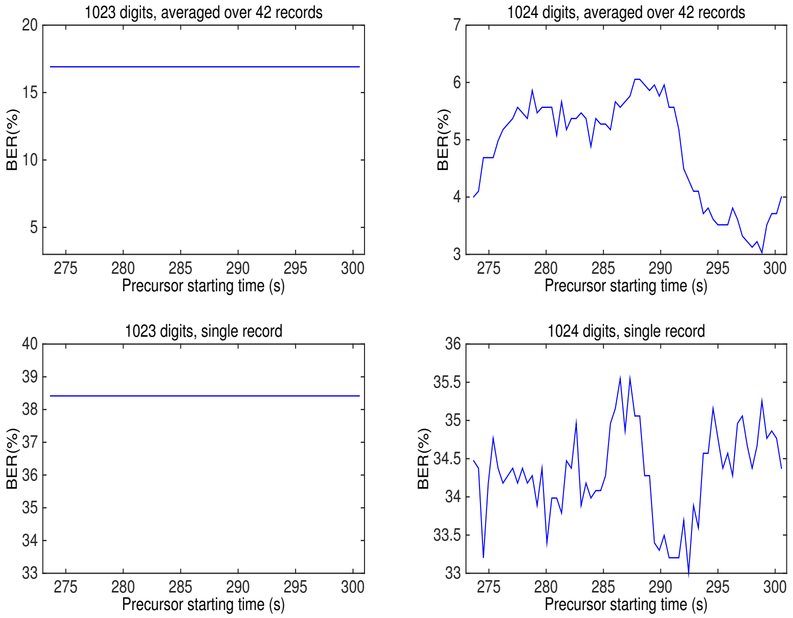

Figure 5.1: Results of deep ocean acoustic communication experiment.

5.4 Numerical simulation

5.4.1 Motivation

To compare with the results of data processing of the ocean experiment, a numerical simulation was run on computer. The numerical simulation serves the following purposes. Firstly, it provides an ideal environment that doesn't vary with time, which simplifies the complexity of underwater environment and provides a simple test of the IFP method. Secondly, in the simulation, we can control the noise level, and evaluate the performance of IFP under different SNRs. Thirdly, since we intended to transmit the communication signal with the same length as the precursor, but failed to do it in the real ocean experiment, we can do it in the simulation and compare the results of the two cases. In summary, by posing the problem in the controllable environment, we can get a reliable reference in interpreting the results of the ocean experiment.

In the simulation, the environmental data were extracted from National Oceanographic Data Center, World Ocean Atlas 2005. Plugging the environmental data into the ray tracing model, we can get the impulse response functions at the receiver. With the impulse response functions, we can simulate the received signal by convolving with transmitted signal and then recover the communication signal with the IFP method.

5.4.2 Simulated impulse response function

In the simulation, there are 21 hydrophones evenly distributed in a vertical array, ranging from 900 m deep to 1600 m deep. The impulse response function is different at different hydrophone, as illustrated in Fig.(5.2).

To illustrate the multipath propagation effect, one digit signal (two cycles of

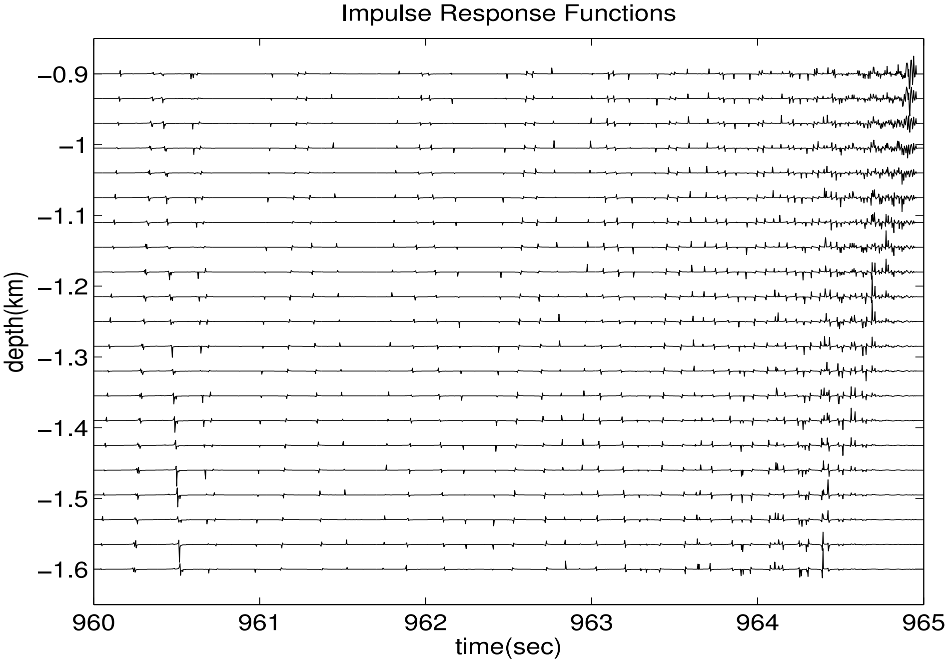

Figure 5.2: Simulated impulse response functions of an vertical array using a ray model.

sinusoidal wave) is convolved with the impulse response function at the tenth hydrophone, and the received signal is shown in Fig.(5.3).

Fig.(5.3) shows how one-digit signal can be distorted and blurred after long distance propagation. When the transmitted signal has more digits, there will be more overlaps in the received signal, which will result in intersymbol interference. Without appropriate processing, it is difficult to extract the original transmitted signal accurately, even if no noise is taken into account.

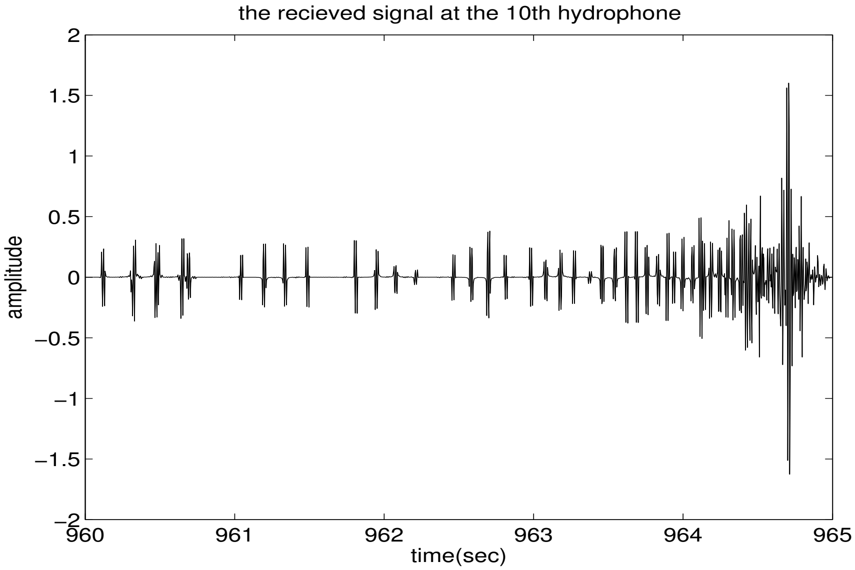

Figure 5.3: Illustration of the multipath propagation

5.4.3 Signal processing

After convolving the transmitted signal (containing the precursor signal and the communication signal) with the simulated impulse response functions, the received signals at the array are generated. Applying the IFP method to the received signal at each channel with Eq.(5.10), averaging over all hydrophones with Eq.(5.11), and then taking the inverse Fourier transform with Eq.(5.12), we can get the recovered communication signal. After demodulation, we can then calculate the bit error rate (BER) and evaluate the performance of the IFP method.

As mentioned earlier, the communication signal was intended to be of the same length as the precursor signal. So, in the numerical simulation, we studied both cases: the one with 1023-digit communication signal and the one with 1024-digit communication signal.

We want to evaluate the performance of the IFP method under different SNR. To do this, we compare the BERs of the two cases under different SNR.

5.4.4 Simulation results

For the case where the communication signal has 1024 digits, we have to interpolate in the spectrum of the precursor signal. The interpolation will affect the accuracy of the inverse filter processing results. Correspondingly, the BER varies with the starting point of the coherent stacking of the precursor signal.

Figures 5.4, 5.5, 5.6, 5.7, 5.8 show the bit error rate for different values of SNR. The two plots on the top are generated with multiple records, while the bottom two plots are obtained with a single record. The two plots on the left are the results of the case where the acoustic communication contains 1023 digits, same as the precursor signal. The two plots on the right hand side are the results of the case where the communication signal has 1024 digits, which is the same as the real experiment. By plotting the four plots in one figure, we can conveniently compare the results horizontally and vertically.

Comparing the two plots horizontally, we can find that the BER of the case of 1024-digit communication signal varies periodically with the starting point of the precursor signal. It is due to the discrepancy in the signal lengths and the interpolation in the inverse filter. This property appears to be unavoidable.Comparing the two plots vertically, we can find that the BERs of the array data are always better than BERs of a single record when Gaussian white noise is added. This is reasonable since the ambient noise is non-coherent while the transmitted signals are coherent. So more records can help to reduce the effect of the ambient noise on the communication and thereby improve the BERs significantly.

When the noise level increases, the BERs increase accordingly. When SNR = -30 dB, even the array data cannot recover the communication signal clearly, and the BER is about 11% for the case of 1023-digit and 9% for the case of 1024-digit.

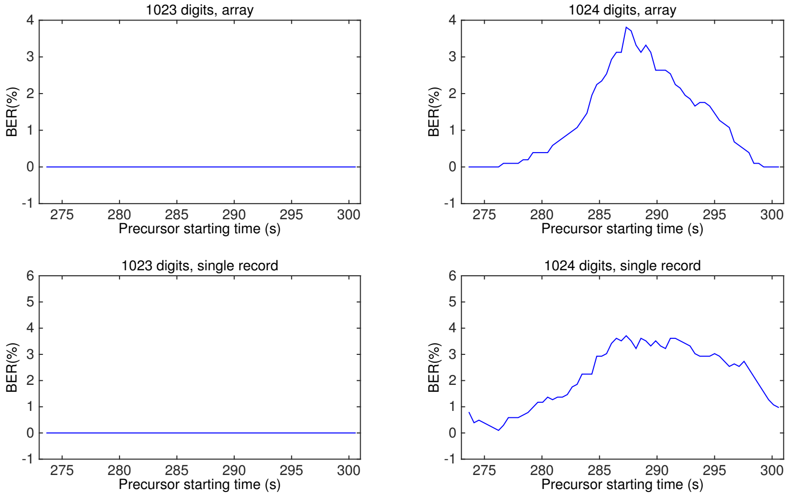

Figure 5.4: Bit error rate without ambient noise.

5.5 Summary

By comparing the experimental results with the numerical simulations, we've verified that the communication signal in the real experiment has 1024 digits, which is the reason of the periodic variation of the bit error rate curve. The simulations also show

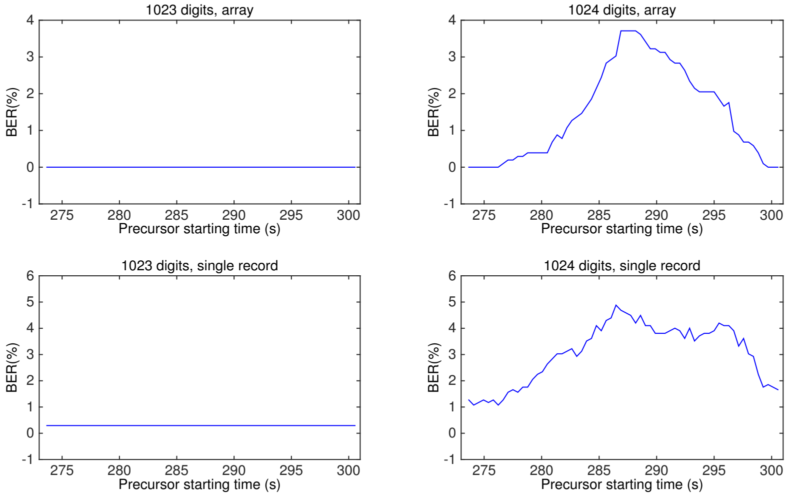

Figure 5.5: Bit error rate when SNR = -10 dB.

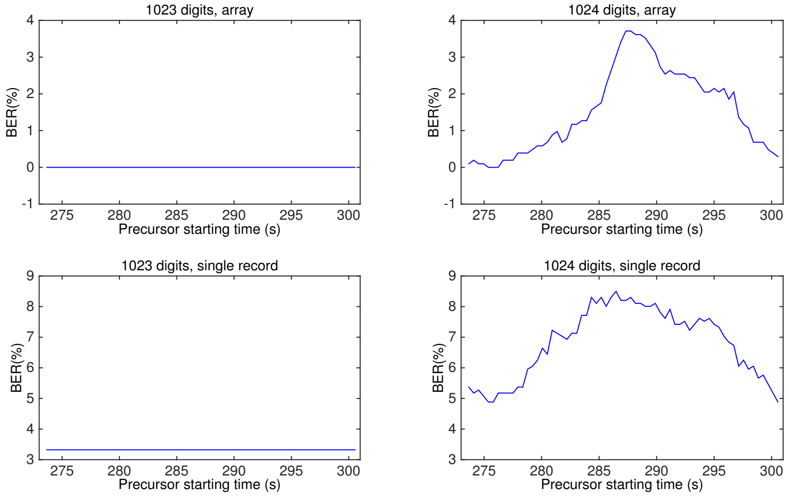

Figure 5.6: Bit error rate when SNR = -20 dB.

that if the communication signal is of the same length as the precursor signal, the BER will be higher. However, the real communication signal has 1024 digits, which is an intrinsic experiment glitch and cannot be fixed in the period of data processing. Besides, the data we have in hand is quite limited. If we have access to the array data and improve the SNR via array beam-forming, we can get a better BER, too.

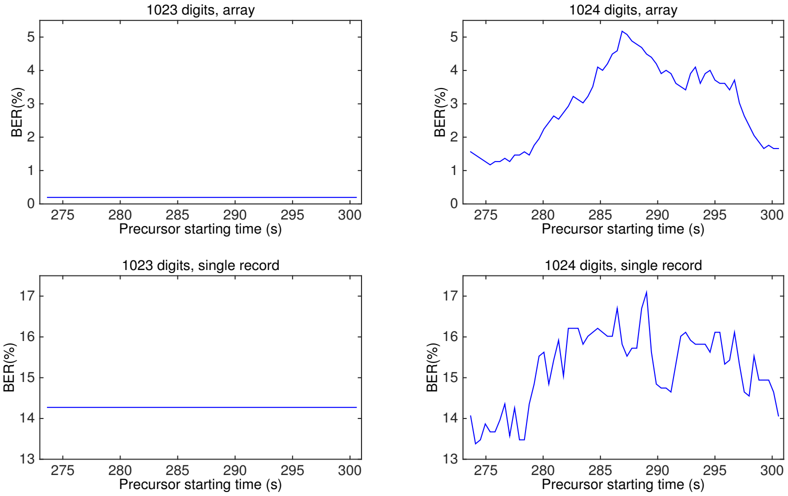

Figure 5.7: Bit error rate when SNR = -25 dB.

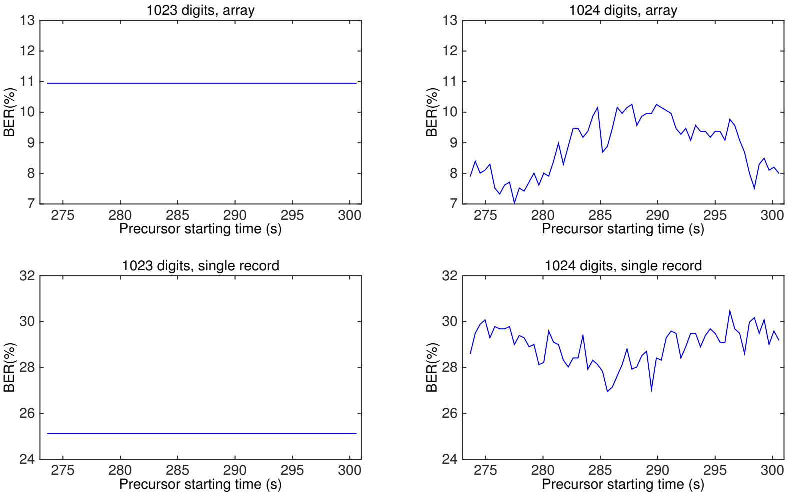

Figure 5.8: Bit error rate when SNR = -30 dB.

Chapter 6

Conclusion

6.1 Overview

The overall goal of this dissertation is to explore the methods of acoustic Green's function extraction in the ocean and to investigate the application of the acoustic Green's function to ocean properties studies. The goal has been achieved through the studies in Chapter 2 to 5.

The method of noise interferometry, which aims to extract acoustic Green's function from ambient noise cross-correlation functions, was tested through field experiments both in a coastal ocean environment and a mid-deep ocean environment. In our data, the performance of noise interferometry is better in the shallow water environment, where the deterministic structure of acoustic Green's function was obtained at 5, 10 and 15 km separation. The extracted Green's function in the studied coastal ocean environment was further explored for waveform modeling, geoacoustic inversion, dispersion analysis, modal separation, reconstruction and ocean current speed estimation. In the mid-depth ocean, the extracted Green's function doesn't show stable/consistent deterministic structures over the total experiment time. The possible factors that affect the performance of noise interferometry were discussed, including the noise source composition, ocean current strength and stability, and acoustic properties of environments.

The method of inverse filter was tested in a low-frequency long-range deep-ocean acoustic communication experiment. The acoustic Green's function was successfully extracted from the precursor signal, which was known at both the source and the receiver. The communication signal, which was transmitted following the precursor signal and was unknown to the receiver, was interpreted. Due to the glitch in the communication signal length and the lack of multi-channel data, the bit-error-rate of the recovered communication signal was about 3%, which is good but not superb.

The two methods presented in this dissertation represent the passive and active methods that are very useful and reliable in ocean acoustics research. The accomplished work provides valuable references for the extraction and application of the acoustic Green's function extraction in different types of ocean environments.

6.2 Future work

Possible future work could be focused on investigating the noise source compositions in the noise interferometry experimental environments, and differentiate the acoustic properties in two studied environments through numerical simulation. In addition, the time warping operators used in Chapter 4 are derived in an ideal waveguide, which is not the same as our experimental environment. If more suitable warping operators are available, the modal separation and Green's function reconstruction will be further improved. Future work can be done on developing and testing an advanced time warping operator for more general environments, such as our obtained optimal geoacoustic model. That work will nicely complement the work reported in this dissertation.

References

[1] Rytov, S. M. (1956) On thermal agitation in distributed systems, *Soviet Phys. Doklady* **1**, 555-559.

[2] S. M. Rytov, Yu. A. Kravtsov and V. I. Tatarskii, *Principles of Statistical Radiophysics. 3: Elements of Random Fields* (Springer, New York, 1989). 29

[3] Claerbout, J. F. (1968) Synthesis of a layered medium from its acoustic transmission response, *Geophysics* **33**, 264-269.

[4] O. I. Lobkis and R. L. Weaver, "On the emergence of the Green's function in the correlations of a diffuse field," *J. Acoust. Soc. Am.* **110**, 3011-3017 (2001). 29

[5] Weaver, R. L., and O. I. Lobkis (2001) Ultrasonics without a source: Thermal fluctuation correlations at MHz frequencies, *Phys. Rev. Lett.* **87**, 134301.

[6] Derode, A., E. Larose, M. Campillo and M. Fink (2003) How to estimate the Green's function of a heterogeneous medium between two passive sensors? Application to acoustic waves, *J. Appl. Phys. Lett.* **83**, 3054-3056.

[7] Derode, A., E. Larose, M. Tanter, J. de Rosny, A. Tourin, M. Campillo and M. Fink (2003) Recovering the Green's function from field-field correlations in an open scattering medium, *J. Acoust. Soc. Am.* **113**, 2973-2976.

[8] Weaver, R. L., and O. I. Lobkis (2004) Diffuse fields in open systems and the emergence of the Green's function, *J. Acoust. Soc. Am.* **116**, 2731-2734.

[9] K. Wapenaar, "Retrieving the elastodynamic Green's function of an arbitrary inhomogeneous medium by cross correlation," *Phys. Rev. Lett.* **93**, 254301 (2004). 29

[10] R. Snieder, "Extracting the Green's function from the correlation of coda waves: A derivation based on stationary phase," *Phys. Rev. E* **69**, 046610 (2004). 29

[11] R. L. Weaver and O. I. Lobkis, "Fluctuations in diffuse field-field correlations and the emergence of the Green's function in open systems," *J. Acoust. Soc. Am.* **117**, 3432-3439 (2005). 29

[12] K. G. Sabra, P. Roux and W. A. Kuperman, "Emergence rate of the time-domain Green's function from the ambient noise cross-correlation function," *J. Acoust. Soc. Am.* **118**, 3524-3531 (2005). 29

[13] Wapenaar K., E. Slob and R. Snieder (2006) Unified Green's function retrieval by cross-correlation, *Phys. Rev. Lett.* **97**, 234301.

[14] O. A. Godin, "Recovering the acoustic Green's function from ambient noise cross-correlation in an inhomogeneous moving medium," *Phys. Rev. Lett.* **97**, 054301 (2006). 29

[15] Godin, O. A. (2007) Emergence of the acoustic Green's function from thermal noise, *J. Acoust. Soc. Am.* **121**, EL96-EL102.

[16] R. Snieder (2007) Extracting the Green's function of attenuating heterogeneous acoustic media from uncorrelated waves, *J. Acoust. Soc. Am.* **121**, 2637-2643.

[17] Bardos, C., J. Garnier and G. Papanicolaou (2008) Identification of Green's function singularities by cross correlation of noisy signals, *Inverse Problems* **24**, 015011.

[18] O. A. Godin, "Retrieval of Green's functions of elastic waves from thermal fluctuations of fluid-solid systems," *J. Acoust. Soc. Am.* **125**, 1960-1970 (2009). 29

[19] Godin, O. A. (2009) Emergence of deterministic Green's functions from noise generated by finite random sources, *Phys. Rev. E* **80**, 066605.

[20] J. Garnier and J. Papanicolaou, "Passive sensor imaging using cross correlations of noisy signals in a scattering medium," *SIAM J. Imaging Sciences* **2**, 396-437 (2009). 29

[21] R. B. Weaver, B. Froment and M. Campillo, "On the correlation of non-isotropically distributed ballistic scalar diffuse waves," *J. Acoust. Soc. Am.* **126**, 1817-1826 (2009). 29

[22] O. A. Godin, "Cross-correlation function of acoustic fields generated by random high- frequency sources," *J. Acoust. Soc. Am.* **128**, 600-610 (2010). 29

[23] M. G. Brown, "Noise interferometry in the geometric limit in a multipathing environment," *J. Acoust. Soc. Am.* **130**, EL173-EL179 (2011). 29

[24] N. A. Zabotin and O. A. Godin, "Emergence of acoustic Green's functions from time averages of ambient noise," *Acta Acustica united with Acustica* **97**, 44-53 (2011). 29

[25] M. Campillo and A. Paul, "Long-range correlations in the diffuse seismic coda," *Science* **299**, 547-549 (2003). 29

[26] N. M. Shapiro, M. Campillo, L. Stehly and M. Ritzwoller, "High resolution surface wave tomography from ambient seismic noise," *Science* **307**, 1615-1618 (2005). 29

[27] Curtis, A., P. Gerstoft, H. Sato, R. Snieder and K. Wapenaar (2006) Seismic interferometry – Turning noise into signal, *The Leading Edge* **25**, 1082-1092.

[28] Y. Yang, M. H. Ritzwoller, A. L. Levshin and N. M. Shapiro," Ambient noise Rayleigh wave tomography across Europe," *Geophys. J. Int.* **168**, 259-274 (2007). 29

[29] Stankiewicz, J., T. Ryberg, C. Haberland, Fauzi and D. Natawidjaja (2010) Lake Toba volcano magma chamber imaged by ambient seismic noise tomography, *Geophys. Res. Lett.* **37**, L17306.

[30] Snieder, R., and E. Larose (2013).Extracting Earth's elastic wave response from noise measurements. *Ann. Rev. Earth Planetary Sci.* **41**, 183-206.

[31] Gorbatov, A., E. Saygin and B. L. N. Kennett (2013) Crustal properties from seismic station autocorrelograms. *Geophys. J. Int.* **192**, 861-870.

[32] M. Campillo and P. Roux, "Seismic imaging and monitoring with ambient noise correlations. In *Treatise of Geophysics*, Vol. 1, edited by B. Romanowicz and A. Dziewonski (Elsevier, Amsterdam, 2014), p. 256-271. 29

[33] Ridder, S. A. L., B. L. Biondi and R. G. Clapp (2014). Time-lapse seismic noise correlation tomography at Valhall, *Geophys. Res. Lett.* **41**, 6116-6122.

[34] T. L. Duvall Jr., S. M. Jeffferies, J. W. Harvey and M. A. Pomerantz, "Time-distance helioseismology," *Nature* **362**, 430-432 (1993). 29

[35] Rickett, J., and J. Claerbout (1999) Acoustic daylight imaging via spectral factorization: Helioseismology and reservoir monitoring, *The Leading Edge* **18**, 957-960.

[36] J. E. Rickett and J. F. Claerbout, "Calculation of the Sun's impulse response by multi-dimensional spectral factorization," *Solar Physics* **192**, 203-210 (2000). 29

[37] M. M. Haney, "Infrasonic ambient noise interferometry from correlations of microbaroms," *Geophys. Res. Lett.* **36**, L19808 (2009). doi:10.1029/2009GL040179. 29

[38] J. T. Fricke, L. G. Evers, P. S. M. Smets, K. Wapenaar and D. G. Simons, "Infrasonic interferometry applied to microbaroms observed at the Large Aperture Infrasound Array in the Netherlands," *J. Geophys. Res. Atmospheres* **119**, 9654-9665 (2014). 29

[39] O. A. Godin, V. G. Irisov and M. I. Charnotskii, "Passive acoustic measurements of wind velocity and sound speed in air," *J. Acoust. Soc. Am.* **135**(2), EL68-EL74 (2014). doi:10.1121/1.4862885. 29

[40] R. Snieder and E. Safak, "Extracting the building response using seismic interferometry; theory and application to the Millikan Library in Pasadena," California, *Bull. Seismol. Soc. Am.* **96**, 586-598 (2006). 29

[41] K. G. Sabra, E. S. Winkel, D. A. Bourgoyne, B. R. Elbing, S. L. Ceccio, M. Perlin and D. R. Dowling, "On using cross-correlation of turbulent flow-induced ambient vibrations to estimate the structural impulse response. Application to structural health monitoring," *J. Acoust. Soc. Am.* **121**, 1987-2005 (2007). 29

[42] Sabra, K. G., S. Conti, P. Roux and W. A. Kuperman (2007) Passive in vivo elastography from skeletal muscle noise, *Appl. Phys. Lett.* **90**, 194101.

[43] O. A. Godin, N. A. Zabotin, A. F. Sheehan and J. A. Collins, "Interferometry of infragravity waves off New Zealand," *J. Geophys. Res. Oceans* **118**(2), 1103-1122 (2014). doi:10.1002/2013JC009395. 29

[44] P. Roux, W. A. Kuperman and the NPAL Group, "Extracting coherent wave fronts from acoustic ambient noise in the ocean," *J. Acoust. Soc. Am.* **116**, 1995-2003 (2004). 29, 31, 32

[45] Sabra, K., P. Roux and W. A. Kuperman (2005) Arrival-time structure of the time averaged ambient noise cross-correlation function in an oceanic waveguide, *J. Acoust. Soc. Am.* **117**, 164-174.

[46] Kuryanov, B. F. (2006) On possibility of passive acoustic tomography in the diffuse noise field, in Ocean Acoustics, Proc. 11th L. M. Brekhovskikh Conf. (GEOS, Moscow), pp. 179-185.

[47] L. A. Brooks and P. Gerstoft, "Ocean acoustic interferometry," *J. Acoust. Soc. Am.* **121**, 3377-3385 (2007). 29

[48] S. E. Fried, W. A. Kuperman, K. G. Sabra and P. Roux, "Extracting the local Green's function on a horizontal array from ambient ocean noise," *J. Acoust. Soc. Am.* **124**, EL183-EL188 (2008). 29

[49] L. A. Brooks and P. Gerstoft, "Green's function approximation from cross-correlations of 20-100 Hz noise during a tropical storm," *J. Acoust. Soc. Am.* **125**, 723-734 (2009). 29

[50] O. A. Godin, N. A. Zabotin and V. V. Goncharov, "Ocean tomography with acoustic daylight," *Geophys. Res. Lett.* **37**, L13605 (2010). doi:10.1029/2010GL043623. 29

[51] O. A. Godin, “On the possibility of using acoustic reverberation for remote sensing of the ocean dynamics,” *Acoust. Phys.* **58**(1), 129-138 (2012). doi:10.1134/S1063771012010101. 29

[52] Leroy, C., S. Lani, K. G. Sabra, W. S. Hodgkiss, W. A. Kuperman and P. Roux (2012) Enhancing the emergence rate of coherent wavefronts from ocean ambient noise correlations using spatio-temporal filters, *J. Acoust. Soc. Am.* **132**, 883-893.

[53] K. G. Sabra, S. Fried, W. A. Kuperman and M. Prior, “On the coherent components of low-frequency ambient noise in the Indian Ocean.” *J. Acoust. Soc. Am.* **133**, EL20-EL25 (2013). 29

[54] S. E. Fried, S. C. Walker, W. S. Hodgkiss and W. A. Kuperman, “Measuring the effect of ambient noise directionality and split-beam processing on the convergence of the cross-correlation function.” *J. Acoust. Soc. Am.* **134**, 1824-1832 (2013). 29

[55] S. W. Lani, K. G. Sabra, W. S. Hodgkiss, W. A. Kuperman and P. Roux, “Coherent processing of shipping noise for ocean monitoring.” *J. Acoust. Soc. Am.* **133**, EL108-EL113 (2013). 29

[56] M. Siderius, C. H. Harrison and M. B. Porter, “A passive fathometer technique for imaging seabed layering using ambient noise,” *J. Acoust. Soc. Am.* **120**, 1315-1323 (2006). 29

[57] Gerstoft P., W. S. Hodgkiss, M. Siderius and C. H. Harrison (2008) Passive fathometer processing, *J. Acoust. Soc. Am.* **123**, 1297-1305.

[58] M. Siderius, H. Song, P. Gerstoft, W. S. Hodgkiss, P. Hursky and C. Harrison, “Adaptive passive fathometer processing,” *J. Acoust. Soc. Am.* **127**, 2193-2200 (2010). 29

[59] Ren, Q., and J.-P. Hermand (2013) Acoustic interferometry for geoacoustic characterization in a soft-layered sediment environment, *J. Acoust. Soc. Am.* **133**, 82-93.

[60] Kim, J., and J. W. Choi (2014) Adaptive passive fathometer processing of surface-generated noise received by Nested array. *J. Acoust. Soc. Am.* **136**, 2149-2149.

[61] C. Yardim, P. Gerstoft, W. S. Hodgkiss and J. Traer, “Compressive geoacoustic inversion using ambient noise,” *J. Acoust. Soc. Am.* **135**, 1245-1255 (2014). 29

[62] O. A. Godin, “Accuracy of the deterministic travel times retrieval from cross-correlations of non-diffuse ambient noise,” *J. Acoust. Soc. Am.* **126**, EL183-EL189 (2009). 30

[63] M. G. Brown, O. A. Godin, N. J. Williams, N. A. Zabotin, L. Zabotina and G. J. Banker, “Acoustic Green’s function extraction from ambient noise in a coastal ocean environment,” *Geophys. Res. Lett.* **41**, 5555-5562 (2014).

[64] O. A. Godin, M. G. Brown, N. A. Zabotin, L. Zabotina and N. J. Williams, “Passive acoustic measurement of flow velocity in the Straits of Florida,” *Geosci. Lett.* **1**, Art. 16 (2014). doi:10.1186/s40562-014-0016-6. 56, 75

[65] J. A. Hildebrand, “Anthropogenic and natural sources of ambient noise in the ocean,” *Mar. Ecol. Prog. Ser.* **395**, 5-20 (2009). doi:10.3354/meps08353. 32

[66] D. S. Ahluwalia and J. B. Keller, “Exact and asymptotic representations of the sound field in a stratified ocean,” in *Wave Propagation and Underwater Acoustics*, Lecture Notes in Physics, vol 70, edited by J. B. Keller and J. S. Papadakis (Springer, New York, 1977). 31

[67] L. M. Brekhovskikh and Yu. P. Lysanov, *Fundamentals of Ocean Acoustics, 3rd edition* (Springer, New York, 2003). 32

[68] M. B. Porter, “The KRAKEN normal mode program,” http://oalib/hlsresearch.com/Modes/kraken.pdf (date last viewed 3/19/2015). 33, 44

[69] G. M. Wenz, Acoustic ambient noise in the ocean: Spectra and sources, *J. Acoust. Soc. Am.* **34**, 1936-1956 (1962).

[70] M. F. McKenna, D. Ross, S. M. Wiggins and J. A. Hildebrand, Underwater radiated noise from modern commercial ships, *J. Acoust. Soc. Am.* **131**, 92-103 (2012).

[71] F. S. Anselmetti, G. A. von Salis, K. J. Cunningham and G. P. Eberli, “Acoustic properties of Neogene carbonates and siliciclastics from the subsurface of the Florida Keys: implications for seismic reflectivity,” *Mar. Geol.* **144**, 9-31 (1997). 35, 41

[72] F. B. Jensen, W. A. Kuperman, M. B. Porter and H. Schmidt, *Computational Ocean Acoustics*, Chapter 1 and 5 (Springer, New York, 2000). 35, 44

[73] Y. Jiang, N. R. Chapman and H. A. Deferrari, “Geoacoustic inversion of broadband data by matched beam processing,” *J. Acoust. Soc. Am.* **119**, 3707-3715 (2006). 42

[74] C. L. Monjo, H. Nguyen and H. A. Deferrari, “Modulations of detectable pulse response time spread in shallow water resulting from a combination of sound-speed variability and bottom loss,” *J. Acoust. Soc. Am.* **102**, 2083-2097 (1997). 42

[75] M. Fink, Time-reversed acoustics, *Physics Today* **50**, 34-40 (1997). 47

[76] W. A. Kuperman, W. S. Hodgkiss, H. C. Song, T. Akal, C. Ferla and D. R. Jackson, Phase conjugation in the ocean: experimental demonstration of an acoustic time-reversal mirror, *J. Acoust. Soc. Am.* **102**, 1-16 (1997). 47

[77] H. C. Song, W. A. Kuperman and W. S. Hodgkiss, A time-reversal mirror with variable range focusing, *J. Acoust. Soc. Am.* **103**, 3234-3240 (1998). 47

[78] W. S. Hodgkiss, H. C. Song, W. A. Kuperman, T. Akal, C. Ferla and D. R. Jackson, A long-range and variable focus phase-conjugation experiment in shallow water, *J. Acoust. Soc. Am.* **105**, 1597-1604 (1999). 47

[79] G. Le Touze, B. Nicolas, J. I. Mars, and J. L. Lacoume, Matched representations and filters for guided waves, *IEEE Trans. Sign. Process.* **57**, 1783-1795 (2009). 58

[80] J. Bonnel, B. Nicolas, J. I. Mars and S. C. Walker, Estimation of modal group velocities with a single receiver for geoacoustic inversion in shallow water, *J. Acoust. Soc. Am.* **128**, 719-727 (2010). 59

[81] J. Bonnel and N. R. Chapman, Geoacoustic inversion in a dispersive waveguide using warping operators, *J. Acoust. Soc. Am.* **130**, EL101-EL107 (2011). 59

[82] J. Zeng, J. Bonnel and N. R. Chapman, Inversion of seabed attenuation using time-warping of close range data, *J. Acoust. Soc. Am.* **134**, EL394-EL399 (2013). 59

[83] H. Niu, R. Zhang, and Z. Li, Theoretical analysis of warping operators for non-ideal shallow water waveguides, *J. Acoust. Soc. Am.* **136**, 53-65 (2014). 60

[84] O. A. Godin, An effective quiscent medium for sound propagating through an inhomogeneous, moving fluid, *J. Acoust. Soc. Am.* **112**, 1269-1275 (2002). 72

[85] J. W. Strutt (Baron Rayleigh), *The Theory of Sound*, Vol. 2, 2nd ed., revised and enlarged (MacMillan, London, New York, 1896), p. 132. 71

[86] X. Zang, M. G. Brown and O. A. Godin, Waveform modeling and inversion of ambient noise cross-correlation functions in a coastal ocean environment, *J. Acoust. Soc. Am.* **138**, 1325-1333 (2015). 73, 74